INTERACTION OF PICOSECOND LASER PULSES WITH MATTER

R. R. ALFANO

Technical Report
TR 72-230.1

April 1972

Updated 2010

City College of The City University of New York

ralfano@sci.ccny.cuny.edu

GTE LABORATORIES INC.

ABSTRACT

In this work, an intense picosecond laser beam is used to investigate four-photon effects and temporal behavior of optical phonons.

The less-well-known four-photon effects such as self-phase modulation and four-photon parametric generation are studied experimentally and theoretically. Mechanisms for these processes are given. Self-phase modulation and small-scale filament formation are observed in numerous crystals, glasses, and liquids including liquidified and solidified rare gases. Typically, the self-phase modulation spectra spans thousands of wavenumbers to the red and blue of the exciting 5300 Å picosecond laser pulse. The physical mechanism responsible for these processes is the change in the refractive index resulting from electronic cloud distortion. Four-photon parametric is observed in glass. The emission is generated from 4000 to 7000 Å, the wavelength depending on emission angle.

The lifetime of 1086 cm^{-1} optical phonon in calcite is measured directly by using the picosecond laser beam to create the phonons by stimulated Raman scattering, and then observing Raman scattering off the phonons at various delay times with a weaker probe picosecond beam. The lifetime has been measured in different phonon decay regimes. A theoretical analysis is given for the phonon decay process and probe-Raman light scattering process.

TABLE OF CONTENTS

LIST OF ILLUSTRATIONS

II FIGURE CAPTIONS

III - FIGURE CAPTIONS

Fig. III-1. Experimental arrangement for observing frequency broadening (SPM), stimulated Raman scattering, and self-focusing.

Fig. III-2. Stokes and anti-Stokes SPM spectra from calcite for different laser shots. The laser beam propagates as an O-wave through the sample.

Fig. III-3. Stokes and anti-Stokes SPM spectra from calcite for different laser shots. The laser beam propagates as an E-wave.

Fig. III-4. Modulated SPM spectra for calcite.

Fig. III-5. Stokes and anti-Stokes from BK-7 glass and filament formation for different laser shots. The filaments are viewed through F': 3-67 filters.

Fig. III-6. A comparison of SPM emission from various glasses: LBC, LDF, and DF-2.

Fig. III-7. SPM emission and filament formation from NaCl.

Fig. III-8. SPM spectra and filament formation from a quartz crystal for the laser propagating an O-wave.

Fig. III-9. A comparison of the extent of the Stokes spectra for flint glass, quartz, and calcite. Kodak N-plate were used. Solid exit face was not focused in the slit. The laser was focused with f = 25 cm into the sample.

Fig. III-10. A comparison of the threshold for SRS and SPM for the laser propagating as O and E waves in calcite. The laser was focused into calcite with f = 25 cm lens. The solid exit face was not imaged on the slit.

Fig. III-11. Experimental arrangement for observing nonlinear effects in liquified and solidified rare gases.

Fig. III-12. Stokes SPM from liquid argon for different laser shots. The laser was focused into the sample with f = 25 cm lens. The exit face was focused on the slit, magnified 10X.

Fig. III-13. Anti-Stokes SPM for liquid argon for different laser shots. The laser was focused into the samples with f = 25 cm lens. The exit face was focused on the slit, magnified 10X.

Fig. III-14. Stokes SPM for liquid krypton for different laser shots. The laser was focused into the samples with f = 25 cm lens. The exit face of the samples was imaged on the slit, magnified 10X.

Fig. III-15. A comparison of typical Stokes SPM spectra for liquid argon and solid krypton. The laser is focused with f = 25 cm and the sample exit face is imaged on the slit, magnified 10X.

Fig. III-16. A simple mechanism for SPM for nonlinear index following the envelope of symmetrical laser pulse; (a) nonlinear index change versus time; (b) time rate of change of index change; (c) frequency change versus time.

Fig. III-17. Calculated SPM spectrum for envelope model (I) for parameters $\beta = 60$, $T_f = 4$ psec.

Fig. III-18. Calculated SPM spectrum for sub-picosecond model (II) for parameters: $\beta = 60$, $T_f = 0.1$ psec.

Fig. III-19. Calculated SPM spectrum for sub-picosecond model (II) for parameters: $\beta = 22$, $T_f = 0.1$ psec.

Fig. III-20. Calculated SPM spectrum for sub-picosecond model (II) for parameters: $\beta = 30$, $T_f = 0.1$ psec.

Fig. III-21. Calculated SPM for electronic model (III) for parameters: $\beta_E = 60$, $T_f = 4$ psec.

Fig. III-22. Calculated SPM for electronic model (III) for parameters: $\beta_E = 60$, $T_f = 4\sqrt{2}$ psec.

Fig. III-23. Calculated SPM for electronic model (III) for parameters: $\beta_E = 60$, $T_f = 0.6$ psec.

Fig. III-24. Calculated SPM for electronic model (III) for parameters: $\beta_E = 90$, $T_f = 0.6$ psec.

Fig. III-25. Calculated SPM for electronic model (III) for parameters: $\beta_E = 120$, $T_f = 0.6$ psec.

Fig. III-26. Calculated SPM for electronic model (III) for parameters: $\beta_E = 150$, $T_f = 0.6$ psec.

Fig. III-27. Calculated SPM for electronic model (III) for parameters: $\beta_E = 60$, $T_f = 0.1$ psec.

Fig. III-28. Calculated SPM for electronic model (III) for parameters: $\beta_E = 30$, $T_f = 0.1$ psec.

Fig. III-29. Calculated SPM for electronic model (III) for parameters: $\beta_E = 60$, $T_f = 0.2$ psec.

Fig. III-30. Calculated SPM for a combined electronic and molecular mechanism. The parameters are $\beta_E = 120$, $T_f = 0.6$ psec for an electronic model III and $\beta_M = 1200$, $T_f = 4\sqrt{2}$ psec for the molecular model (I).

IV - FIGURE CAPTIONS

Fig. IV-1. Four-photon coupling showing volume phase matching among two-laser, anti-Stokes, and Stokes photon.

Fig. IV-2. Experimental arrangement for displaying the emission from materials as a function of wavelength and angle.

Fig. IV-3. Schematic wavelength and angular spectra for SRS (top) and for SPM and four-photon parametric emission (bottom).

Fig. IV-4. (a) Angular anti-Stokes emission with main laser beam at slit center. Light in center is frequency swept light while outer curves are due to four-photon emission; (b) entire angular anti-Stokes emission curve from 4000 to 5300 Å for BK-7 glass, length 8.9 cm.

Fig. IV-5. Stokes emission from BK-7 glass, $\ell = 8.9$ cm. Filters 3-67. Light at center is SPM while outer curves are due to four-photon emission.

Fig. IV-6. Calculated four-photon power flow versus momentum mismatch centered at the phase matching anti-Stokes angle for the following parameters (a) $\gamma_o = 3\ cm^{-1}$, $\ell = 0.5$ cm, $g_o\ell = 3$; (b) $\gamma_o = 10\ cm^{-1}$, $\ell = 0.5$ cm, $g_o\ell = 10$; (c) $\gamma_o = 3\ cm^{-1}$, $\ell = 3$ cm, $g_o\ell = 18$. The zero-point flucutation noise power, $P_o \sim 10^{-2}$ watts/cm^2 - 10^{-1} watts/cm^2.

Fig. IV-7. Anti-Stokes angle outside materials: circles, experimental points; dash-dot, curve I calculated for Class-I emission; dash, curve II calculated for Class-II emission; solid line, curve III calculated for small scale filaments plus a nonlinear index change.

Fig. IV-8. Angular anti-Stokes spectra from calcite for O-wave excitation. Length 6.5 cm; beam is focused by f = 25 cm; filters: 5-60 and 5-61; and the collecting lens f = 10 cm is located 10 cm from the slit of spectrograph.

V. FIGURE CAPTIONS

Fig. V-1. Phonon dispersion curve of diatonic lattice.

Fig. V-2. Decay of optical phonon into two acoustic phonons.

Fig. V-3. Refractive index indicatrix for uniaxial crystal.

Fig. V-4. Direction of wave normal, of the field vectors and energy flow in an anisotropic crystal.

Fig. V-5. Table I: Ordinary and extraordinary refractive index of calcite (18°C) from critical tables.[11]

Fig. V-6. Table II: Useful parameters for phase-matched probe Stokes scattering.

Fig. V-7. Angles for the probe and exciting laser beams (a) outside calcite, (b) noncollinear phase matching inside the calcite.

Fig. V-8. Table III: Group velocity for probe, laser, and Stokes Raman pulses.

Fig. V-9. Experimental arrangement.

Fig. V-10. Signals detected and displayed coincident on 555 scope.

Fig. V-11. Probe Stokes scattering intensity versus stimulated Raman scattering intensity (number of phonon scattering versus number of phonon produced.

Fig. V-12. Effect of phase matching on probe scattering.

Fig. V-13. Probe Stokes Raman angular and wavelength dependence (a) 1.06 present (b) 1.06 absence. Probe: 5300 Å.

Fig. V-14. Normalized Stokes Raman-scattered probe intensity versus delay time between 1.06- and 0.53-μm beams at R. T. and 100°K.

Fig. V-15. Three-phonon decay process: (a) scattering process, (b) splitting process.

Fig. V-16. Phonon dispersion curve showing the decay of optical phonon splitting into two acoustic phonons.

Fig. V-17. Optical phonon lifetime, τ, as function of its momentum, k_1, for the splitting process (op $\rightarrow$ 2 as): $\beta = 1\ cm^2/sec$, $\Gamma_{AS} = 10^7\ sec^{-1}$, $Q = 10^8\ cm^{-1}$; (a) $\partial\omega_2/\partial k_2 = 10^2$ cm/sec; (b) $\partial\omega_2/\partial k_2 = 3 \times 10^2$ cm/sec.

Fig. V-18. Phonon dispersion curve showing the decay of optical phonon splitting into two optical phonons.

Fig. V-19. Phonon dispersion curve showing the scattering of the optical phonon with an acoustic phonon to give another optical phonon.

Fig. V-20. Optical phonon lifetime as function of its momentum for the scattering process: (op + as $\rightarrow$ op): $\beta = 1\ cm^2/sec$, $\Gamma_{AS} = 10^7\ sec^{-1}$, $Q = 10^8\ cm^{-1}$, (a) $\partial\omega_2/\partial k_2 = 10^2$ cm/sec; (b) $\partial\omega_2/\partial k_2 = 3 \times 10^2$ cm/sec.

Fig. V-21. A plot of the phonon lifetime T_1 versus the phonon lifetime T_{1ex} extracted from the tail of the convolution of an exponential decaying phonon population at a rate T_1 with a Gaussian shape laser pulse of duration T_L. The T_{1ex} is obtained from the slope of tail at $\tau_D > T_L$. The percent error in T_1 is shown at varius T_1/T_L ratios.

Fig. V-22. A plot of the phonon lifetime T_1 versus the phonon lifetime T_{1ex} extracted from the tail of the convolution of an exponential decaying phonon population at a rate T_1 with full exponential shape laser pulse of duration T_L.

Fig. V-23. A plot of the phonon lifetime T_1 versus the lifetime T_{1ex} extracted from the tail of the convolution of an exponential decaying phonon population at a rate T_1 with a Lorenztian shape laser pulse of duration T_L.

Fig. V-24. Plot of an exponentially decaying phonon population (T_1 = 22 psec) convoluted with (a) Gaussian, (b) full exponential, and (c) Lorenztian laser shape pulse of FWHM of 3 psec.

Fig. V-25. Plot (a) is the calculated probe Stokes energy versus delay time τ_D (convolution of exponentially decaying phonon population with lifetimes T_1 = 19 psec with an exponentially shaped laser pulse of duration T_L = 5 psec); and a plot (b) is the experimentally measured probe Stokes energy at 100°K from calcite (the measured lifetime from the tail is T_1 = 19.1 psec). The convolution curve is shifted in time by 5 psec to match the tails.

I. INTRODUCTION

The advent of powerful laser beams makes possible the observation of nonlinear optical processes in materials. These processes are nonlinear in the sense that the polarization of the material varies nonlinearity with the laser's electric field. This gives rise to multi-wave interactions, the susceptibility providing the coupling between the individual light waves. The resulting nonlinear polarization acts as a source term in Maxwell's equations and gives rise to the generation of new frequencies and effects. To describe the nonlinear processes the macroscopic polarization of the medium in the electric dipole approximation is expanded in a power series in the field:

$$P = \chi^{(1)}\bar{E} + \chi^{(2)}\bar{E}\bar{E} + \chi^{(3)}\bar{E}\bar{E}\bar{E} + \ldots \quad (1)$$

The coefficients $\chi^{(1)}$, $\chi^{(2)}$, and $\chi^{(3)}$ denote respectively, the second, third and fourth rank susceptibility tensor which are a measure of the strength of the coupling between the different light waves. The power series expansion given by equation (1) becomes a poor approximation when the electric field of the laser is on the order of the atomic field $\sim 3 \times 10^{8}$ V/cm. Armstrong et al[1] using a quantum mechanical approach related the nonlinear microscopic properties produced by two or more light quanta interactions to the susceptibility coefficients of the macroscopic nonlinear polarization. Linear optical phenomena such as absorption is associated with $\chi^{(1)}$ while Armstrong et al[1] has shown that $\chi^{(2)}$ is associated with three-photon interactions such as second harmonic generation and $\chi^{(3)}$ is associated with four-photon interactions such as third harmonic generation. The size of the first three χ coefficients are $\chi^{(1)} \sim 10^{-1}$ esu, $\chi^{(2)} \sim 10^{-7} - 10^{-9}$ esu and $\chi^{(3)} \sim 10^{-11} - 10^{-14}$ esu. In media with inversion symmetry (cubic and isotropic solids and liquids) the lowest order nonlinear effects are associated with $\chi^{(3)}$.

The field of nonlinear optics has been a very active field of investigation since the observation of second harmonic generation by Franken[2] and coworkers in 1961. New frequencies have been created in the U.V., visible, and infrared spectral regions through parametric amplifications, Raman laser action, stimulated polariton scattering, and harmonic generation. The size and importance of the nonlinear terms have been limited by the power and pulse width of available lasers typically 10 MW in power and 10 nsec in duration.

With the recent development of the mode-locked laser[3] with its extremely high peak power $\sim 10^9$W and ultrashort pulse width $\sim 10^{-12}$ sec, nonlinear terms become larger and new effects become observable. The nonlinear terms can now be as large as 1 to 1/100 of percent of the linear term. The development of the mode-locked laser opened a new era in nonlinear optics, and can be regarded as one of the major achievements of physics in the last few years. Not only is the generation of phenomenon of great interest but the application of the ultra short pulses to the measurement and study of other physical processes is just emerging. For there is no other man made and controllable event which takes place on the time scale of 10^{-12} sec as the emission from a mode-locked laser. Yet there are many naturally occurring physical processes which are accomplished in just this interval of time. For instance an atom or ion in a solid completes one period of oscillation; a molecule in a liquid collides with a neighbor or changes orientation, all of this is a time comparable to the ultrashort pulse. Even an electron accomplishes only about one thousand revolutions around the nucleus in a picosecond.

Moreover the electric field intensity during a picosecond pulse can become a substantial fraction (of the order of a percent) of the electric fields inside an atom. Hence not only can it affect a molecule, but can even reach within an atom and distort its spherical shape. All of this defines an essentially new area of physics in a hitherto totally inaccessible domain of time and electric field intensity.

The use of the mode-locked laser in this work has four important consequences: First, the low value of the electronic part of $\chi^{(3)}$ (generally in the range of $10^{13} - 10^{-14}$ esu) is no longer an impediment to the observation of the effect due to electronic distortion. Second, because of the short duration of the pulse, it is now possible to distinguish between molecular and electronic processes in materials. Third, the short pulses can be used for direct measurement of ultrafast lifetimes of elementary excitation; typically $\sim 10^{-12}$ sec. Finally, the use of the intense ultrashort pulses eliminates the efficient conversion of a large fraction of laser light to stimulated Brillouin scattering (SBS)[4]. The breakdown and damage of the material caused by the large acoustic phonon flux produced by SBS is thus greatly reduced by the use of short pulses.

In this thesis, I investigate experimentally and theoretically four-photon interactions accompanying the passage of intense picosecond laser pulses through matter and the direct measurement of an optical phonon lifetime. I have concentrated mainly on the less well-known four-photon effects arising from $\chi^{(3)}$ such as frequency broadening of the spectrum of the light due to self-phase modulation, (SPM), nondegenerate four-photon parametric generation, as well as self-focusing and the transient stimulated Raman scattering (SRS).

Chapter II describes the experimental technique of generating and detecting picosecond laser pulses. The following chapters describe several first observations and major contributions to nonlinear optics I have made using a mode-locked laser. In Chapter III, frequency broadening of thousands of wavenumbers to the red and blue of the exciting frequency and small scale filaments are investigated in many solids and liquids, and the direct distortion in atomic shapes of argon and krypton atoms under the action of the intense electric field of the laser are demonstrated; in Chapter IV, the four photon parametric generation in glass and other materials are described; and in the final chapter the lifetime of the 1086 cm^{-1} optical phonon in calcite is directly measured at 300°K and 100°K.

I. REFERENCES

1. J.A. Armstrong, N. Bloembergen, J. Ducuing, and P. S. Pershan, Phys. Rev. 127, 1918 (1962).

2. P.A. Franken, A.E. Hill, C.W. Peters, G. Weinreich, Phys. Rev. Lett. 7, 118 (1961).

3. A.J. DeMaria, D.A. Stetser, and H. Heynan, Science, 156, 1557 (1967).

4. R.G. Brewer and C.H. Lee, Phys. Rev. Lett. 21, 267 (1968).
   Y.R. Shen, Phys. Rev. Lett. 20, 378 (1966).
   Y.R. Shen and Y.L. Shaham, Phys. Rev. 163, 224 (1967).
   S.L. Shapiro, J.A. Giordmaine, and K.W. Wecht, Phys. Rev. Lett. 19, 1093 (1967).

II. EXPERIMENTAL TECHNIQUES

This chapter describes the construction of a mode-locked glass laser, the technique used to obtain high second harmonic generation (SHG) conversion,[1] and the measurement of the picosecond pulse width by the two photon fluorescence (TPF) technique.[2]

1. The Laser and Associated Equipment

A schematic representation of the mode-locked glass laser is shown in Fig. II-1 and a photograph of the laser is shown in Fig. II-2. The laser consists of a Nd:Brewster-Brewster cut 7 1/2 x 1/2 inch^2 Owen Illinois glass rod (ED-2), a Korad K-1 laser head, K-1 power supply, and KWC-3 water cooler, a 10-M 100% reflectivity wedge dielectric rear mirror, a 50% dielectric wedge output mirror, a modified Kodak Q-switched dye cell, and lansing mirror mounts. The laser rod is located symmetrical in the cavity. The dye cell is located near the rear mirror. The lengths from the rear and output mirrors to the face of the laser rod are 26 cm and 27 cm respectively. The effective cavity length is 83 cm giving a round trip time of 5.53 nsec for an optical pulse. The use of a 10-M radius of curvature rear mirror instead of a plane parallel mirror makes the alignment of the mirrors less critical and the cavity more stable. The mirrors are wedged to reduce multiple picosecond pulse generation. The wedge angle of the mirrors used ranged from 10' to 1°--the typical wedge angle is 30'. The laser rod and dye cell are oriented at Brewster angle to reduce multiple pulsing and to eliminate reflection losses. The laser rod and dye cell are oriented at 25° and 34° to the optical axis, respectively.

The laser beam is Q-switched and mode-locked with type 9860 Kodak dye dissolved in chlorobenzene and then passed through 1.5 cm of potassium dihydrogen phosphate (KDP) SHG crystal. A typical oscilloscope trace of the output of the laser at 5300 Å detected by TRG No. 105B photodiode is shown in Fig. II-3. Typically 20-60 laser pulses are emitted spaced by the cavity round trip time (5.5 nsec). The power of a pulse at 1.06 μ is typically between 2-8 x 10^9 W which is converted to 2-8 x 10^8 W at the harmonic. The photodiodes were calibrated at 1.06 μ and 0.53 μ by beam splitting 8% of the output into the photodiodes and the remaining portion of the beam into a thermopile.

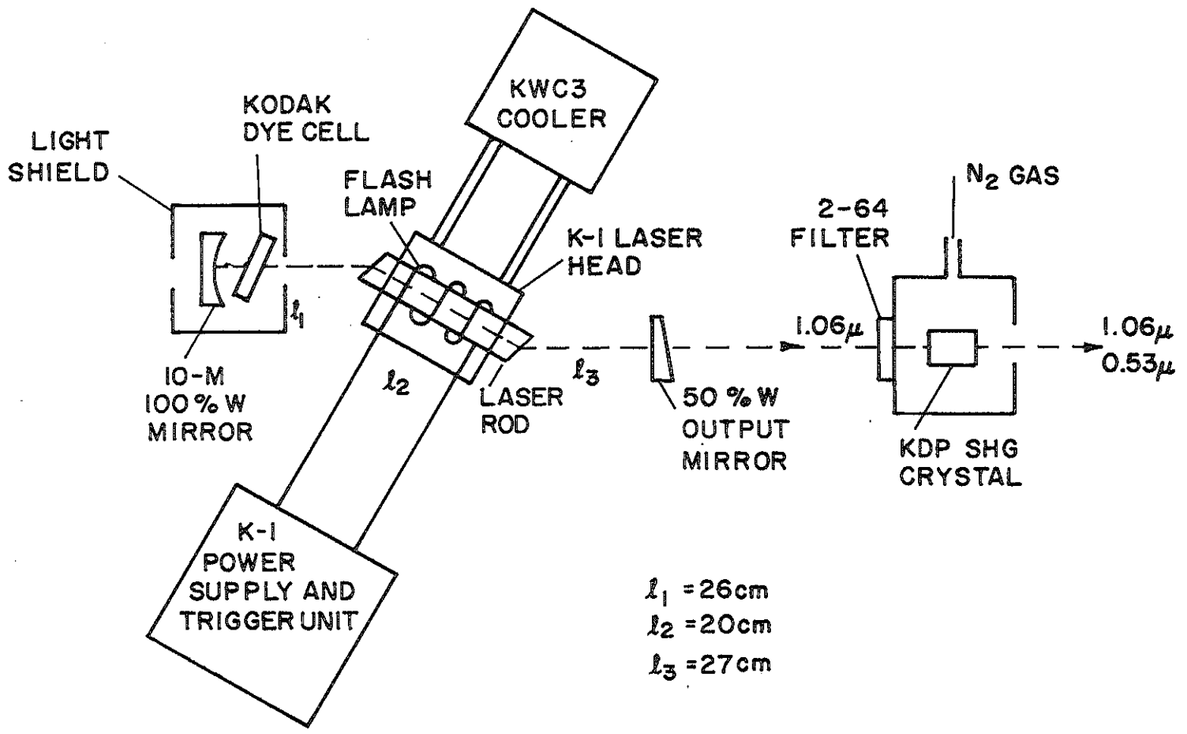

Fig. II-1. Schematic of a mode-locked laser system.

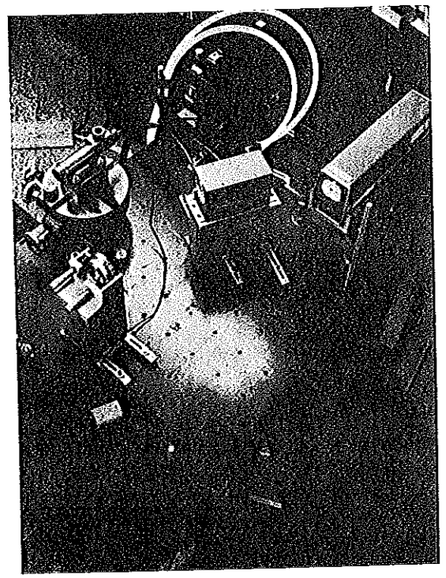

Fig. II-2. Photograph of a mode-locked laser.

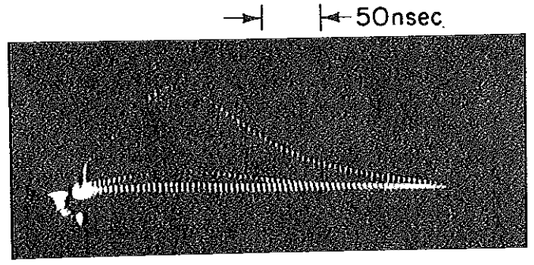

Fig. II-3. Typical oscilloscope trace of output of mode-locked laser.

To obtain a clean mode-locked pulse train, the voltage to the pump lamp and dye transmission are critically adjusted. The transmission through a Kodak dye cell between 57% to 64% and a voltage between 3.0 to 3.5 KV seems to be the best operating range for mode-locking. A single "clean" pulse train usually occurred when the voltage is operated a few voltage above the threshold voltage for lasing.

The mode-locking capability of the Kodak 9860 dye is found to be very sensitive to room lights and air contamination. Within a few hours in room lights the dye did not produce a clean pulse train. By shielding the dye from room lights and by preparing the dye in a N_2 atmosphere, the dye operated effectively for a day. The dye cell is enclosed with the rear mirror in a metal box which has a 3/4 inch hold along the optical path. The anti-reflection (AR) coated glass windows of the Kodak dye cell have been replaced with fused quartz windows because the AR coating and glass windows damaged after a hundred or so laser shots. The rear laser mirror dielectric coatings also damaged after approximately two weeks of continual use.

The Nd:glass rod is situated inside a Korad K-1 laser head. In the K-1 head is a spiral Xenon flashlamp which surrounds the rod and serves to pump the rod. Wrapped around the lamp is a ceramic reflector which improves the pumping efficiency of the laser. A U.V. shield is used to block the U.V. radiation from the flashlamp. The laser rod, flashlamp, and head is cooled directly by cooled thermostatically controlled water at a flow rate of 1.5 gal/min at a temperature of $70 \pm 1.5°F$. Water cooling gives better reproducibility from shot-to-shot at once a minute operation. The K-1 power supply charges the capacitor bank (120 μf) to a selected voltage up to 5 KV with an accuracy of $\pm$ 10 V. Series injection triggering dumps the selected voltage into the lamp.

Optical experiments utilizing pulse lasers require a single mode He-Ne (λ = 6328 Å) alignment laser beam which follows the path of the laser exactly. This allows the optical components in the experiment to be located in the correct position. Since the Nd: glass laser operates at a wavelength of 1.06 μ one cannot send the He-Ne laser beam through the rear mirror to simulate the 1.06 μ laser beam. The 6328 Å laser beam would travel at a slightly different angle after passing through the glass rod because of different angles of refraction for the 1.06 μ and 6328 Å beams. In the far field the 1.06 μ and 6328 Å beams would not coincide. A more complicated alignment system has been assembled which aligns the 1.06 μ and 6328 Å in the near and far field.

The alignment system is shown schematically in Fig. II-4 and a photograph of the system is shown in Fig. II-5.

A davison autocollimator shown in position C is used to align the system. The eyepiece of the collimator has been modified with a crosshair. For aligning the near field of the glass laser with respect to the He-Ne laser A, mirror 2 is removed and the center of the output laser mirror and laser rod is centered in the crosshairs. Mirror 2 is replaced and the bore of the He-Ne laser tube A is also centered in the autocollimator by adjusting a laser A and mirror 2 which is mounted on a lansing mount. The He-Ne laser beam A is attenuated by a factor of $\sim 10^4$ and viewed through the collimator. The He-Ne laser beam A is adjusted so that it is also centered. This locates the far field of the He-Ne alignment laser A with respect to the autocollimator. The He-Ne laser B is used to center the components in the glass laser's cavity such as laser mirrors, dye cell, and glass rod.

To align the far field of glass laser beam with respect to the He-Ne laser A, the cavity is aligned with respect to the autocollimator. Mirror 2 is removed and the cavity is aligned parallel by using standard autocollimator techniques. The rear mirror is adjusted so that the return image from the rear mirror (dim red dot) is returned into the image from the front mirror (white dot) which is centered in the crosshairs. Now, the far and near field of the two lasers are coincident. Mirror 2 and 3 are removed and the laser is ready to fire. Fine tuning of the alignment beam with respect to the 1.06 μ is accomplished by taking a burn pattern on a positive polariod film in the far field and adjusting mirror 2 slightly so that the He-Ne is centered in the burned pattern.

The optical equipment is mounted on two tables (3' x 6'). The benalex table tops are drilled and taped with 1/4-20 holes spaced every three inches. Lens, prisms, beam splitters and other components can be mounted on rods which can be screwed into the tables. The K-1 head, dye cell and mirror mounts are mounted on solid aluminum blocks which are bolted to the table with clamps. Mirrors for the alignment system are mounted on three pins mounts which fit into a V-groove mount. These mirrors can be removed and replaced without changing the optical alignment.

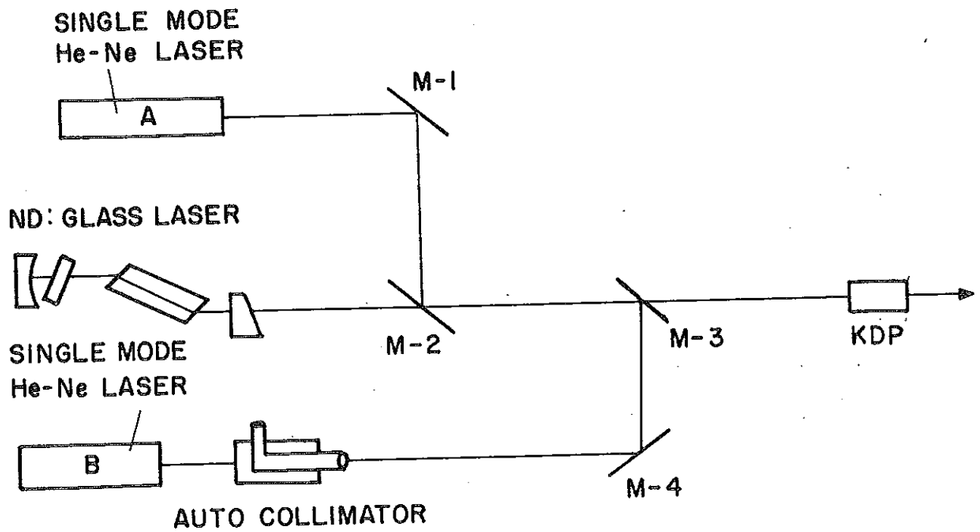

Fig. II-4. Optical alignment system for collinear tracking of 6328 Å and 1.06 μ beams.

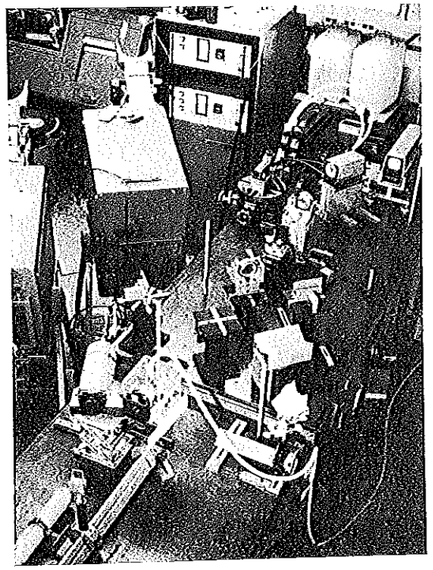

Fig. II-5. Photograph of alignment system.

2. Second Harmonic Generation

The second harmonic of the 1.06 μ laser beam has been used in the experiments because of its convenience in detecting and photographing spectra in the visible region. The alignment of the SHG crystal for the highest conversion is obtained by photographing the SHG emission beam as a function of phase matching angle, θ_o. This technique has been theoretically analyzed by Giordmaine.[1]

The SHG for a KDP crystal not phase matched along the laser beam consists of a bright circular ring and a bright spot. The bright spot is in the direction of the laser beam. This forward light is emitted at low efficiency since phase matching is not satisfied. The ring emission originates from the phase matching the laser beam photon with a small angle scattered photon from the main beam.

As the crystal is rotated through the phase matching angle for the forward laser beam, the ring approaches the bright spot and the intensity of the bright spot increases rapidly. At the phase matching angle, the ring cuts through the bright spot which has increased by a factor of over a 10^3.

Figure II-6 shows the experimental arrangement used to observe the SHG angular emission from KDP vs function of crystal orientation. Figure II-7 shows a series of pictures of SHG emission at various angles below and above the phase matching angle, θo. The SHG emission has been attenuated by a factor of 10^4 in Fig. II-7e. The conversion efficiency in this position is ~10%.

The KDP crystal (1.5 x 1 x 1 cm^3) is oriented and cut for phase matching the 1.06 μ beam by Isomet Corp., Palisades, N.J. The crystal length of 1.5 cm can convert the entire frequency bandwidth of the mode-locked laser output.[3] The crystal is mounted in a Lansing mount which is located in a lucite enclosure purged with N_2 gas. A N_2 atmosphere is necessary because KDP is hydroscopic.

3. Two Photon Fluorescence

The conventional two-photon fluorescence (TPF) technique of Giordmaine and coworkers[2] is used to display the pulse width of the 5300 Å optical pulse. The experimental arrangement is shown in Fig. II-8. After filtering by Corning 2-64 filter to remove the laser fundamental and pump light and telescoping

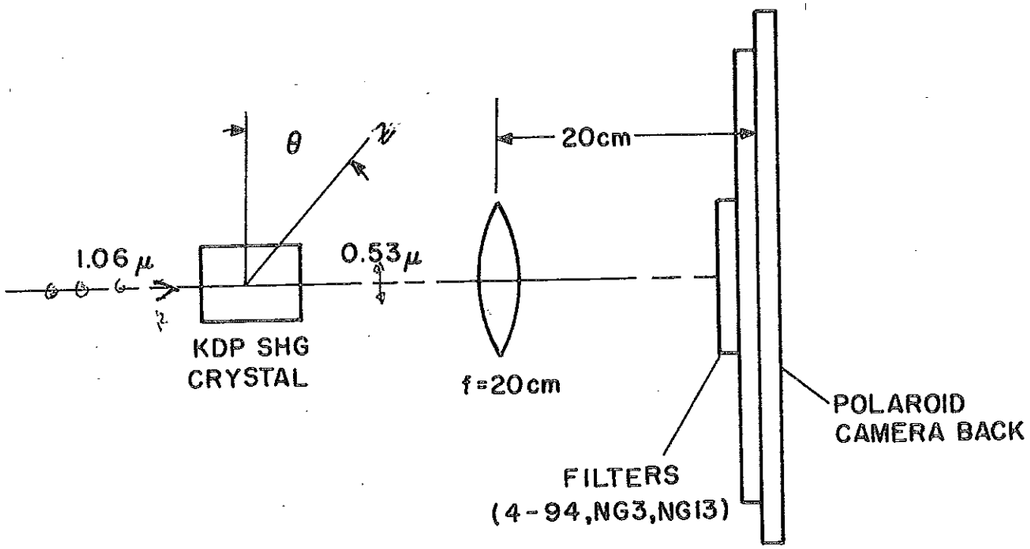

Fig. II-6. Experimental apparatus to obtain maximum second harmonic.

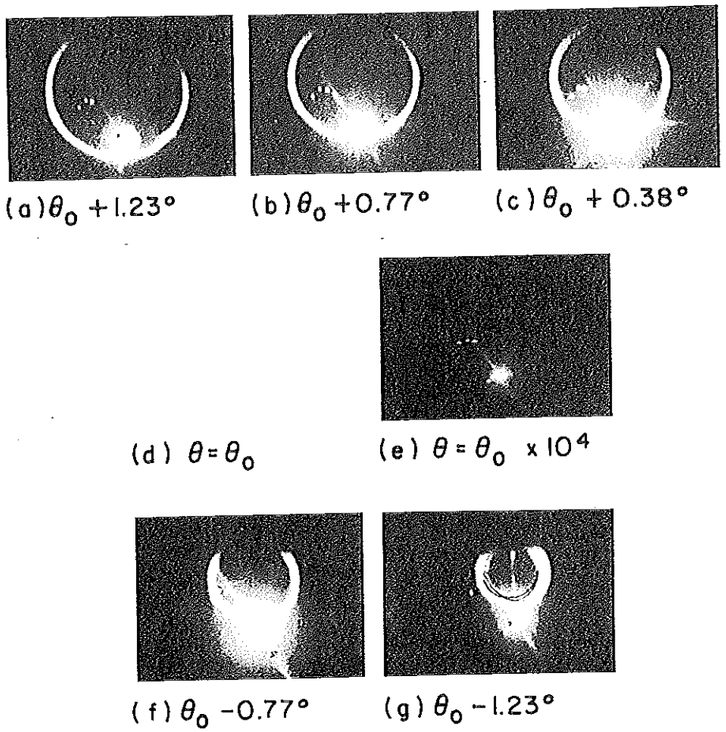

(a) θ_0 +1.23° (b) θ_0 +0.77° (c) θ_0 + 0.38°

(d) $\theta = \theta_0$ (e) $\theta = \theta_0$ x 10^4

(f) θ_0 -0.77° (g) θ_0 -1.23°

Fig. II-7. Second harmonic emission at various angles about the phase matching angle, θ_0.

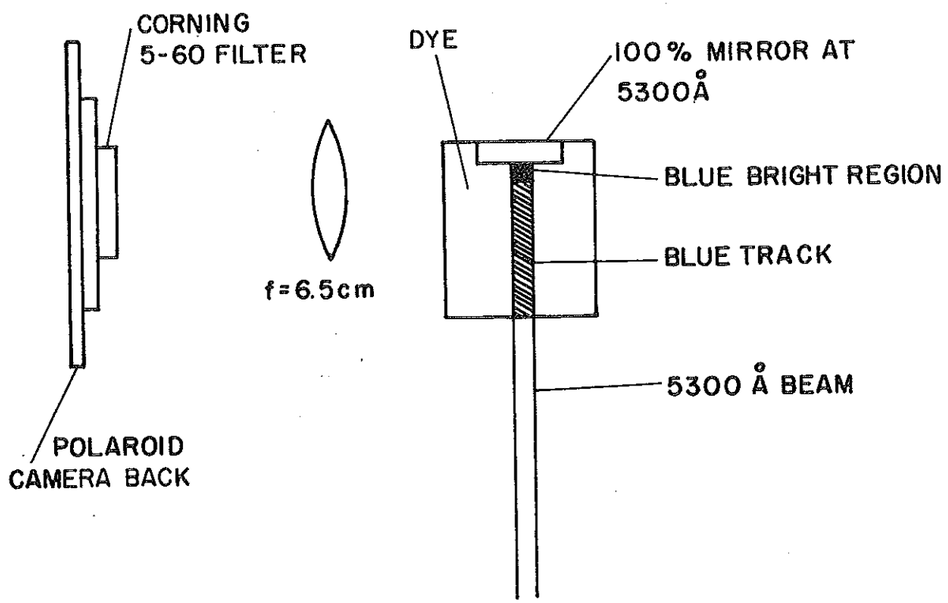

Fig. II-8. Two-photon fluorescence setup.

the beam to ~2 mm, the beam transversed a 5 cm fluorescence cell. In a solution of 7-diethylamino 4-methyl coumarin dissolved in ethanol, the laser beam produced a bright blue track.

A direct measurement of the total width of the pulse is obtained by normal reflection of the beam at the dielectric mirror (R = 100%) immersed in the solution at the exit end of the cell. The length[2] of the bright fluorescence region at the mirror is $ct_p / 2\sqrt{2n}$ where n = 1.5 is the refractive index of the solution and t_p is the pulse width of gaussian pulse. A typical fluorescence track produced by 5300 Å pulse train photograph (Polaroid 3000 speed) through 5 - 60 filters to eliminate 5300 Å scattered light is shown in Fig. II-9 magnified by 2.5 . The short bright region of 0.7 mm/2.5 length at the left occurs at the mirror. This shows that the total burst of radiation at 5300 Å lasts for 4 psec. Rhodamine 6G dissolved in methanol is used to measure the total burst of radiation of 6 psec at a wavelength of 1.06 μ.

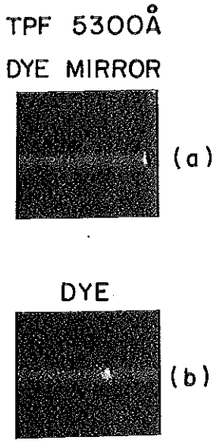

Fig. II-9. Two-photon fluorescence pattern at 5300 Å; (a) TPF pattern at mirror, (b) TPF pattern with beam crossing self; magnified $\cong 2.5$.

II. REFERENCES

1. J.A. Giordmaine, Phys. Rev. Lett. 8, 19 (1961)

2. J.A. Giordmaine, P.M. Rentzepis, S.L. Shapiro and K.W. Wecht, Appl. Phys. Lett. 11, 216 (1967).

3. R.C. Miller, Phys. Lett. 26A, 177 (1968).
   S.L. Shapiro, Appl. Phys. Lett. 13, 19 (1968).

III. SELF-PHASE MODULATION

1. Introduction

This chapter reports on the observation of frequency broadening and self-focusing in numerous crystals, glasses,[1] and liquified and solidified rare gases.[2] We have identified the frequency broadening as arising from self-phase modulation (SPM). Various mechanisms for SPM will be discussed for the materials studied; and the SPM spectra will be calculated and its characteristics compared with the observed spectra.

In the experiment high-power picosecond pulses at a wavelength of 5300 Å were either reduced in area by an inverted Galilean telescope or focused into materials. Under high powers the output spectra of the materials are shifted thousands of wave numbers to the red and blue and show modulation. A similar effect of self-phase modulation from filaments was first observed by Shimizu[3] in liquid CS_2 who attributed the 200 cm^{-1} broadening resulting when a 20 nsec Q-switched ruby laser passed through a cell of CS_2 to the orientational Kerr effect. Rocking of the CS_2 molecules about its equilibrium value has also been proposed to explain the CS_2 spectra.[4] In a Nd-glass laser, Treacy[5] interpreted the picosecond laser pulses as being linearly frequency swept since he was able to compress the pulses by passing them through two gratings. Duguay[6] has shown that the sweep in the mode-locked glass laser originates from SPM. The nonlinear susceptibility coefficients in solids are ~10 to 10^3 times less than in organic liquids, but with high powers available from mode-locked picosecond lasers combined with electronic self-focusing the change in the nonlinear refractive index of solids is large enough to cause an observable frequency broadening.

An intense optical pulse traveling through a medium can distort the atomic configuration of material resulting in a change of the refractive index via the nonlinear coefficients. For a medium having inversion symmetry the first nonlinear coefficient is $\chi^{(3)}$, and the refractive index, n, becomes intensity dependent:

$$n_{\parallel} \equiv n_o + n_2 E^2 \tag{1}$$

where $n_{\parallel}$ is the refractive index parallel to electric field, E is the electric field of the laser, since $n^2 = \epsilon = 1 + 4\pi\chi$ the coefficients: $n_o = (1 + 4\pi\chi^{(1)})^{1/2}$ is the normal refractive index, and $n_2 = 2\pi\chi^{(3)}/n_o$ is the first nonlinear coefficient.

The medium in turn reacts back on the pulse through the intensity dependent refractive index n_2E^2 causing both the pulse radial profile to reduce in size (self-focus) and the pulse spectral components to be modulated and broadened as the pulse propagates.

The occurrence of self-focusing can be seen from the following argument. As the beam profile enters the material it produces a radial index profile ($\Delta n \sim n_2E^2$) which simulates a convergent lens if $n_2>0$. This occurs because the center of the beam moves slower (c/n) than the radial wings. The planes of constant phase become concave into the direction of propagation causing the rays to bend toward the beam axis. This lens deforms the beam profile further into a more concentrated beam. This process continues and leads to a focused beam. Diffraction limits the spot size which is typically between 5 and 20 μ. After the first focus, the beam forms small scale filaments. The formation of these filaments is not yet understood and has been interpreted either as a trapped waveguide[7] or simply as a track of moving focal spots.[8] It is not the purpose of this thesis to investigate the self-focusing models.

The intensity dependent refractive index n_2E^2 also distorts the phase and envelope shape of the pulse resulting in a broadened and modulated spectrum. The change in the spectrum results from both the time rate of change of the phase-self phase modulation and from the frequency components of the sharpened tail of the pulse — self steepening.[9] Since the pulse modifies its own spectra though a change in phase and envelope, these processes are named self-phase modulation and self-steepening, respectively. The effect envelope-shape distortion is negligible[3,9,10] for the sample length (less than 20 cm) used in our study while self-phase modulation has been calculated and shown to produce a modulated frequency broadening in liquids over several hundred wavenumbers in extent.[3,4,10]

Mechanisms in liquids which give rise to the coefficient of the intensity-dependent refractive index n_2 are the orientational Kerr effect, electrostriction, symmetric redistribution, librations, and electronic distortion. In suitably chosen liquids[11] (centro symmetric molecules) these frequency-broadening mechanisms may be distinguished from the electronic mechanism through their different time responses.[11] The relaxation times for these mechanisms are approximately given[11] by

$$\tau \text{ (orientation)} = \frac{4\pi}{3}\eta\, a^3/kT > 10^{-12} \text{ sec}$$

$$\tau \text{ (molecular types)} = \frac{\langle x^2 \rangle}{D} = \frac{6\,\pi\eta a \langle x^2 \rangle}{kT} > 10^{-12} \text{ sec}$$

$$\tau \text{ (libration about field)} = \sqrt{\frac{2I}{\alpha E_o^2}} > 10^{-12} \text{ sec}$$

and

$$\tau \text{ (electronic)} = 2\pi a_o \hbar/e^2 > 1.5 \times 10^{-16} \text{ sec}$$

where η is the viscosity, a is the molecular radius, D is the diffusion coefficient $\geq 10^{-5}$ cm/sec for liquids (for liquids $\eta = 0.4$ cp and glasses $\eta = 10^6$ cp), and x is the diffusion distance of the clustering $\sim 10^{-8}$ cm; I is the moment of inertia $I_{Argon} = 9.3 \times 10^{-38}$ esu and $I_{CCl_4} = 1.75 \times 10^{-38}$ esu, α is the polarizability $\alpha_{Argon} = 1.6 \times 10^{-24}$ esu and $\alpha_{CCl_4} = 1.026 \times 10^{-24}$ esu and E_o is the amplitude of electric field, taken as 10^5 esu which is close to the atomic field. The response time for an electron distortion is about the period of a Bohr orbit $\sim 1.5 \times 10^{-16}$ sec. Thus, typical calculated relaxation-time responses for diffusional motions are $> 10^{-12}$ sec while the electronic distortion response time is $\sim 10^{-16}$ sec.[11] With picosecond light pulses Brewer and Lee[11] have shown that the dominant mechanism for filament formation should be electronic in very viscous liquids. Recently, however, molecular rocking has been suggested as the cause of the broadening and self-focusing in CS_2.[4] The molecules are driven by the laser field to rock about its equilibrium position of a potential well which has been set up by the neighboring molecules. This mechanism is characterized by a relaxation time:

$$\tau_1 = \frac{\eta}{G} = 2.3 \times 10^{-13} \text{ sec},$$

where G is the shear modulus $\sim 1.5 \times 10^{10}$ dynes/cm and viscosity $\eta = 3.7 \times 10^{-3}$ p for CS_2.

In solids, mechanisms giving rise to the coefficient of the intensity-dependent refractive index, n_2, for picosecond pulse excitation are either direct distortion of electronic clouds around nuclei or one of several coupled electronic mechanisms, librational distortion where electronic structure is distorted as the molecule rocks, electron-lattice distortion where the electron cloud distorts as the lattice vibrates, and molecular redistribution where electronic shells are

altered as the nuclei redistribute spatially. The electrostriction mechanism[11,12] is rejected because it exhibits a negligible effect for picosecond pulses.

Rare-gas liquids are composed of atoms possessing spherical symmetry. Thus there are no orientational, librational, or electron-lattice contributions to the nonlinear refractive index coefficient, n_2. However, interrupted rocking of argon atom can occur in which a distorted atom can rock about an equilibrium value before it collides with other atoms. Contributions to the nonlinear refractive index might be expected from electrostriction, molecular redistribution, interrupted rocking, and a direct distortion of the electron clouds: $n_2 = n_{2_{EL}} + n_{2_{MR}} + n_{2_{ROCKING}} + n_{2_{ELECT}}$. Electrostriction is ruled out because picosecond exciting pulses are too short.[11] Molecular redistribution[13] arises from fluctuations in the local positional arrangement of molecules and can contribute significantly to n_2. However, we estimate[14,15] n_2 due to all mechanisms except electronic to be $\sim 1.1 \times 10^{-14}$ esu for liquid argon from depolarized inelastic-scattering data.[16] Electronic distortion ($n_2 = 6 \times 10^{-14}$ esu) slightly dominates all nonlinear index contributions. Furthermore, the depolarized inelastic light scattering wing vanishes in solid xenon,[17] implying that the molecular redistribution contribution to n_2 vanishes in rare-gas solids. Observation of self-focusing and SPM in rare-gas liquids and solids appears to provide a direct proof that atomic electronic shells are distorted from their spherical symmetry under the action of the applied field. However, both pure electronic and molecular redistribution mechanisms are contributing to n_2 in rare gas liquids. The response time of the system for combination of both these mechanisms lies between 10^{-16} and 10^{-12} sec.

2. Self-Phase Modulation in Crystals and Glasses

Experimentally a Nd:glass mode-locked laser is used to generate picosecond light pulses which are then converted in a potassium dihydrogen phosphate (KDP) crystal to the second harmonic at 5300 Å. The laser construction is described fully in Section II. The laser output at 1.06 μ was typically $\sim 5 \times 10^9$ W which was converted to 2×10^8 W at the harmonic, 0.53 μ. The laser output consisted typically of 20 to 60 pulses separated from each other by cavity rounded trip time of 5.5 nsec. The crystal and glasses were polished by the optical shop at GTE Laboratories by Joseph Steiner. No care of flatness or parallelism was taken.

$2 \times 10^{8}/(60^{-11}) \quad 2 \times 10^{-3} = 2\,\text{mW}$

The experimental setup is shown in Fig. III-1. TheSHG beam from KDP was reduced in size to a collimated 1.2 mm diameter beam across the sample by an inverted telescope. The intensity distribution of the light at the exit face of the sample was magnified 10 times and imaged on the 2-mm slit of a Jarrel Ash grating 3/4-m spectrograph. Hence the spectrum of each individual filament within the slit was displayed. Usually there were five to twenty filaments. A thin quartz-wedge beam splitter was used in order to photograph filament formation of the Stokes (anti-Stokes) side of the spectra, three type 3-68 and three type 3-67 (two type 5-60) Corning filters were used to prevent the 5300-Å direct laser light from entering the spectrograph. To reduce nonfilament light, a wire of 2 mm in diameter was sometimes placed at the focal point of the imaging lens. Spectra were taken on Polaroid type 57 film or Kodak type 1N plates.

Typical SPM spectra from various solids are depicted in Figures III-2 through III-9. These photographs were taken on polaroid film with the exception of Fig. III-9 where a Kodak 1N plate was used. The symbols in these figures are defined as follows: F, denotes the filters used near the spectrograph slit; ℓ, denotes the sample length; collimated: 5X, denotes the laser has been collimated and reduced five fold; focused: f, denotes the laser has been focused into the sample with a lens of focal length f; collinear: 10X, denotes that the emission from the sample has been mangified 10X and imaged on the slit; and angular: f, denotes the angular spectra has been obtained from the sample by placing a lens of focal length f, a distance f away from the slit.

Figure III-2 shows the Stokes anti-Stokes spectra from calcite for a collimated 5300 Å beam propagating as an ordinary wave (O-wave) while Fig. III-3 shows the SPM spectra for the 5300 Å beam propagating as extra-ordinary wave (E-wave). Stimulated Raman scattering of 1st and 2nd Stokes are readily observed in these figures. Figure III-4 shows a modulated spectra from calcite. Figure III-5 shows Stokes and anti-Stokes spectra from borosilicate crown (BK-7) and associated filament formation at the exit face, magnified by 10X. Figure III-6 compares the Stokes spectrum observed from various glasses: Light barium crown (LBC-1), extra dense flint (DF-2), and light dense flint (LDF). No filament formation was observed in LBC, DF, and LDF. Figure III-7 and Fig. III-8 show SPM spectra and filament formation from NaCl and quartz crystals, respectively. Figure III-9 compares Stokes SPM emission from flint glass (LDF), quartz, and calcite with a focused laser beam. This photograph (Fig. III-9) was taken on

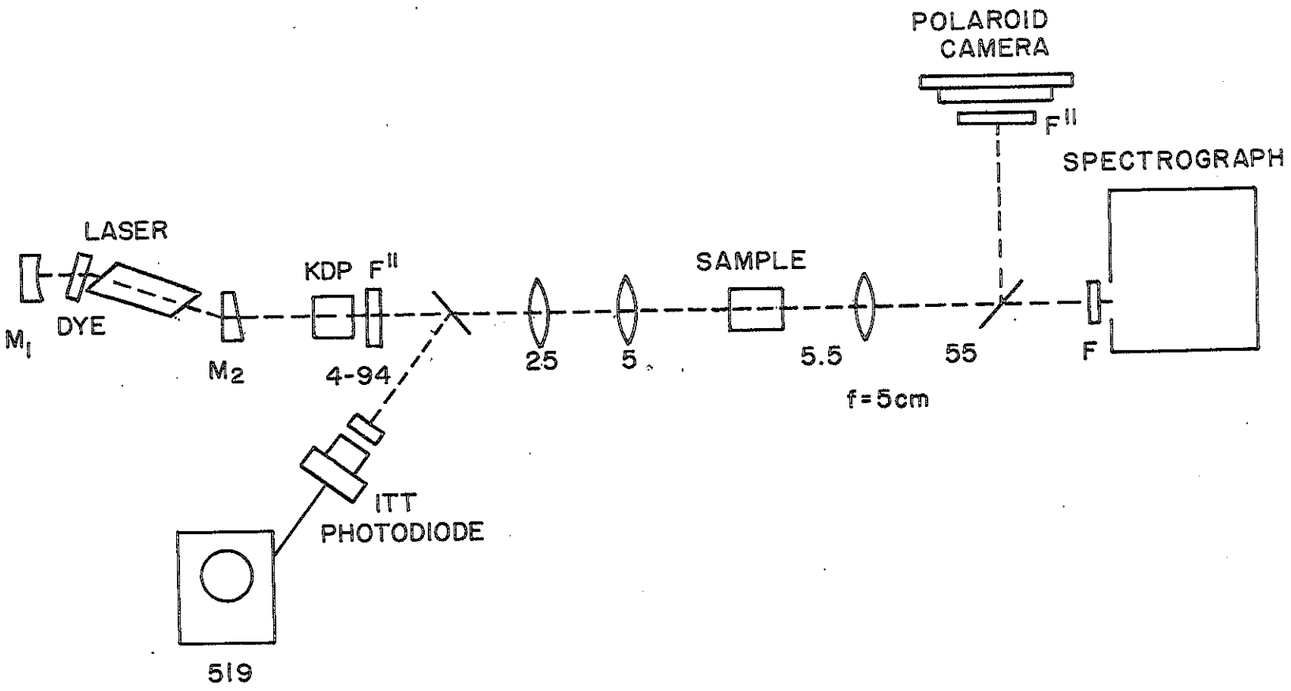

Fig. III-1. Experimental arrangement for observing frequency broadening (SPM), stimulated Raman scattering, and self-focusing.

STOKES

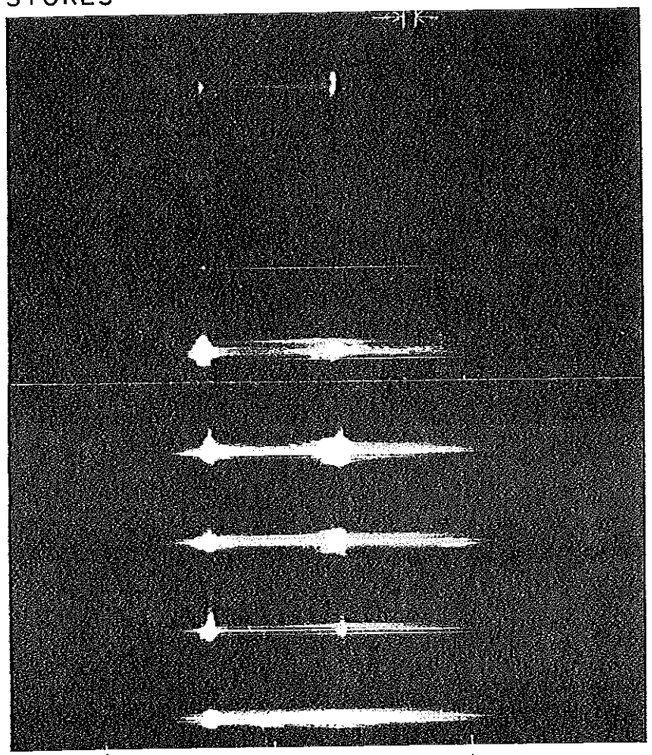

F = 3, (3, 67)
3, (3, 68)
ℓ = 4.5 cm
COLLIMATED = 5x
COLLINEAR = 10x

ANTISTOKES

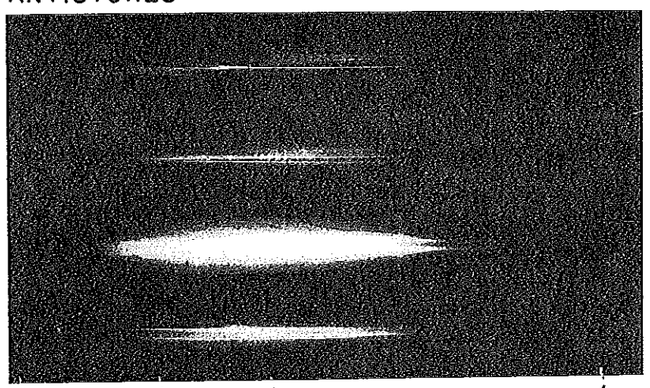

F = 2, (5-60)
ℓ = 4.5 cm
COLLIMATED = 5x
COLLINEAR = 10x

Fig. III-2. Stokes and anti-Stokes SPM spectra from calcite for different laser shots. The laser beam propagates as an O-wave through the sample.

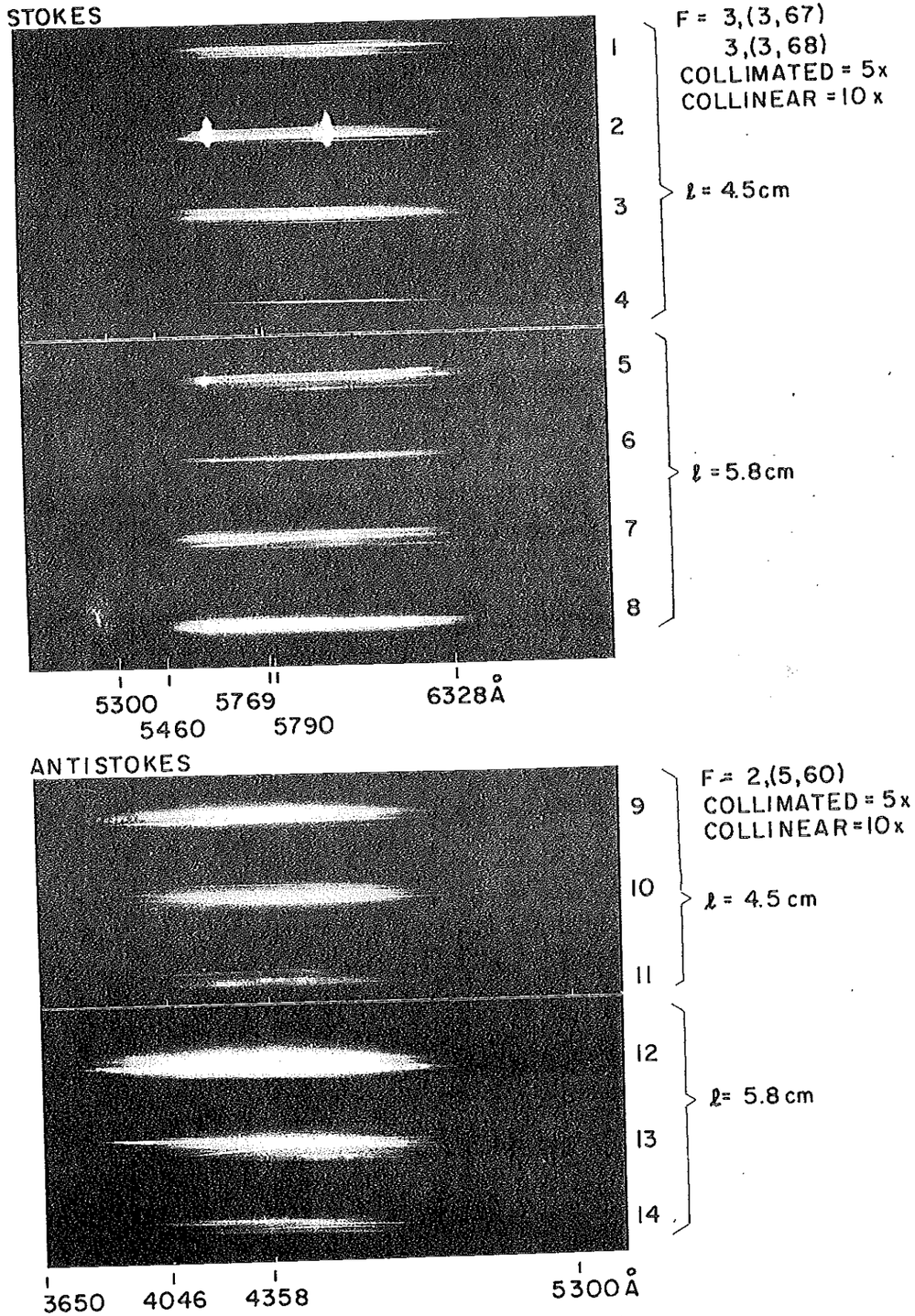

Fig. III-3. Stokes and anti-Stokes SPM spectra from calcite for different laser shots. The laser beam propagates as an E-wave.

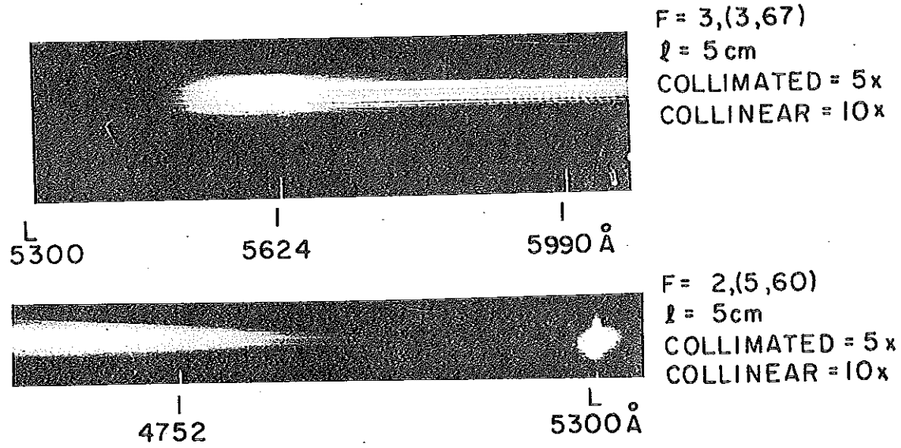

Fig. III-4. Modulated SPM spectra for calcite.

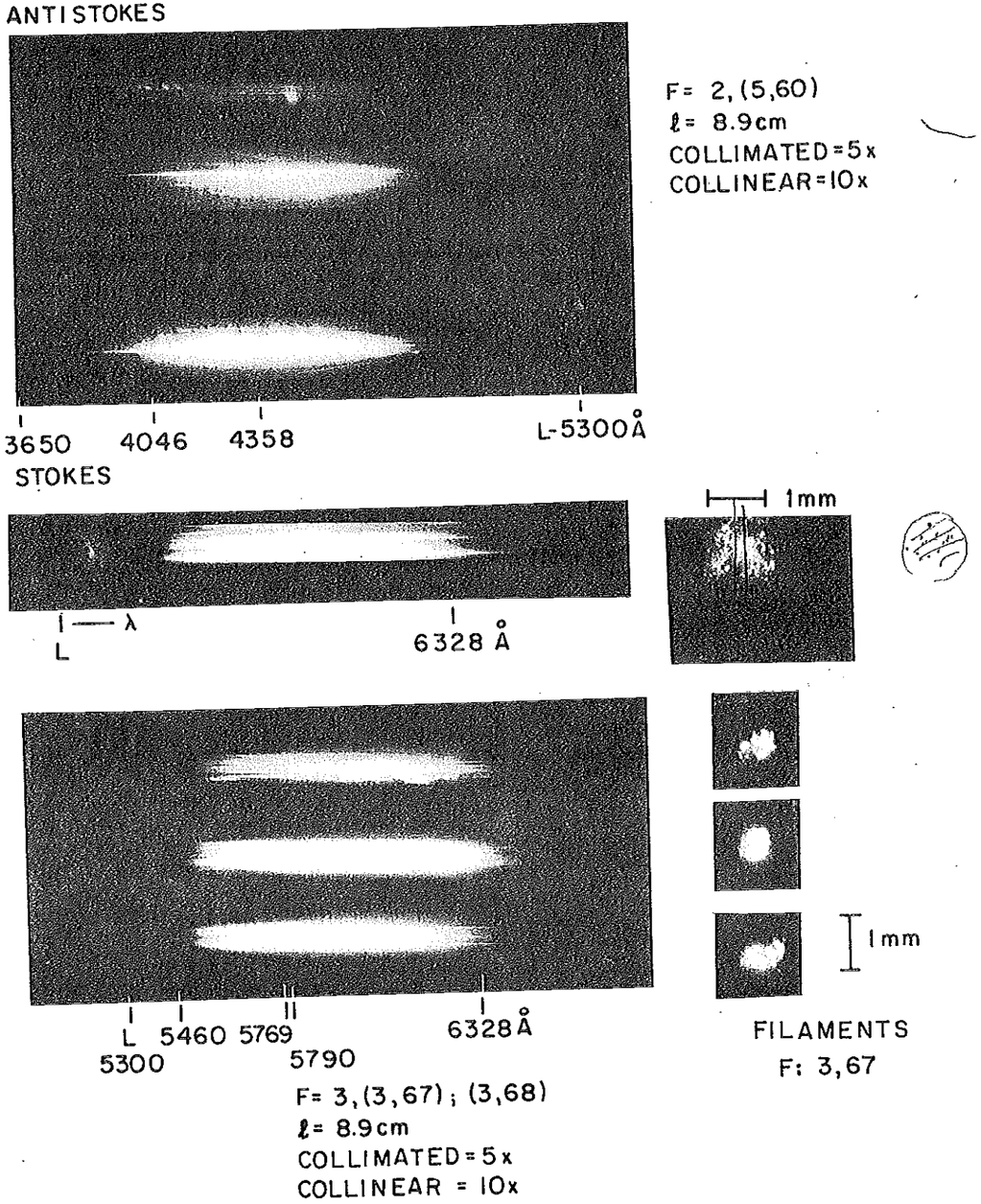

Fig. III-5 Stokes and anti-Stokes from BK-7 glass and filament formation for different laser shots. The filaments are viewed through F': 3-67 filters.

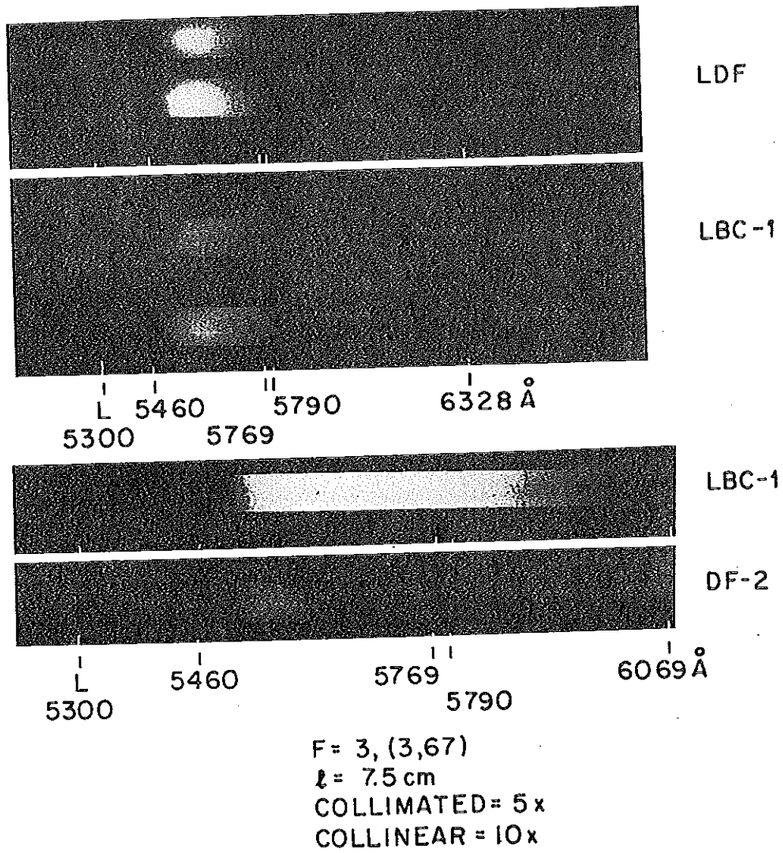

Fig. III-6. A comparison of SPM emission from various glasses: LBC, LDF, and DF-2.

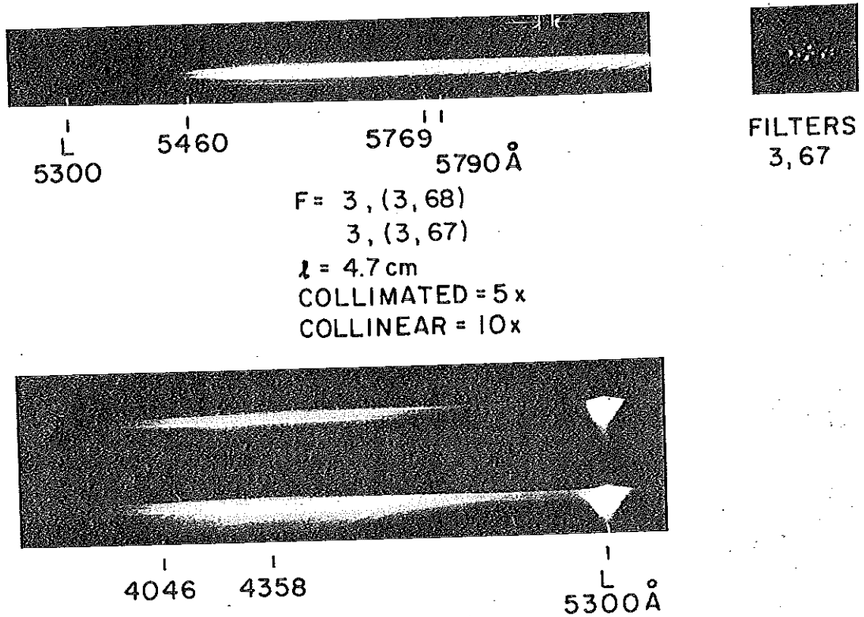

Fig. III-7. SPM emission and filament formation from NaCl.

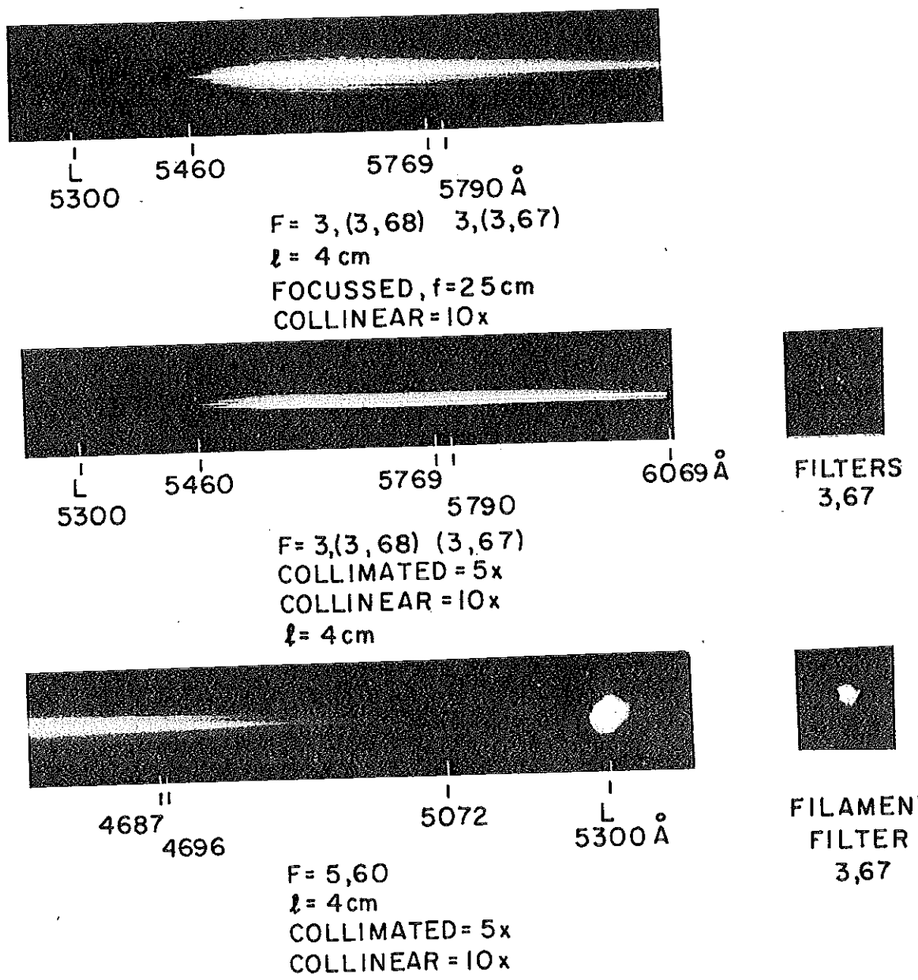

Fig. III-8. SPM spectra and filament formation from a quartz crystal for the laser propagating an O-wave.

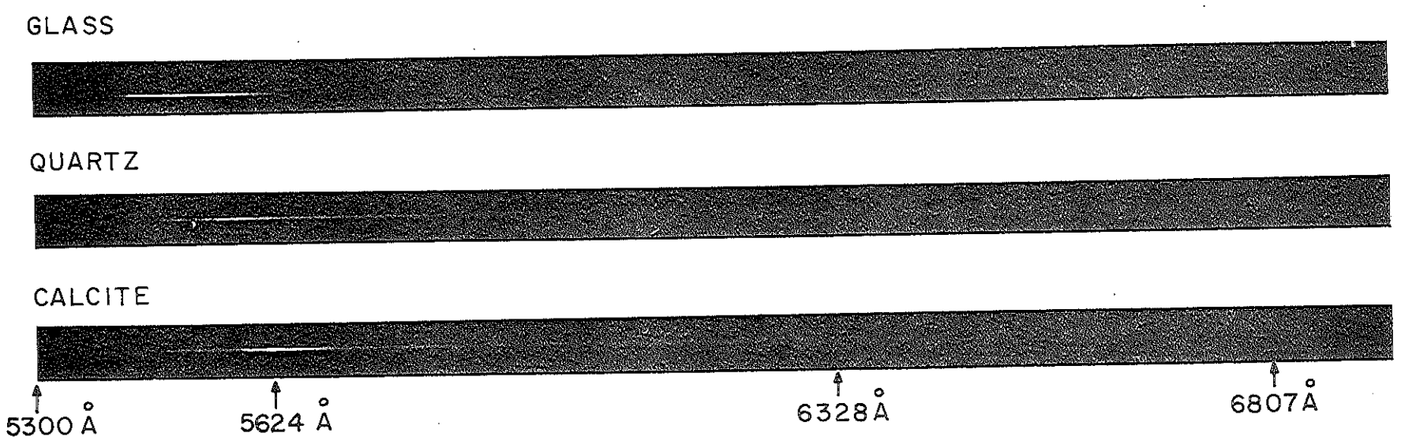

Fig. III-9. A comparison of the extent of the Stokes spectra for flint glass, quartz, and calcite. Kodak N-plate were used. Solid exit face was not focused in the slit. The laser was focused with f = 25 cm into the sample.

1N-plates. The sensitivity of N plates is $\sim 10^2$ less than the sensitivity of type 57-polaroid film in the visible region. The spectra obtained with N-plates is barely visible. However, the spectra sensitivity of N plates extends to ~ 8000 Å while polaroid #57 film is limited to 6400 Å. (The polaroid infrared film could not be adapted to our spectrograph.)

Spectra taken from these samples showed modulation in filaments. The modulation ranged from as small as a few wave numbers to hundreds of wave numbers. The filament size ranged from approximately 5 to 50 μ. Typically five to twenty small-scale filaments were observed. The SPM pulse train consists of a few pulses (~10) occurring prior to the most intense pulses in the laser train. Some laser shots from these samples occasionally did not show modulation or no regular modulation pattern. Typical Stokes sweeps from these filaments were 4400 cm^{-1} in a calcite crystal of length 4 cm, 3900 cm^{-1} in a quartz crystal of length 4.5 cm, 1100 cm^{-1} in extra-dense flint glass of length 7.55 cm, 3900 cm^{-1} in NaCl of length 4.7 cm, and 4200 cm^{-1} in both borosilicate crown (BK-7) and light barium crown (LBC-1) glass of length 8.9 cm. Sweeps on the anti-Stokes side were typically to 6100 cm^{-1} in calcite, 5500 cm^{-1} in quartz, 7300 cm^{-1} in NaCl, and 7400 cm^{-1} in BK and LBC glasses. The anti-Stokes sweeps from the flint glass were not observed probably due to the two 5-60 filters used.

Spectra taken with the collimated beam and with the filaments imaged on the slit were often complicated. Some spectra show parabolic structure with apexes near the center of the spectra with the parabolas going toward the red for Stokes and toward the blue for anti-Stokes. Typical filament spectra show an aperiodic structure similar to that observed by Shimizu[3] although periodic structures similar to those observed by Lifsitz and Grieneisen[10] were sometimes also observed.

In a calcite crystal the threshold for the sweep is lower than the threshold for stimulated Raman scattering (SRS) when the laser travels as an extraordinary (E) wave, but the sweep threshold is higher than the SRS threshold when the laser travels as an ordinary (O) wave. This is demonstrated in Fig. III-10. The SRS threshold is lower for the laser traveling as an O wave than for an E wave by ~3. The length of the frequency sweep is not changed when the collection angle is varied from 0.5 to 10 deg indicating that no parametric fluorescence effect is involved. The sweep is also polarized in the direction of the incident laser polarization. This is also true for unstrained NaCl and glasses. Damage was occasionally

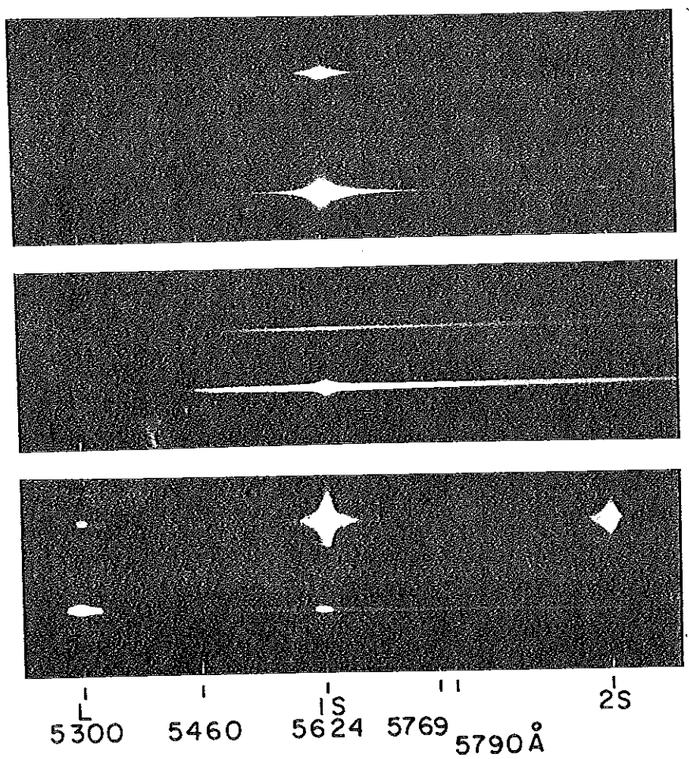

Note: Emission from sample at 40cm away is focussed on slit with (i) f=5cm (ii) f=4cm

Fig. III-10. A comparison of the threshold for SRS and SPM for the laser propagating as O and E waves in calcite. The laser was focused into calcite with f = 25 cm lens. The solid exit face was not imaged on the slit.

observed in calcite but since the emission is modulated, collimated, and polarized it is not produced from dielectric breakdown.

Summarizing the important experimental aspects of the spectra: They are characterized by very large spectral widths and a non-periodic or random substructure. Occasionally a periodic structure of interference minima and maxima are observed. The modulation frequencies range from a few cm^{-1} to hundreds of cm^{-1} and for some modulation progressively increases away from the central frequency. For spectra of less than about 5000 cm^{-1} total width, the spectral extents on the Stokes and anti-Stokes sides are the same within 20 percent. The Stokes and anti-Stokes spectra are approximately equal in intensity and roughly uniform. The peak intensity at the central frequency is $\sim 10^2 - 10^3$ the intensity of the SPM spectra at a given frequency. These results were verified with a prism spectrometer, so that the intensity calibration problems inherent in other instruments were avoided. The spectra also appeared symmetric about the input light frequency when grating instruments were used, but the maximum spectral extent observable with this instrument was about 5000 cm^{-1} and simultaneous observation of Stokes and anti-Stokes spectra for a single laser train was impossible in the case of an extremely large spectral extent. Using spectrographs with only a wire for a filter allowed the display of Stokes and anti-Stokes SPM spectra from the same filaments simultaneously, and under these conditions the maximum spectral on the Stokes and anti-Stokes side was determined to be the same within 20 percent for the maximum shifts from 2000 to 4000 cm^{-1}. The similarity of the spectra observed in different materials strongly suggests a common mechanism for all materials. In Section 4 these experimental results will be shown to imply a relatively fast mechanism and to be consistent with an electronic SPM model.

For relaxation time much less than the laser pulse width, the approximate frequency sweep $\Delta\bar{\nu}$ can be calculated for an isotropic material from[18,19] (see Section 4, Eqs. 18 and 31):

$$\Delta\bar{\nu} \sim 2\delta\bar{\nu} n_2 k E_o^2 \ell, \tag{2}$$

where $\delta\bar{\nu}$ is the spectral width of the pulse, n_2 is the third-order nonlinear refractive index, E_o is the field amplitude, k is the propagation constant, and ℓ is the distance the light propagates through the sample. However, for an

anisotropic crystal the sweep equation is more complicated than (2) because of the tensor form of the susceptibility χ^3 and the polarization of the optical field. Since the third-order susceptibility coefficients are not well known in crystals, only a rough estimate of the sweep span can be made in glass using Eq. (2). Using n_2 for glass[20] of $\sim 3 \times 10^{-13}$ esu, an electric field strength E_o of 1.3×10^4 (2×10^{10} W/cm^2; 2×10^8 W in 1 mm^2), $\delta\bar{\nu}$ the spectral width of the pulse of 100 cm^{-1}, an estimated active length of 4 cm, and $k = 1.18 \times 10^5$ cm^{-1}, the calculated sweep for glass is $\Delta\bar{\nu} \sim 2400$ cm^{-1}, and the change in refractive index $\delta n = \frac{1}{2} n_2 E_o^2$ is 0.26×10^{-4}. This agrees with estimated change in refractive index, δn, corresponding to a 20 μ diameter filament,[21] is $\geq \left(\frac{1}{8n_o}\right)\left(\frac{1.22\lambda}{d}\right)^2 = 0.7 \times 10^{-4}$.

Electronic-librations mechanism for the SPM is not possible in NaCl, and electronic-lattice distortion is ruled out in glasses. However, all the coupled-electronic mechanisms can contribute in calcite and quartz.

With a large power density, $\sim 10^4$ GW/cm^2, in the filaments, multiphoton effects such as four-photon processes may be taking place.[22] This led to a search for a four-photon parametric emission. This observation is discussed in Section IV.

The large frequency sweeps obtained in crystals indicate that these materials might be used as ultrafast light gates with response times of $\sim 10^{-15}$ sec, an improvement in response of 10^3 over the molecular-orientation light gate introduced by Duguay and Hansen.[20] Self-phase-modulation processes are probably present inside mode-locked lasers.[23]

3. Self-Phase Modulation in Rare Gas Liquids and Solids

The same mode-locked laser described previously in Section III-2 and II-1 is used as the exciting source for this study. The experimental arrangement is shown in Fig. III-11.

The second harmonic pulses of power $\sim (2.5\text{-}8) \times 10^8$ W are focused with a 25-cm focal length lens into 12-cm-long samples of argon and krypton. The beam intensity in the liquids is $\sim 4 \times 10^{11}$ W/cm^2 over a beam waist length of ~ 7 cm. The beam diameter is photographically measured to be 300 μm at the focal point and 400 μm at 3.5 cm to both sides from the focal distance. A collimated beam of diameter 1.1 mm could not produce SPM. Filaments are imaged onto a 3/4-m Jarrell-Ash spectrograph where the spectra are recorded on

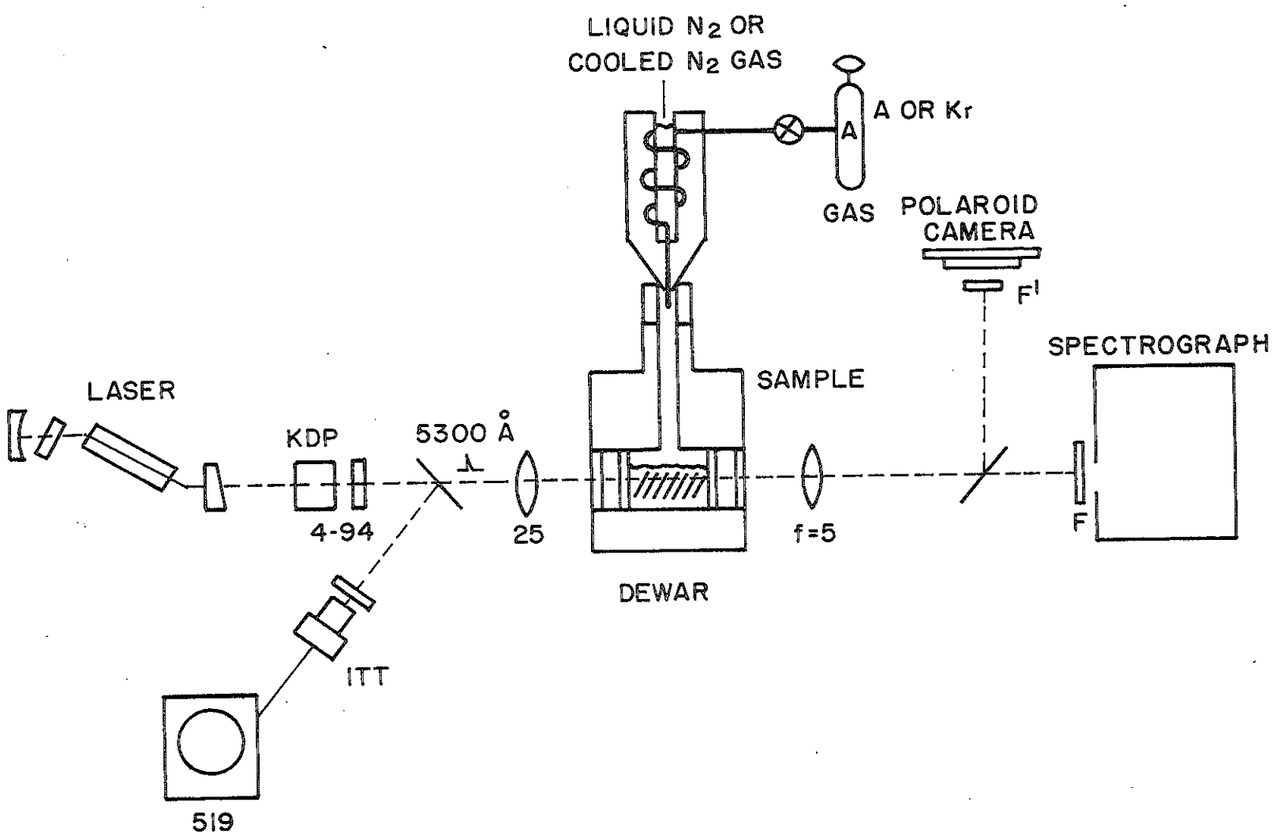

Fig. III-11. Experimental arrangement for observing nonlinear effects in liquified and solidified rare gases.

Polaroid type 57 film. A glass beam splitter deflects a portion of the beam onto a camera where the filaments are simultaneously photographed.

Liquid argon is condensed from Linde research grade gas into an optical Dewar. Liquid krypton is condensed similarly, and solid krypton is grown by slowly lowering the temperature below the freezing point of krypton. All samples appear perfectly clear to the eye. No visible imperfections are observed in krypton solids. The solid is probably composed of large single crystals of size ~1 mm since the growth technique is similar to that of Bolz, Broida, and Peiser.[24]

Spectra showing frequency broadening and SPM from liquid argon and liquid and solid krypton are shown in Figs. III-12 through III-15. Sweeps of 1000 to 6000 cm^{-1} are observed to both the red and blue sides of 5300 Å in liquid argon. Similar spectral sweeps are observed in liquid and solid krypton. Some spectra as shown in Fig. III-12 show a complicated modulated radial structure within the broadened spectra, while other filament spectra show periodic modulation — some show no modulation, others show a non-regular or random modulation — see Figs. III-13 through III-15 for different laser shots. The modulation ranges from a few cm^{-1} to hundreds of cm^{-1}.

A most important point is that the threshold for observing SPM in liquid krypton is 0.64 ± 0.12 that of liquid argon; also the SPM threshold ratio of solid to liquid krypton is 0.86 ± 0.15. In liquid argon, SPM spectra appear at a threshold power of ~0.5 GW focused in a 12-cm sample. At threshold the SPM pulse train consists of a few pulses occurring prior to the most intense pulses in the laser train. This may be because pulses in the laser train broaden in frequency[23] and lengthen in time through the train.[25] Normally three to ten small-scale filaments of 5 to 20 μm in diameter are observed. Sometimes filaments are accompanied by concentric rings progressively weaker in intensity[26] of typical diameters of ~200 and ~350 μm. No large change in shape of the laser pulse train appears upon passage through the sample as displayed on a 0.5-nsec resolution Tektronix 519 scope. The swept light is also collimated, polarized, and modulated. These observations rule out dielectric breakdown.

To explain these results the following argument is presented which estimates the nonlinear index n_2, self-trapping length, critical self-trapping power, and sweep length. For spherically symmetric atoms the induced dipole moment p may be expressed as a function of the local field E_L in the form[27]

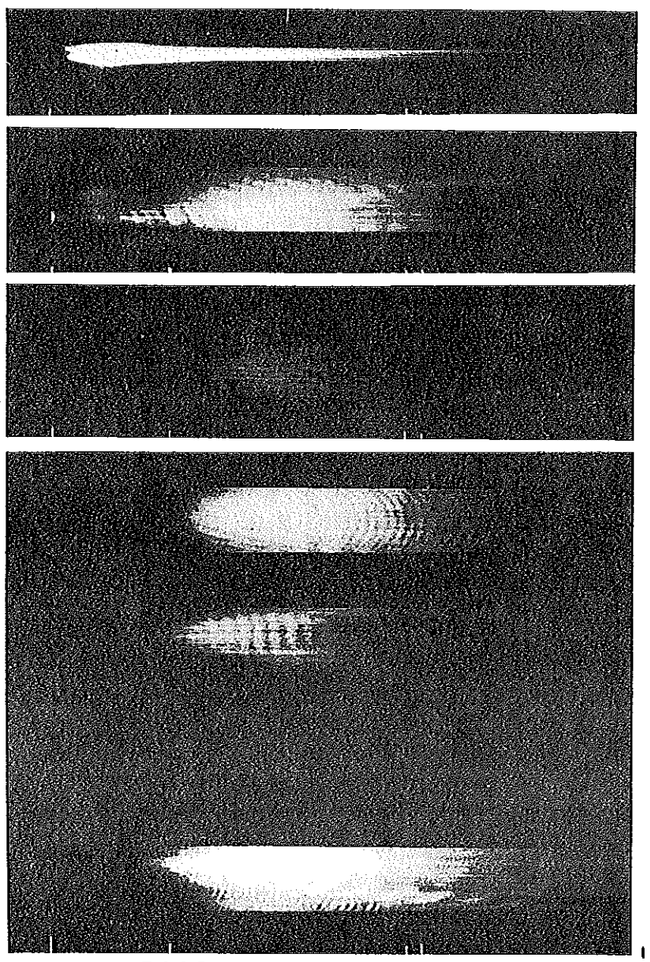

Fig. III-12. Stokes SPM from liquid argon for different laser shots. The laser was focused into the sample with f = 25 cm lens. The exit face was focused on the slit, magnified 10X.

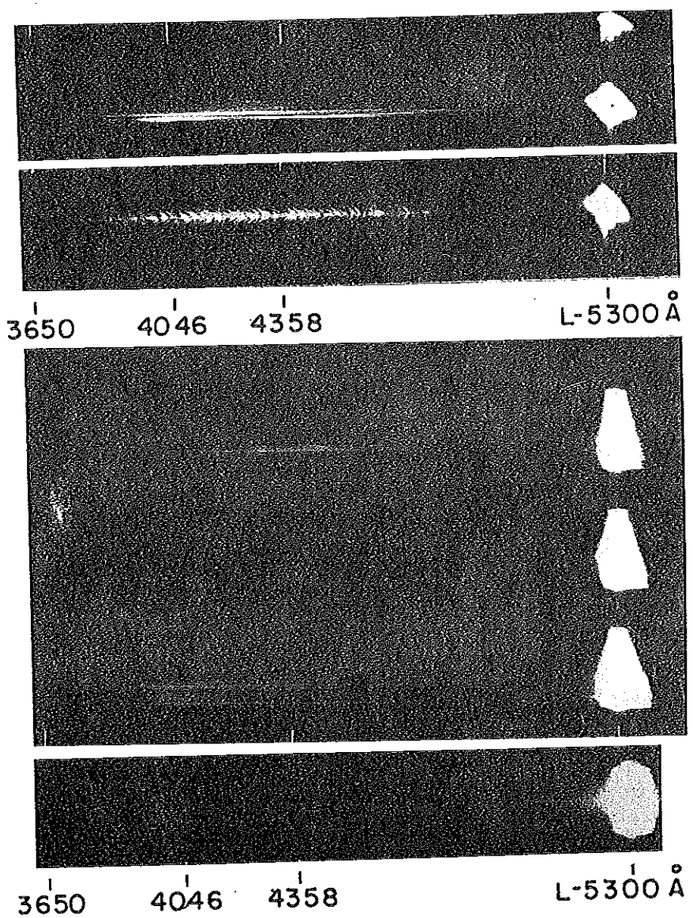

F = (5,60)
ℓ = 7 cm
FOCUSSED = 10 cm
COLLINEAR = 10x

F = (5,60)
ℓ = 7 cm
FOCUSSED = 25 cm
COLLINEAR = 10x

F = (5,60)
ℓ = 7cm
FOCUSSED = 10cm
COLLINEAR = 10x

F = (5,60),(5,61)
ℓ = 12cm
FOCUSSED = 25cm
COLLINEAR = 10x

Fig. III-13. Anti-Stokes SPM for liquid argon for different laser shots. The laser was focused into the samples with f = 25 cm lens. The exit face was focused on the slit, magnified 10X.

KRYPTON:STOKES

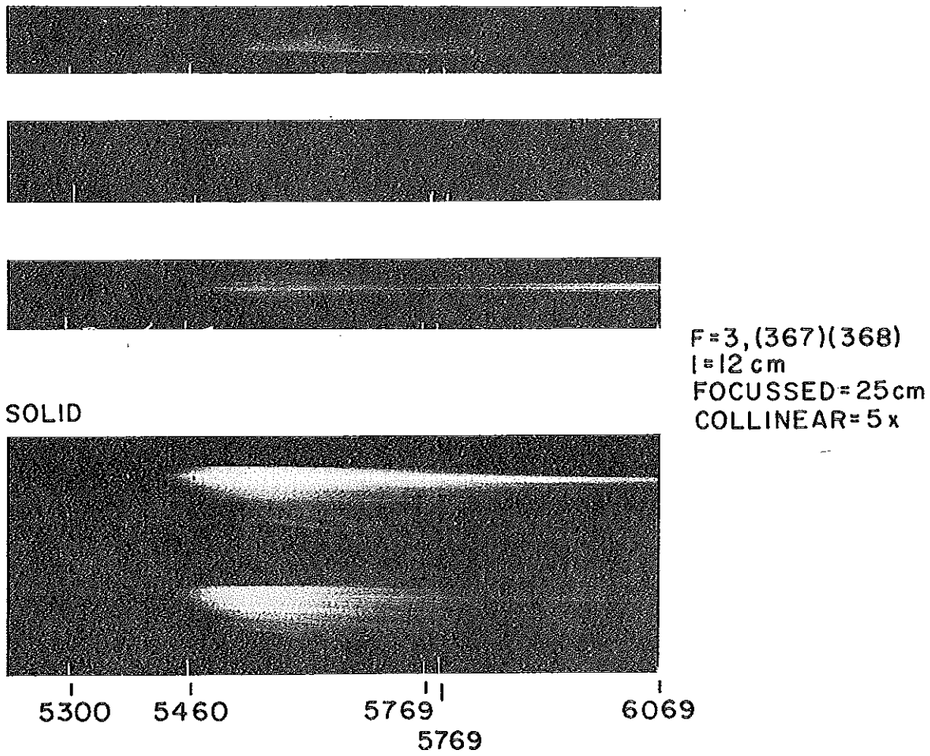

Fig. III-14. Stokes SPM for liquid krypton for different laser shots. The laser was focused into the samples with f = 25 cm lens. The exit face of the samples was imaged on the slit, magnified 10X.

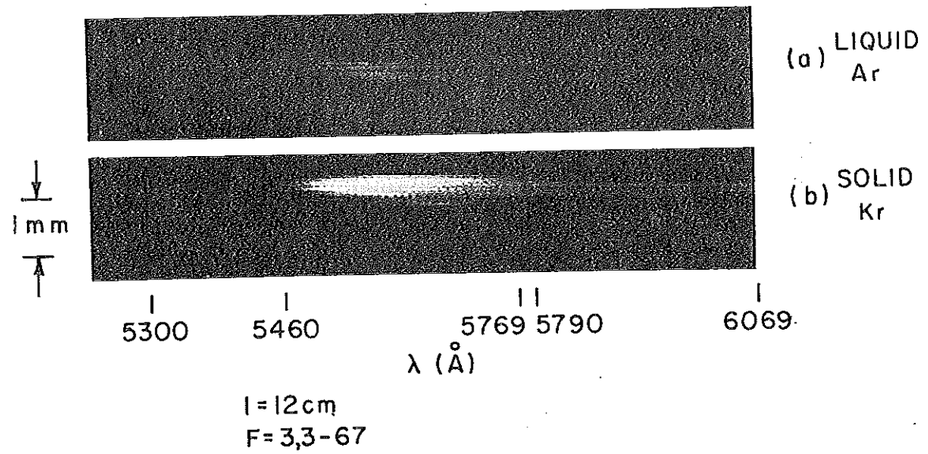

Fig. III-15. A comparison of typical Stokes SPM spectra for liquid argon and solid krypton. The laser is focused with f = 25 cm and the sample exit face is imaged on the slit, magnified 10X.

$$p = \alpha_o E_L + \frac{1}{6}\gamma E_L^3 + \cdots, \tag{3}$$

where α_o is the polarizability and γ is known as the second order hyperpolarizability. The βE_L^2 term vanishes because of inversion symmetry of spherical atoms. The term γ represents electronic distortion which occurs only at intense electric fields. Taking a metallic sphere as a model for a spherical atom, the hyperpolarizability is given by[28]

$$\gamma = \left[\frac{4}{5}\alpha_o \frac{(a-b)}{R} + \alpha_o \frac{\Delta V}{V}\right] \frac{2}{E_L 2}, \tag{4}$$

where R is the radius of the undistorted atom, and a and b are the semiaxes of the deformed sphere. The terms in Eq. (4) arise from a change in polarizability due to a change of shape and of volume of the atom. Experimental values of γ are known for He, Ne, Ar, and Kr and are in close agreement with theoretical values.[27,29,30] The experimental values[30] of γ for liquid argon and liquid krypton are 5.9×10^{-37} and 14×10^{-37} esu, respectively.

The refractive index[13] in rare-gas liquids is given by $n_\parallel \equiv n_o + n_2\langle E^2\rangle$ where $n_\parallel$ is the refractive index parallel to the field, $\langle E^2\rangle^{1/2}$ is the rms value of the electric field, and $\vec{E} = \frac{1}{2} E_o \hat{e}_\parallel (e^{i\omega t} + c.c)$. The electronic nonlinear refractive index in rare gas liquids is given by[31]

$$n_2 = [(n_o^2 + 2)^4/81\, n_o]\pi N\gamma, \tag{5}$$

where n_o is the refractive index, and N is the number of atoms per unit volume. The term n_2 is $\cong 0.6 \times 10^{-13}$ esu in liquid argon and $\cong 1.36 \times 10^{-13}$ esu in liquid krypton. For liquid argon, liquid krypton, and solid krypton the refractive indices are taken as 1.23, 1.30, and 1.35, respectively.[32]

Intense electric fields distort atoms and produce a birefringence. The anisotropy in refractive index between light traveling with wave vector parallel and perpendicular to the applied electric field is given by[27,33]

$$\delta n_\parallel - \delta n_\perp = \frac{1}{3} n_2 E_o^2, \tag{6}$$

where $\delta n_\parallel$ and $\delta n_\perp$ are the changes in refractive indices parallel and perpendicular to the field and $\delta n_\parallel = 3\delta n_\perp$ for electronic processes in spherical atoms.[27,30] The value of this difference is $\sim 5 \times 10^{-5}$ liquid argon at $E_o \sim 1.5 \times 10^7$ V/cm

($\sim 4 \times 10^{11}$ W/cm^2). This change in index can lead to self-trapping and, because of the high intensity in the filament, SPM.

The critical power for self-focusing[7] and the self-focusing length[34] are given by

$$P_{crit} \geq (1.22\,\lambda)^2 c/64 n_2, \tag{7}$$

and

$$\ell = \frac{a}{2}\left[\frac{2n_o}{n_2}\right]^{1/2} \frac{1}{E_o}\,. \tag{8}$$

For liquid argon with a, the beam radius, taken to be 150 μm and E_o as 1.5×10^7 V/cm, the values 3.3 MW and 10 mm are obtained for P_{crit} and ℓ. The self-focusing length is less than the beam waist length in our experiment. This shows that hyperpolarizabilities are clearly large enough at mode-locked laser powers to observe self-focusing caused by the electronic distortion effect.

An estimate of the sweep length[18,19] $\Delta\bar{\nu}$ in liquid argon is given by (see Eq. 31)

$$\Delta\bar{\nu} \cong \delta\bar{\nu} n_2 k E_o^{\,2} \ell \sim 1.2 \times 10^4 \text{ cm}^{-1}, \tag{9}$$

where $\delta\bar{\nu}$, the spectral width of the pulse, is taken as 100 cm^{-1}; ℓ, the active sample length, is taken as the beam waist length of ~7 cm; and k, the propagation constant, is 1.18×10^5 cm^{-1}.

Since P_{crit} goes as γ^{-1}, Eq. (7) shows that the self-trapping threshold for liquid krypton should be lower than that of liquid argon. This is experimentally observed. Since self-trapping thresholds differ slightly in liquid and solid krypton, direct distortion and not molecular redistribution produce SPM. This result also provides a strong argument that electron-lattice distortion is apparently not playing much of a role in SPM from solid krypton. Rather, the reason that solid krypton has a slightly lower SPM threshold than liquid krypton can probably be attributed to its higher density (16%) and higher refractive index contribution (10%). The physical reason for γ in krypton being ~2.4 times larger than for argon is that the outer electron shell for rare-gas atoms is less tightly bound, and hence, more distortable as Z increases.

Summarizing, calculations and experimental results show that the electronic contribution to n_2 is (1) large enough to cause SPM and self focusing and (2) slightly larger than the other mechanisms — molecular translation and rotation — by a factor of 3.

4. Theoretical Analysis of Self-Phase Modulation

In this section the spectrum of an intense optical pulse is calculated after traveling a distance in an isotropic material. The characteristics of the spectrum for different parameters of the pulse and of the material are compared with the experimental observed spectrum. The spectrum is calculated for mechanism which respond to the envelope of the mode-locked pulse, to the sub-picosecond component of the pulse,[35] and to the optical frequency components.

Qualitative features of the spectrum[3] and a physical understanding of the broadening process are obtained by first approximately calculating the spectra by Stoke's method of stationary phase.[36]

The electric field of the input laser beam is assumed to be given by

$$E(t) = \frac{1}{2} E_o(t)\, e^{-i\,(\omega_L t - z\omega_L/c)} + c.c \tag{10}$$

where $E_o(t)$ is the envelope of the pulse taken to be a gaussian e^{-t^2/T^2} where $T_p = (2\ell n2)^{1/2} T$ is the FWHM of the laser pulse width, and ω_L is laser angular frequency. The electric field of the laser beam in the time domain after traveling a distance z in the material is given by

$$E(t) = \frac{1}{2} E_o(t)\, e^{-i\,(\omega_L t - n(t)\, z\, \omega_L/c)} + c.c \tag{11}$$

where n is the total refractive index. The instantaneous phase of the light wave is given by

$$\varphi = \omega_L t - n(t)\, \omega_L z/c \tag{12}$$

Following Shimizu,[3] the spectral amplitude of the light pulse is given by the Fourier transform

$$E(\omega) = \frac{1}{2\pi}\int_{-\infty}^{\infty} E(t)\, e^{i\omega t}\, dt = \frac{Re}{2\pi}\int_{-\infty}^{\infty} E_o(t)\, e^{-i(\omega_L t - \omega_L nz/c)}\, e^{i\omega t}\, dt \qquad (13)$$

Substituting $n = n_o + \delta n$ Eq. (4) becomes

$$E(\omega) = \frac{Re}{2\pi}\, e^{in_o\omega_L z/c}\int_{-\infty}^{\infty} E_o(t)\, e^{i\left[(\omega-\omega_L)t + \omega_L z\,\delta n/c\right]}\, dt \qquad (14)$$

where δn is the nonlinear part of refractive index. The integral (Eq. (14)) is of the type

$$f(x) = \int_{\alpha}^{\beta} g(t)\, e^{ixh(t)}\, dt \qquad (15)$$

which can be approximately evaluated by the method of stationary phase.[36] In the first approximation of this method the main contribution of the value of the integral arises from the immediate vicinity of those points (τ) called critical points at which h(t) is stationary $h'(t)\Big|_{t=\tau} = 0$

That is

$$f(x) \sim \int_{\tau-\epsilon}^{\tau+\epsilon} g(t)\, e^{ixh(t)}\, dt = \left(\frac{2\pi}{xh''(\tau)}\right)^{1/2} g(\tau)\, e^{(ixh(\tau) + i\pi/4)} \sim \frac{1}{z^{1/2}} \qquad (16)$$

$E \sim 1/z$ poly

where ϵ is small and h is real.[36] Setting $h(t) = (\omega-\omega_L)\,t + \omega_L z\,\delta n/c$ and $x = 1$, then the main contribution to the integral (Eq. 14) occurs when $h'(t) = 0$ = $\omega - \omega_L + \frac{\omega_L z}{c}\left(\frac{\partial(\delta n)}{\partial t}\right)$.

Beer law $E = e^{-\alpha z}$

Therefore, the critical points (τ) are defined by

$$\omega - \omega_L = \frac{-\omega_L z}{c}\,\frac{\partial(\delta n)}{\partial t} \qquad (17)$$

In this approximation we assume that mechanism for δn responses to envelope of picosecond pulse ($\delta n \sim E_o^2(t)$ bell-shaped but not necessarily symmetrical. A schematic representation of δn versus time is shown in Fig. III-16a.

The maximum frequency broadening on Stokes and antistokes occurs at the inflection points t_1 and t_2 as shown in Fig. III-16b

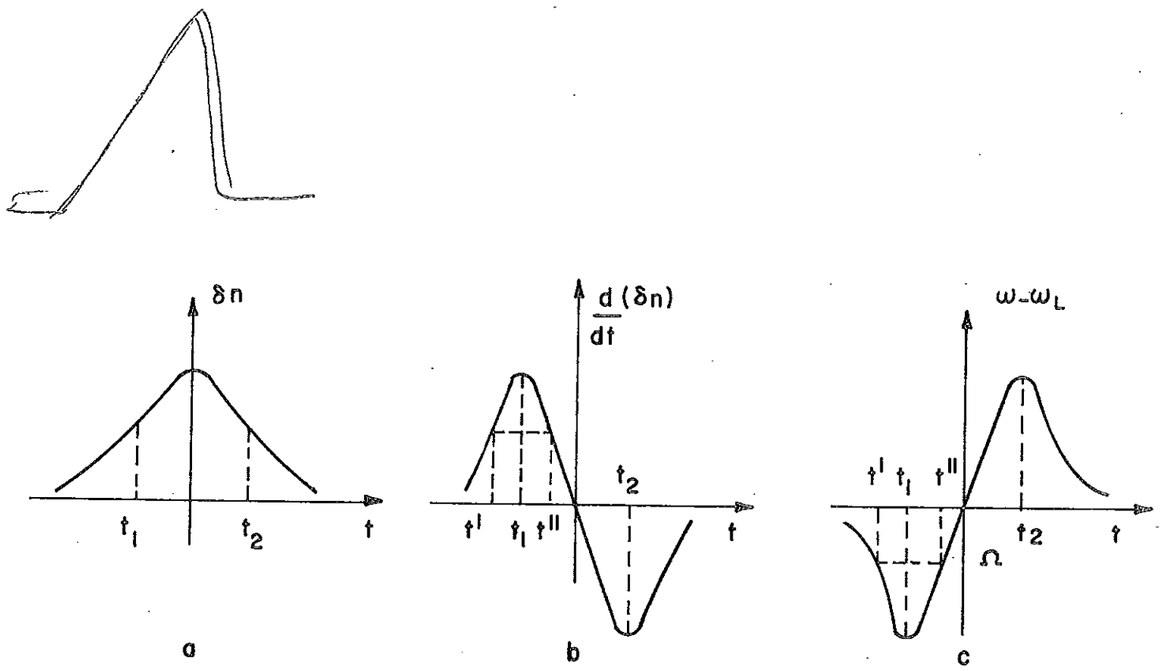

Fig. III-16. A simple mechanism for SPM for nonlinear index following the envelope of symmetrical laser pulse; (a) nonlinear index change versus time; (b) time rate of change of index change; (c) frequency change versus time.

$$\Delta\omega^{S}_{Max} \equiv \omega_S - \omega_L = \frac{-\omega_L z}{c} \frac{\partial(\delta n)}{\partial t}\Bigg|_{t=t_1} \qquad \text{(Stokes)} \qquad (18)$$

$$\Delta\omega^{AS}_{Max} \equiv \omega_{AS} - \omega_L = \frac{-\omega_L z}{c} \frac{\partial(\delta n)}{\partial t}\Bigg|_{t=t_2} \qquad \text{(Antistokes)}$$

From these equations the following facts are obtained: (1) If the maximum frequency length are not equal δn is not symmetrical; (2) the same frequency shift occurs at two times t' and t''

$$\omega - \omega_L = \frac{-\omega_L z}{c} \frac{\partial(\delta n)}{\partial t}\Bigg|_{t'} = \frac{-\omega_L z}{c} \frac{\partial(\delta n)}{\partial t}\Bigg|_{t''} \qquad (19)$$

This is depicted in Fig. III-16c. The main contribution to integral (Eq. 14) comes from two time points t' and t'' satisfying Eq. 17. Using method stationary phase phase Eq. 14 becomes

$$E(\omega) = \frac{Re}{2\pi} e^{i n_o \omega_L z/c} \left[\left(\int_{-\infty}^{a} dt + \int_{a}^{\infty} dt \right) \left(E_o e^{i\left((\omega-\omega_L) t + \omega_L z \delta n/c \right)} \right) \right] \qquad (20)$$

where $t' < a < t''$.

Therefore using Eq. 16:

$$E(\omega) = Re \left(\frac{2\pi c}{\omega_L z} \right)^{1/2} e^{i(n_o \omega_L z/c + \pi/4)}$$

$$\left\{ \frac{E_o(t')\, e^{i\left((\omega-\omega_L)t' + \frac{\omega_L n_o z\, \delta n(t')}{c} \right)}}{\left(\frac{d^2}{dt^2}(\delta n) \right)^{1/2}_{t'}} + \frac{E_o(t'')}{\left(\frac{d^2}{dt^2}(\delta n) \right)^{1/2}_{t''}} e^{i\left((\omega-\omega_L) t'' + \frac{\omega_L n_o z\, \delta n(t'')}{c} \right)} \right\} \qquad (21)$$

The spectrum intensity is given by:

$$S(\omega) = \frac{c}{4\pi} \left| E(\omega) \right|^2 \tag{22}$$

Therefore

$$S(\omega) = \left(\frac{c}{4\pi}\right)\left(\frac{2\pi c}{\omega_L z}\right) \left\{ \frac{\left|E_o(t')\right|^2}{\left(\frac{d^2(\delta n)}{dt^2}\right)_{t'}} + \frac{\left|E_o(t'')\right|^2}{\left(\frac{d^2(\delta n)}{dt^2}\right)_{t''}} \right.$$

$$\left. + \frac{2\, E_o(t')\, E_o(t'')}{\left(\frac{d^2 \delta n}{dt^2}\right)_{t'}^{1/2} \left(\frac{d^2 \delta n}{dt^2}\right)_{t''}^{1/2}} \cos\left[(\omega-\omega_L)t' + \omega_L z\, \delta n(t')/c - (\omega-\omega_L)t'' - \omega_L z\, \delta n(t'')/c\right] \right\} \tag{23}$$

The last term of Eq. 23 produces the periodic structure in the spectrum via interference. The spectrum intensity has minimum when the two point t' and t'' are 180° out of phase and they cancel each other out by interference. This occurs when

$$(\omega-\omega_L)t' + \frac{\omega_L z\, \delta n(t')}{c} - (\omega-\omega_L)t'' - \frac{\omega_L z\, \delta n(t'')}{c} = (2m-1)\pi \tag{24}$$

where $m = 1, 2, 3 \ldots$. A maximum in $S(\omega)$ for

$$(\omega-\omega_L)t' + \frac{\omega_L z\, \delta n(t')}{c} - (\omega-\omega_L)t'' - \frac{\omega_L z\, \delta n(t'')}{c} = 2r\pi \tag{25}$$

where $r = 0, 1, 2, 3 \ldots$ and the two points t' and t'' are in phase and constructively interfere.

An estimate of modulation frequency in the broadened spectra can be made by calculating the maximum number of interference minimum, M, in the spectra and divide this into the maximum frequency broadening. Notice that no frequency shift (in the envelope approximation) occurs at $t = \pm\infty$ and $t = 0$ where $\delta n = 0$ and $d/dt(\delta n) = 0$ occurs respectively. (See Figure 16). Taking $t' = 0$ and $t'' = -\infty$, Eq. (24) reduces to

$$\frac{\omega_L z\, \delta n(o)}{c} = (2M-1)\pi. \tag{26}$$

Therefore, the maximum number of minimum on the spectra is

$$M = \frac{1}{2}\frac{\omega_L z\, \delta n(o)}{c\pi} + \frac{1}{2} \tag{27}$$

For typical experimental values of z and δn (i.e., $z \sim 1$ to 5 cm, $\delta n \sim 10^{-3}$ to 10^{-5} esu, and $\omega_L/2c\pi = 1.9 \times 10^4$ cm^{-1}), the number of minimum that appears in the spectra may range from as high as 100 to as low as none (0.6).

An estimate of the modulation frequency of periodic structure in SPM spectral on the Stokes side is

$$\delta\omega_M \sim \left|\frac{\Delta\omega^S_{max}}{M}\right| = \frac{-\frac{\omega_L z}{c}\frac{\partial(\delta n)}{\partial t}\Big|_{t'}}{\frac{1}{2}\frac{\omega_L z}{c\pi}\delta n(o) + \frac{1}{2}} \tag{28}$$

and

$$\delta\omega_M \sim \frac{2\pi\frac{\partial}{\partial t}(\delta n)\Big|_{t'}}{\delta n(o)}$$

Taking $E_o(t) = E_o e^{-t^2/T^2}$ where $T_p = (2\ln 2)^{1/2} T = T_f\sqrt{2}$ is the intensity FWHM of the pulse and T_f is the field FWHM, and assuming an envelope response time mechanism: $\delta n = \frac{n_2 E_o^2}{2} e^{-2t^2/T^2}$, $\frac{\partial(\delta n)}{\partial t}\Big|_{t'=T/2} = \frac{1.2\, n_2 E_o^2}{2T}$. These parameters are substituted into Eq. 29 to obtain the modulation frequency:

$$\delta\omega_M = \frac{2\pi\,(1.2)}{T} = \frac{2\pi\,(2)}{T_p}\ \text{sec}^{-1} \tag{30}$$

and into Eq. 18 to obtain the maximum frequency extent:[37]

$$|\Delta\omega_{max}| \sim \frac{\omega_L}{T_p C} n_2 E_o^2 z\ \text{sec}^{-1} \sim \omega.$$

or

$$|\Delta\bar{\nu}_{max}| \sim \frac{1}{2\pi C} n_2 E_o^2 \frac{z}{\tau} \text{ cm}^{-1}. \tag{31}$$

The modulation frequency in wavenumbers is $\delta\bar{\nu}_m = \frac{2}{T_p C}$. For $T_p = 10^{-12}$ sec, $\delta\bar{\nu}_m = 67$ cm^{-1}, and for $T_p = 10^{-13}$ sec, $\delta\bar{\nu}_m = 670$ cm^{-1}. Notice, the shorter the T_p the larger the modulation frequency of the periodic structure. The maximum frequency extent for this model in wavenumbers is $\Delta\bar{\nu}_{max} = 125$ cm^{-1} for $T_p = 10^{-12}$ sec and $\Delta\bar{\nu}_{max} = 1250$ cm^{-1} for $T_p = 10^{-13}$ sec. (The following parameters were used: $z = 2$ cm, $n_2 E_o^2 = 10^{-4}$ and $\omega_L/c = 1.18 \times 10^5$ cm^{-1}.) Therefore, the shorter duration pulse produces the widest frequency extent with the least internal periodic structure.

The remaining part of this section is devoted to the calculation of the spectrum intensity for n_2 responding to (I) the envelope of a mode-locked pulse ($T_f = 4$ psec), (II) sub-picosecond components of noise pulses within the mode-locked pulse [35,38] (0.1 - 1.0 psec), and (III) pure electronic response with no $3\omega_L$, $5\omega_L$, $7\omega_L$ ... wave propagation due to absorption ($\lambda < 1770$ Å) in the material.

The experimental results of sections 2 and 3 may be used to determine an upper limit for the relaxation time τ of the index nonlinearity mechanism. Using the form of equation 18 for an estimate of the maximum frequency extent and substituting τ^* for T_p gives $\Delta\omega_{max} \sim \frac{\omega_L}{c\tau^*} n_2 E_o^2 z$. Here τ^* is the shortest time in which the nonlinear index changes significantly. Typically about 4000 cm^{-1} broadening on either side for active length[39] $z \sim 0.2$ cm in various materials are observed, and $n_2 E_o^2$ is estimated to be $< 10^{-3}$ esu from Kerr gate experiments[20] and from the diameter of the observed filament. Therefore the mechanism relaxation time must be $\tau^* \leq 3 \times 10^{-14}$ sec. This relaxation is faster than the molecular type of motions.

The general form for the nonlinear refractive index[3] with quadratic field dependence is

$$n(t) = n_o + \underbrace{\int_{-\infty}^{t} f(t', t)\, E^2(t')dt'}_{\delta n} \tag{32}$$

where n_o is the normal index, $E(t)$ is the laser electric field assumed to have a gaussian envelope ($E_o(t) = E_o e^{-t^2/T^2}$) and $f(t)$ is the weighing function describing

the response of the system; f(t) assumes the form $e^{-t/\tau}/\tau$ where τ is the response time of the material. The incident laser's electric field has the form given by Eq. 10. After propagating a distance into a material where dispersion has been neglected,[40] the electric field has the form given by Eq. 11.

For a material response time slower than pure electronic (models I and II) but faster than molecular orientation, i.e., coupled electronic, molecular redistribution, libratic motion ($t > \tau > 10/\omega_L$) - the envelope of the pulse is reflected in n(t):

$$n(t) = n_o + \frac{n_2 E_o^2}{2} e^{-2t^2/T^2} \tag{33}$$

f(t) has averaged out the optical cycles response. Substituting Eq. 33 into Eq. 11, the electric field in the time domain becomes

$$E(t) = E_o e^{-t^2/T^2} \cos\left(\omega_L t - \frac{n_o z \omega_L}{c} - \frac{1}{2}\frac{n_2 \omega_L z E_o^2 e^{-2t^2/T^2}}{c}\right). \tag{34}$$

For pure electronic response ($\tau \sim 1/\omega_L$, model III) for material $f(t) \to \delta(t)$ and

$$n(t) = n_o + n_2 E_o^2 e^{-2t^2/T^2} \cos^2(\omega_L t - n_o \omega_L z/c) \tag{35}$$

Substituting Eq. (35) into Eq. 11, the electric field in the time domain with higher odd harmonic ($3\omega_L$, $5\omega_L$ ...) absorpted is

$$E(t) = E_o e^{-t^2/T^2} \left\{ \cos\left(\omega_L t - \frac{n_o z \omega_L}{c} - \frac{n_2 \omega_L z E_o^2 e^{-2t^2/T^2}}{2c}\right) \right.$$

$$\times J_o\left(\frac{n_2 \omega_L z E_o^2 e^{-2t^2/T^2}}{2c}\right) - \sin\left(\omega_L t - \frac{n_o z \omega_L}{c} + \frac{n_2 \omega_L z E_o^2 e^{-2t^2/T^2}}{2c}\right)$$

$$\left. \times J_1\left(\frac{n_2 \omega_L z E_o^2 e^{-2t^2/T^2}}{2c}\right) \right\}. \tag{36}$$

$E(\omega)$ is obtained by the fourier transform Eq. 13 evaluated numerically.[41] The normalized spectral density of the phase modulated light is obtained from:

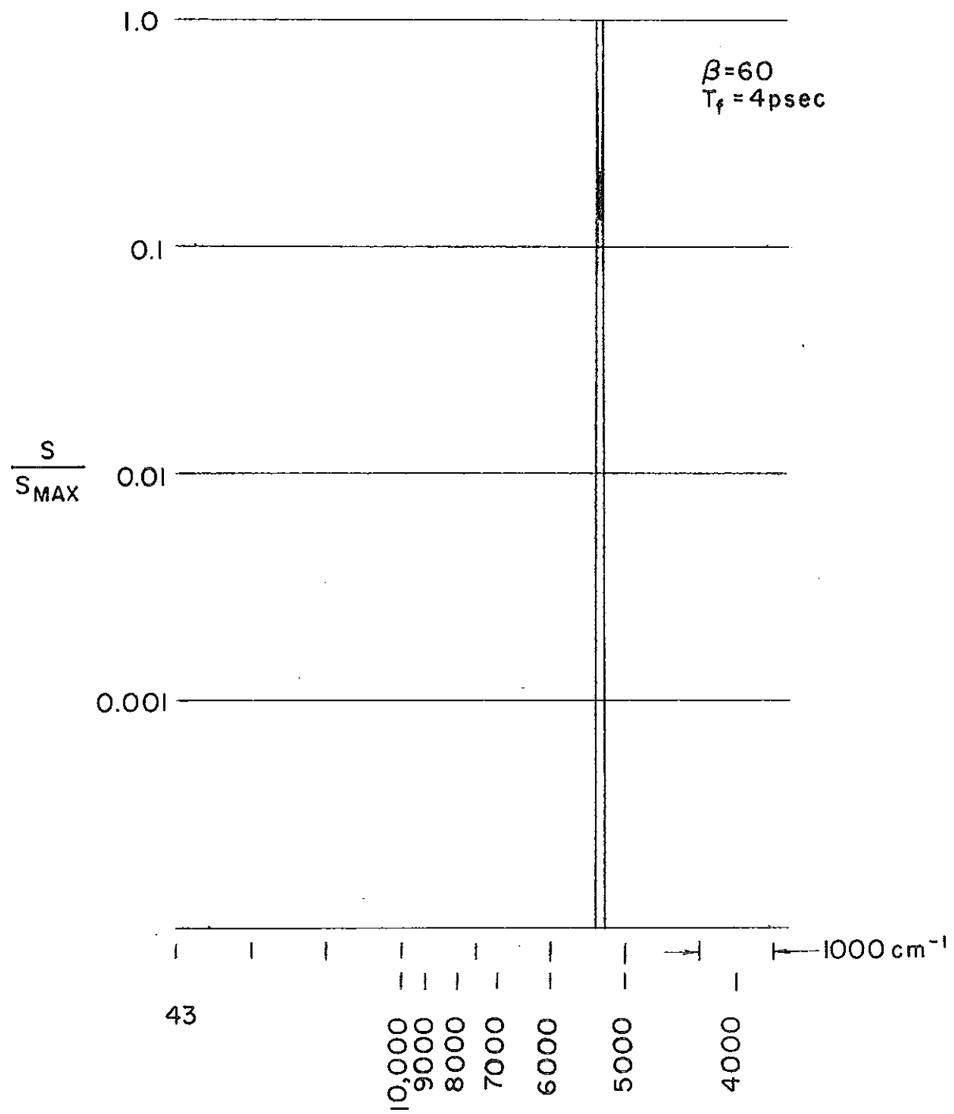

Fig. III-17. Calculated SPM spectrum for envelope model (I) for parameters $\beta = 60$, $T_f = 4$ psec.

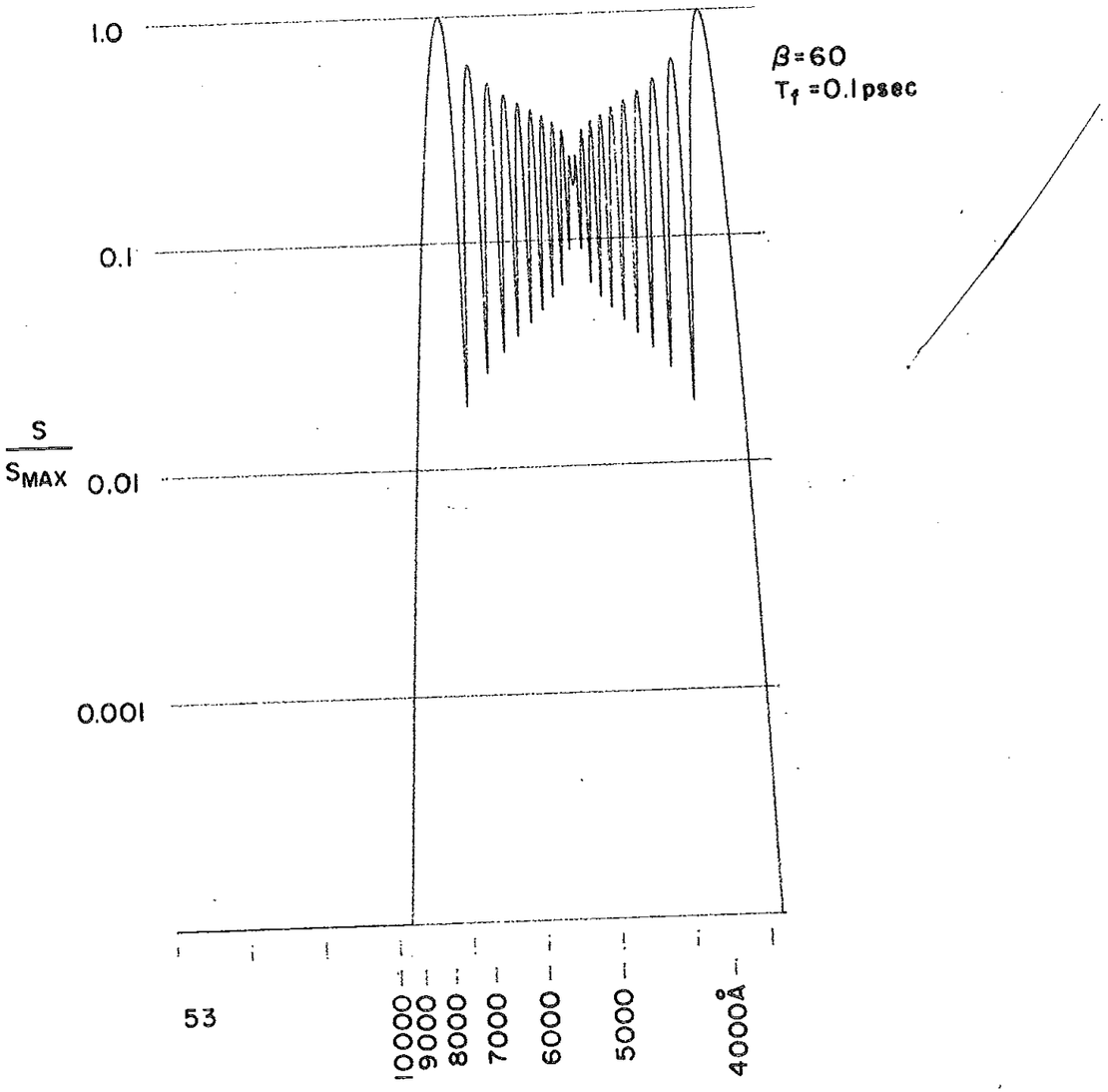

Fig. III-18. Calculated SPM spectrum for sub-picosecond model (II) for parameters: $\beta = 60$, $T_f = 0.1$ psec.

$$S(\omega) = \frac{c}{4\pi} |E/\omega|^2 / S_{max}(\omega) \tag{37}$$

The parameter β is defined as

$$\beta = \frac{1\, n_2\, E_o^2\, z\, \omega_L}{2c} \tag{38}$$

which measures the strength of the broadening process. From Eq. 31 the frequency broadening varies $\sim \beta/T_p$. A reasonable value for $\beta \cong 30$ can be chosen from knowing the approximate or typical value for the parameters used in these experiments: $n_2 \sim 1.2 \times 10^{-13}$ esu, $E_o \sim 3 \times 10^4$ esu (10^{11} w/cm^2), $n_2 E_o^2 \sim 1.2 \times 10^{-4}$ esu, $z \sim 5$ cm, and $\lambda_L = 5300$ Å. However, due to the uncertainty in electric field, E_o, and active propagation distance, z, resulting from self focusing, and the exact value for n_2 for all the materials studied, β may range from as high as 300 to as low as 1. ($n_2 E_o^2 \sim 10^{-3}$, $\omega_{L/C} \sim 10^5$ cm^{-1}, $z \sim 6$ cm).

The calculated SPM spectra for model I and II (E(t) is given by Eq. 34) are shown in figures III-17 through 20 for various β and T_f. The spectra in Fig. III-17 is for $\beta = 60$ and for a mechanism which follows the envelope of the pulse of 4 psec duration. The extent of the spectral broadening does not agree with experimental observation. A rather oversize $\beta \sim 1300$ is required to increase the broadening to the observed width. However, the SPM spectra shown in Fig. III-18, 19 and 20 calculated for model II for $\beta = 60$, 22, and 30 respectively have features which are similar to some of the experimental observation. For example, Fig. III-18 with $\beta = 60$ and $T_p = 0.1$ psec has (1) a large spectral extent ~ 7000 cm^{-1}, and (2) a large modulation frequency of the periodic structure in the spectrum which progressively increases away from the exciting frequency — initially its ~ 430 cm^{-1}, increases to 700 cm^{-1} and ends with 1400 cm^{-1}. Recall, from sections 2 and 3 that most of the SPM spectra either show no periodic structure, non-regular or random periodic structure with modulation frequency ranging from a few cm^{-1} to 1000 cm^{-1}, or periodic structure with modulation frequency which gets progressively, larger away from the exciting frequency. Also, all the experimental data have an intense central component at the exciting frequency which is ~ 100 - 1000 times larger than the SPM frequency components. The calculated spectrum for this model shows that the light is spread out into a continuum of frequencies with no intense central frequency and a smooth modulation.

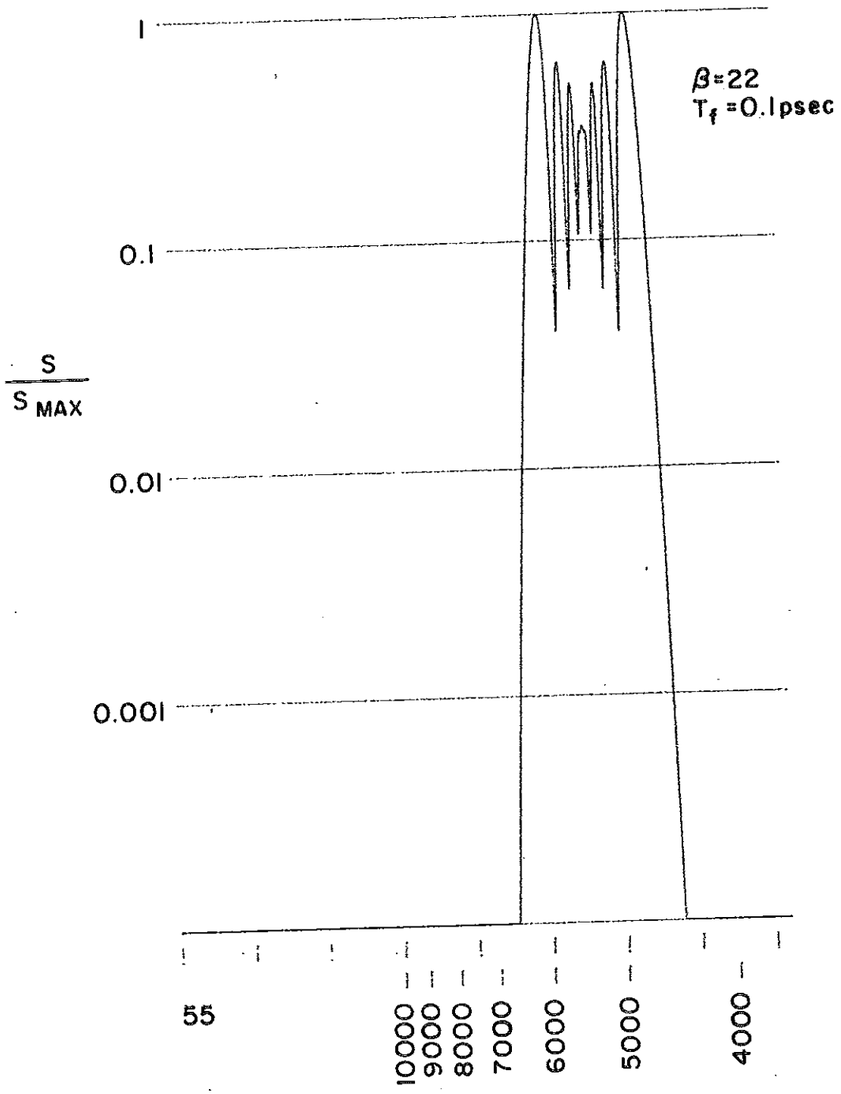

Fig. III-19. Calculated SPM spectrum for sub-picosecond model (II) for parameters: $\beta = 22$, $T_f = 0.1$ psec.

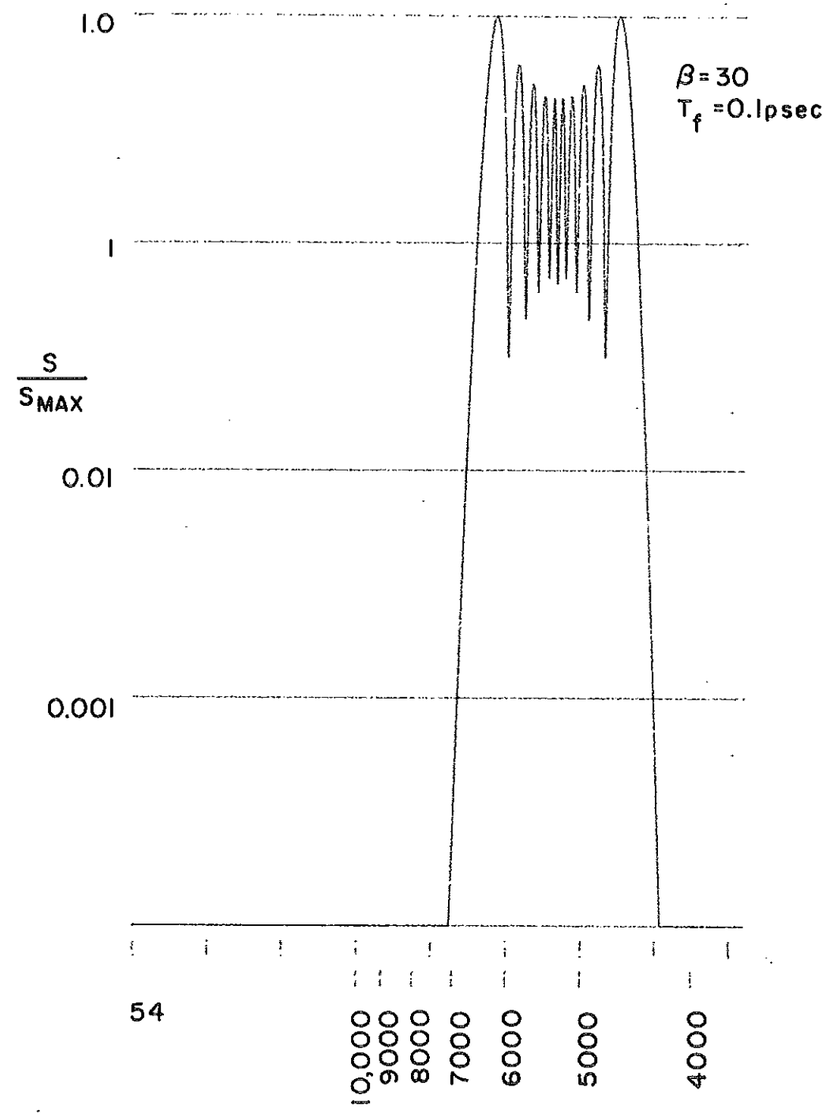

Fig. III-20. Calculated SPM spectrum for sub-picosecond model (II) for parameters: $\beta = 30$, $T_f = 0.1$ psec.

The differences between experimental and calculated spectrum may be explained by noting that the observed spectra is caused by the first few laser pulses (~ 10) in the whole train of pulses (~ 60) emitted by the mode-locked laser.[42] The first 10 pulses self-focused producing filaments which results in SRS and SPM emission. The intense central component may be due to non-filament light. Also part of light in the radial structure of each of the first ~ 10 pulses do not self-focus. The overlap of the spectra from different filament imaged on the spectrographic plate could occur, resulting in complicated modulated spectra with a non-regular pattern.

Calculated spectra for the electronic model III are shown in Fig. III-21 through Fig. III-30 for various β and T_f (E(t) is given by Eq. 36). In this model T_f is taken as the pulse width of either the envelope or one of the sub-picosecond pulse components. The spectra shown in Fig. III-21 with $T_f = 4$ psec and $\beta = 60$ and in Fig. III-22 with $T_f = 4/2$ psec and $\beta = 60$, again lack the wide broadening. Rather large spectral broadening is calculated for the sub-picosecond pulse with $T_f = 0.6$ and 0.1 psec. (Figs. III-23-29). Also, there is no regular periodic structure in the intensity profile in these latter figures (22-29) but just an interference behavior with intensity maximums and minimums in the spectrum. The frequency separation between the intensity maximum range from as small as few cm^{-1} to as high as ~ 1000 cm^{-1} depending on T_f and β. The frequency of the intensity maximum progressively increases away from the exciting laser's frequency. For example, in Fig. III-26 the intensity maximum in the SPM spectrum at first occurs every ~ 60 cm^{-1} and near the end every ~ 300 cm^{-1}.

Other features shown by these figures (23-29) are (1) an intense central component (5300 Å) which is ~ 100 times larger than the SPM background and, (2) the intensity SPM profile is approximately uniform with frequency. These characteristics are commonly observed experimentally and no hand waving arguments are necessary to account for gross differences between calculated and observed spectra. The electronic model (III) seems to fit the experimental data more consistently than models I and II.

As stated previously there are many mechanisms contributing to the nonlinear refractive index coefficient, n_2, for picosecond light pulses. Their magnitudes range from 10^{-11} to 10^{-14} esu and temporal responses range from $\sim 10^{-11}$ to 10^{-16} sec depending on the mechanism. The nonlinear refractive index for the material with different mechanisms takes the form:

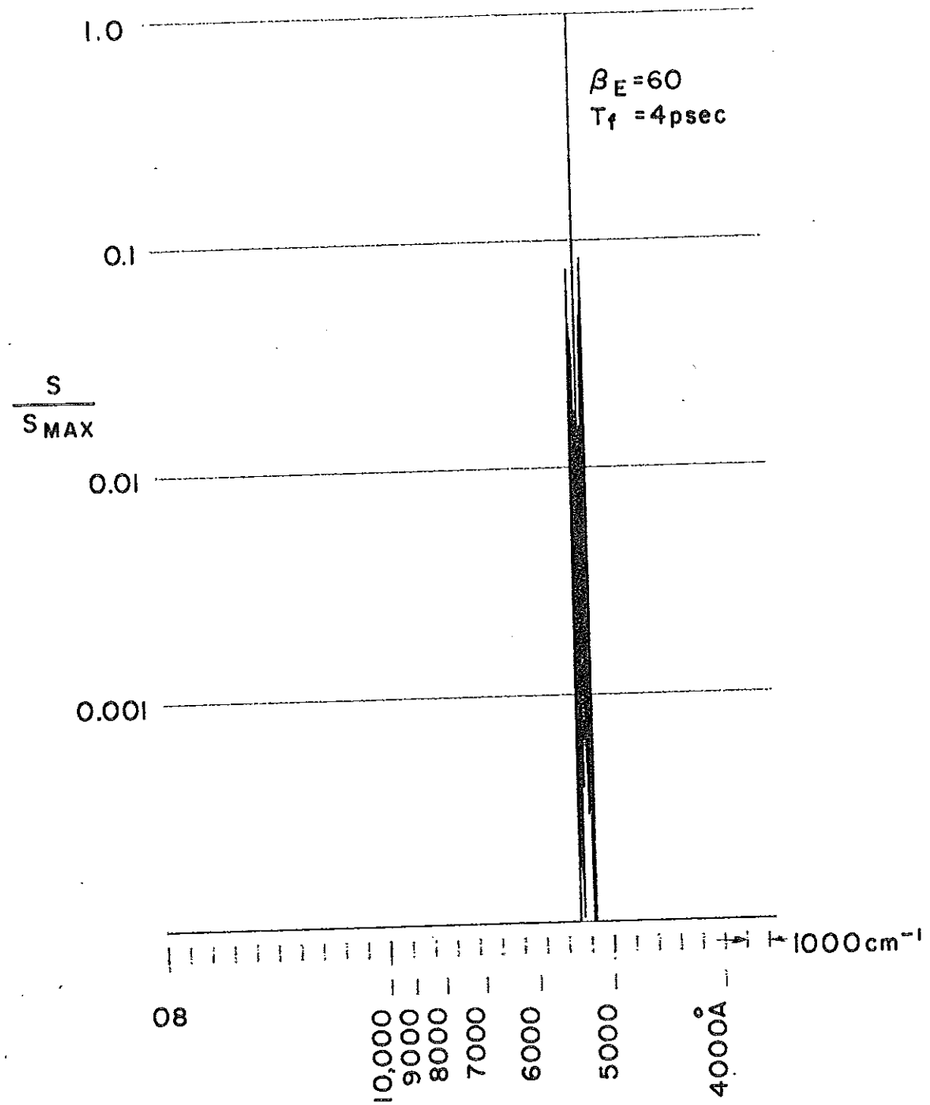

Fig. III-21. Calculated SPM for electronic model (III) for parameters: $\beta_E = 60$, $T_f = 4$ psec.

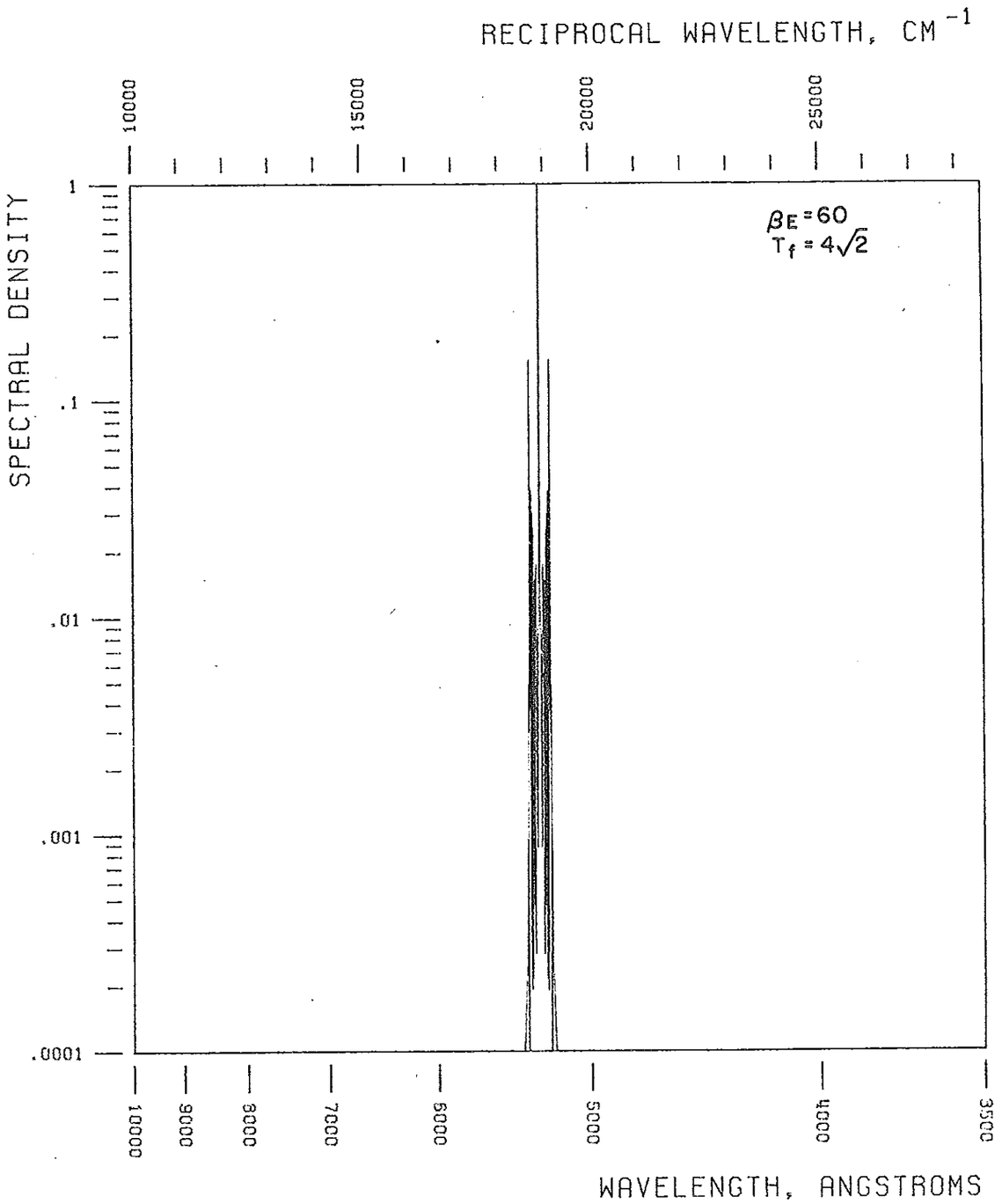

Fig. III-22. Calculated SPM for electronic model (III) for parameters: $\beta_E = 60$, $T_f = 4\sqrt{2}$ psec.

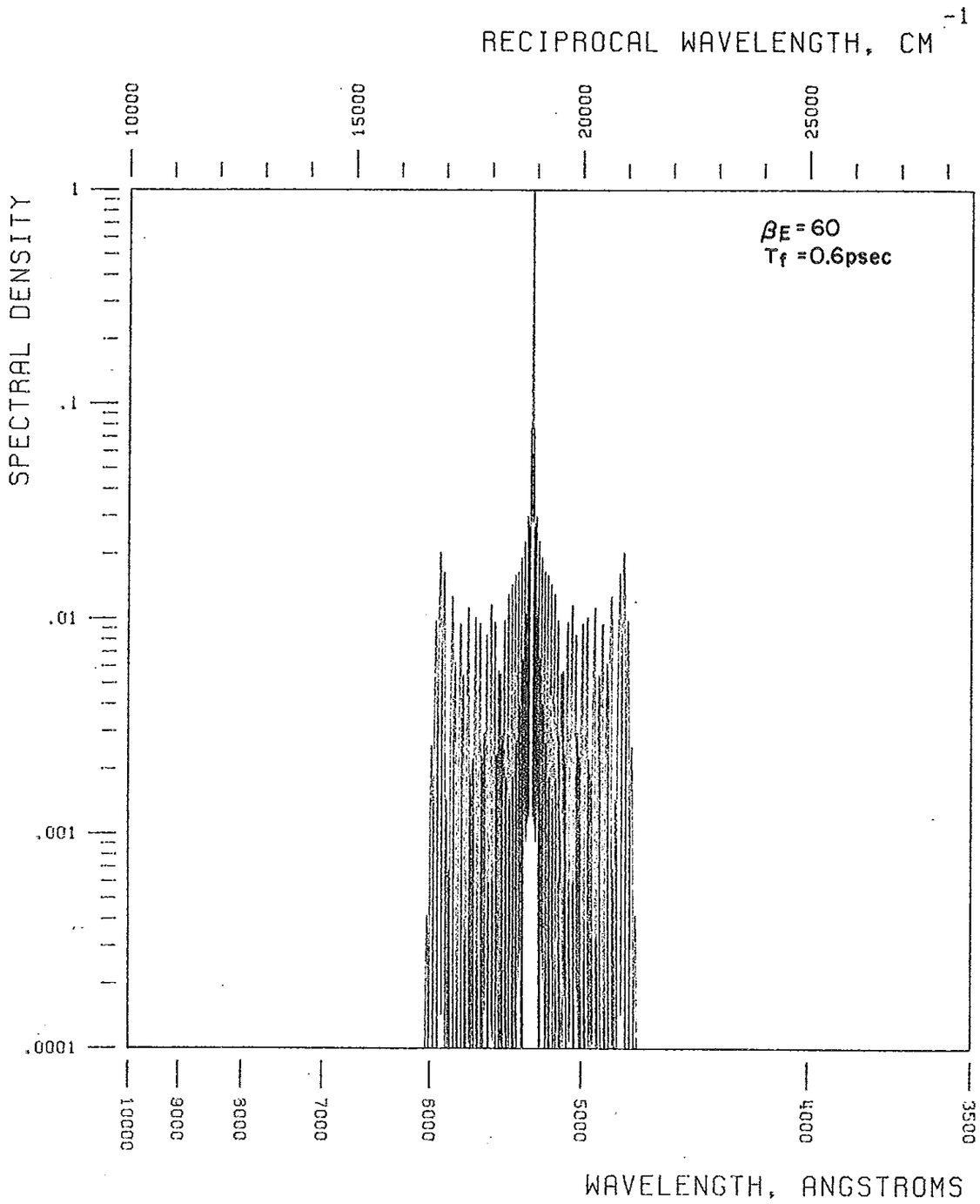

Fig. III-23. Calculated SPM for electronic model (III) for parameters: $\beta_E = 60$, $T_f = 0.6$ psec.

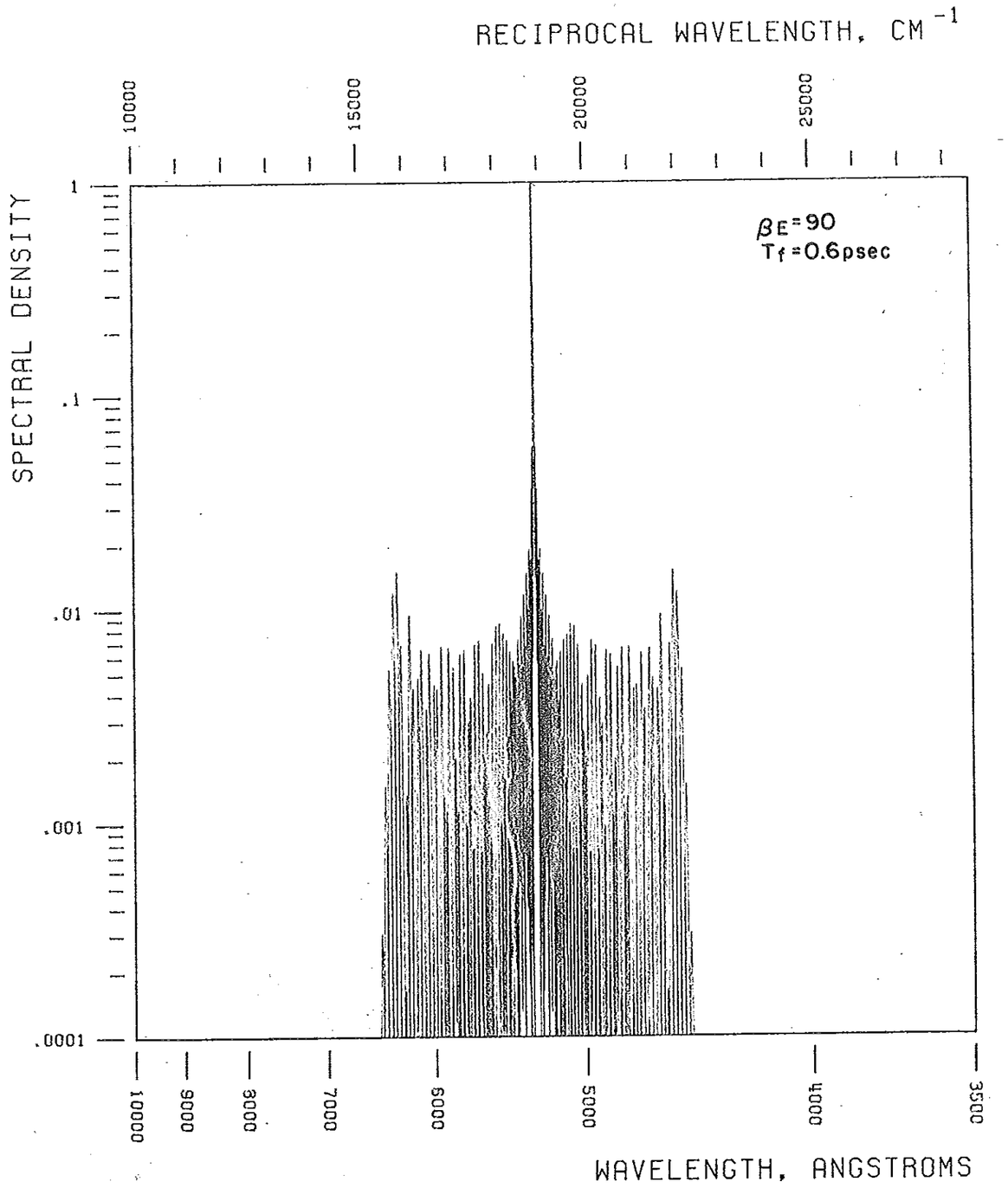

Fig. III-24. Calculated SPM for electronic model (III) for parameters: $\beta_E = 90$, $T_f = 0.6$ psec.

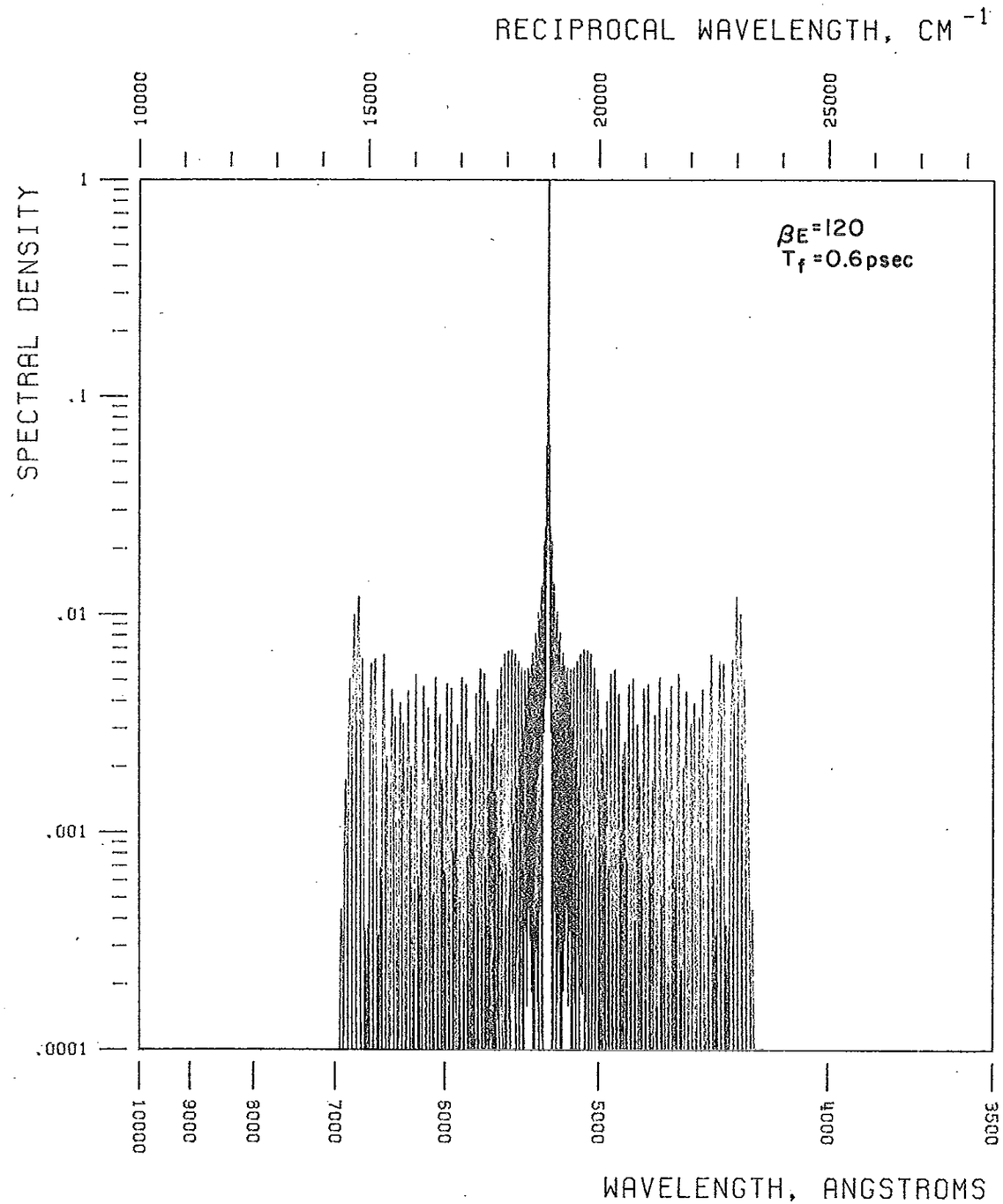

Fig. III-25. Calculated SPM for electronic model (III) for parameters: $\beta_E = 120$, $T_f = 0.6$ psec.

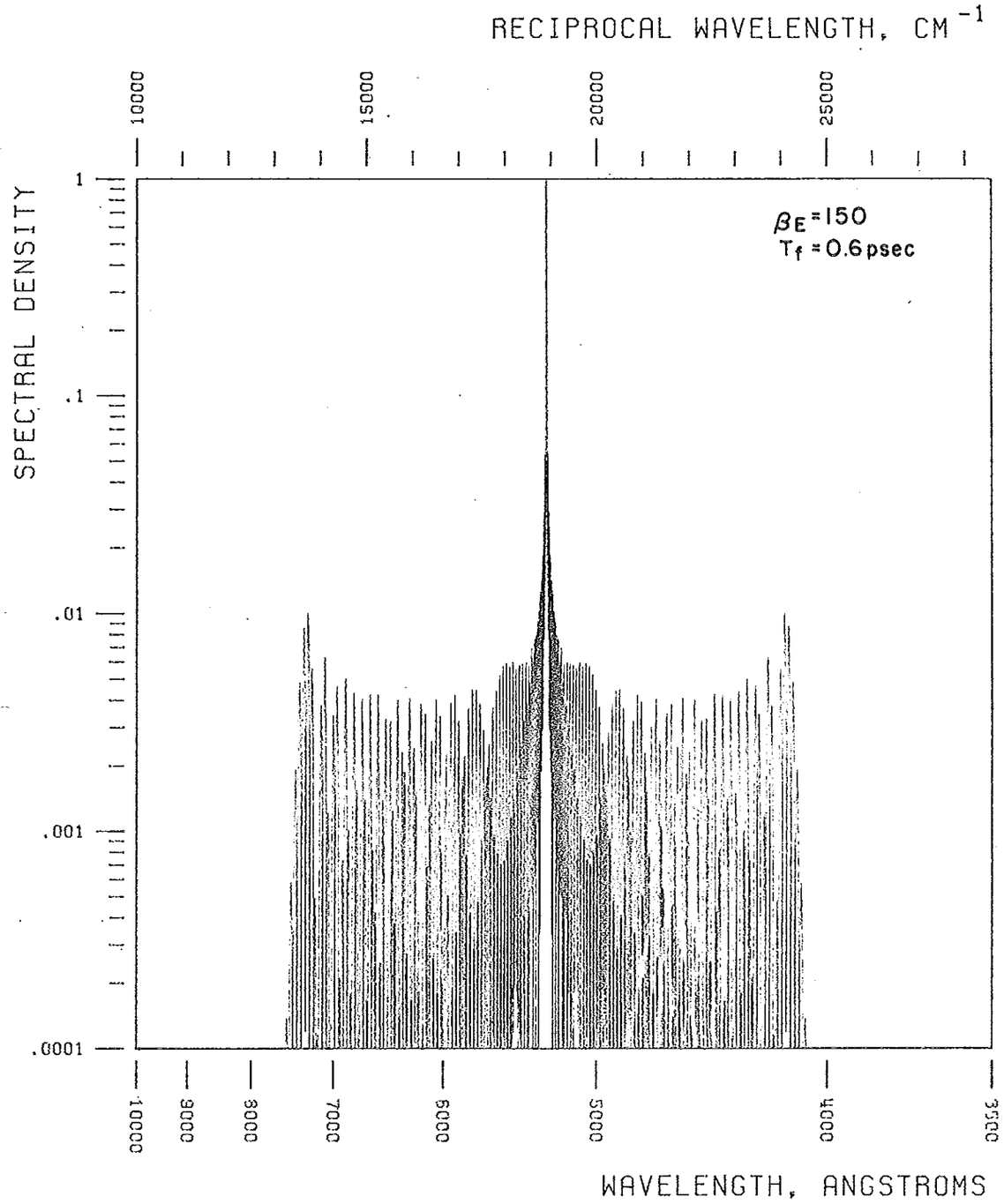

Fig. III-26. Calculated SPM for electronic model (III) for parameters: $\beta_E = 150$, $T_f = 0.6$ psec.

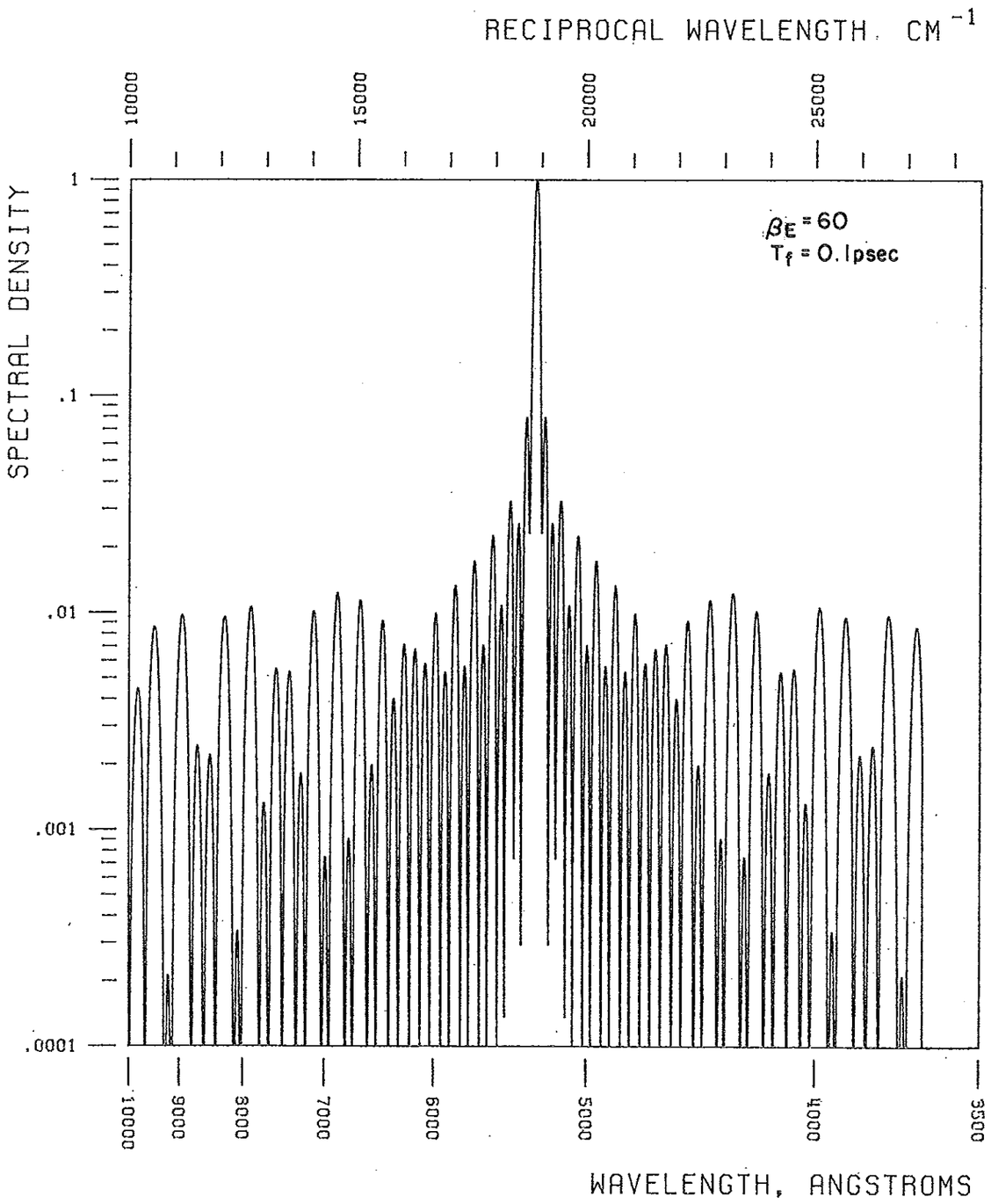

Fig. III-27. Calculated SPM for electronic model (III) for parameters: $\beta_E = 60$, $T_f = 0.1$ psec.

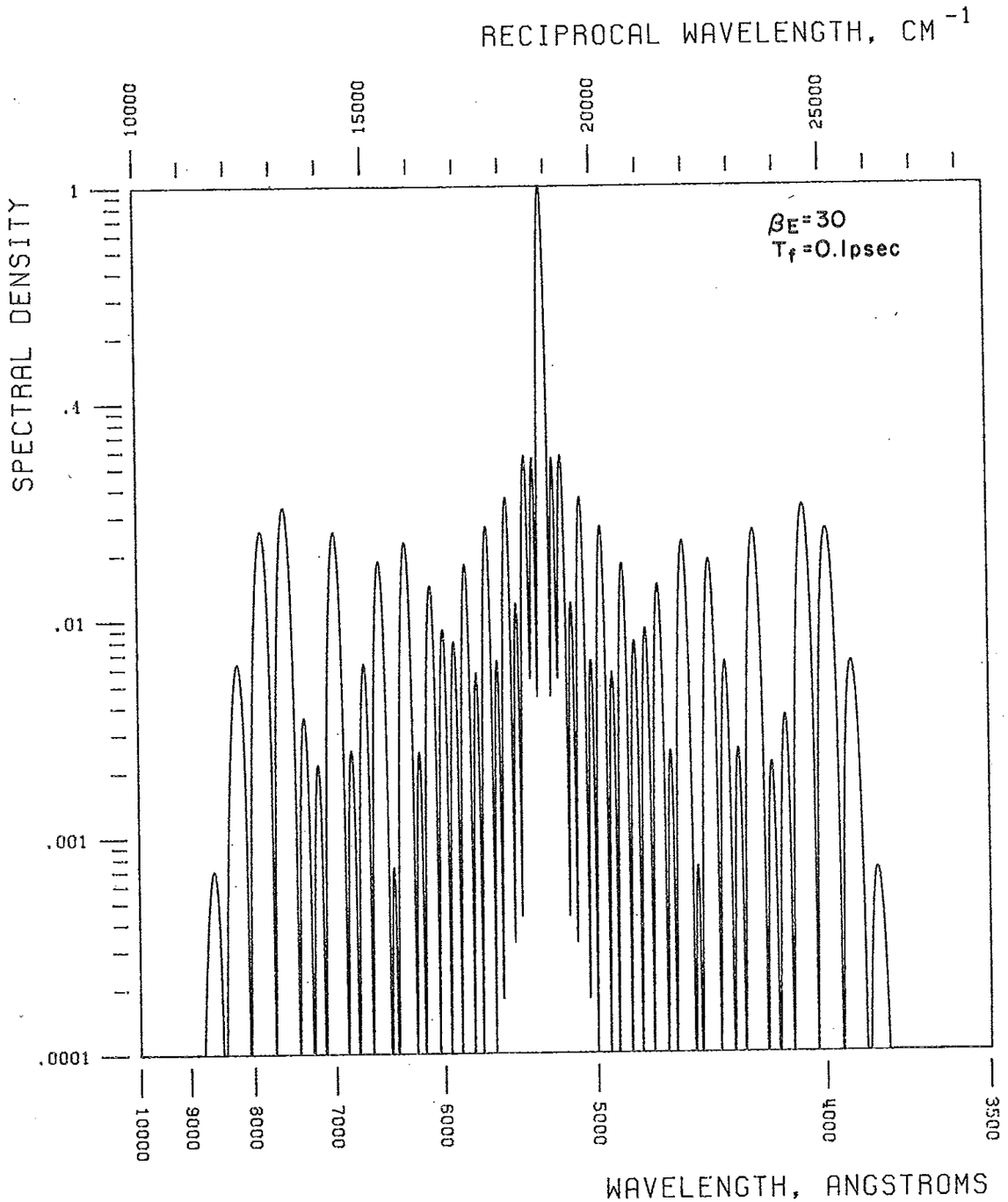

Fig. III-28. Calculated SPM for electronic model (III) for parameters: $\beta_E = 30$, $T_f = 0.1$ psec.

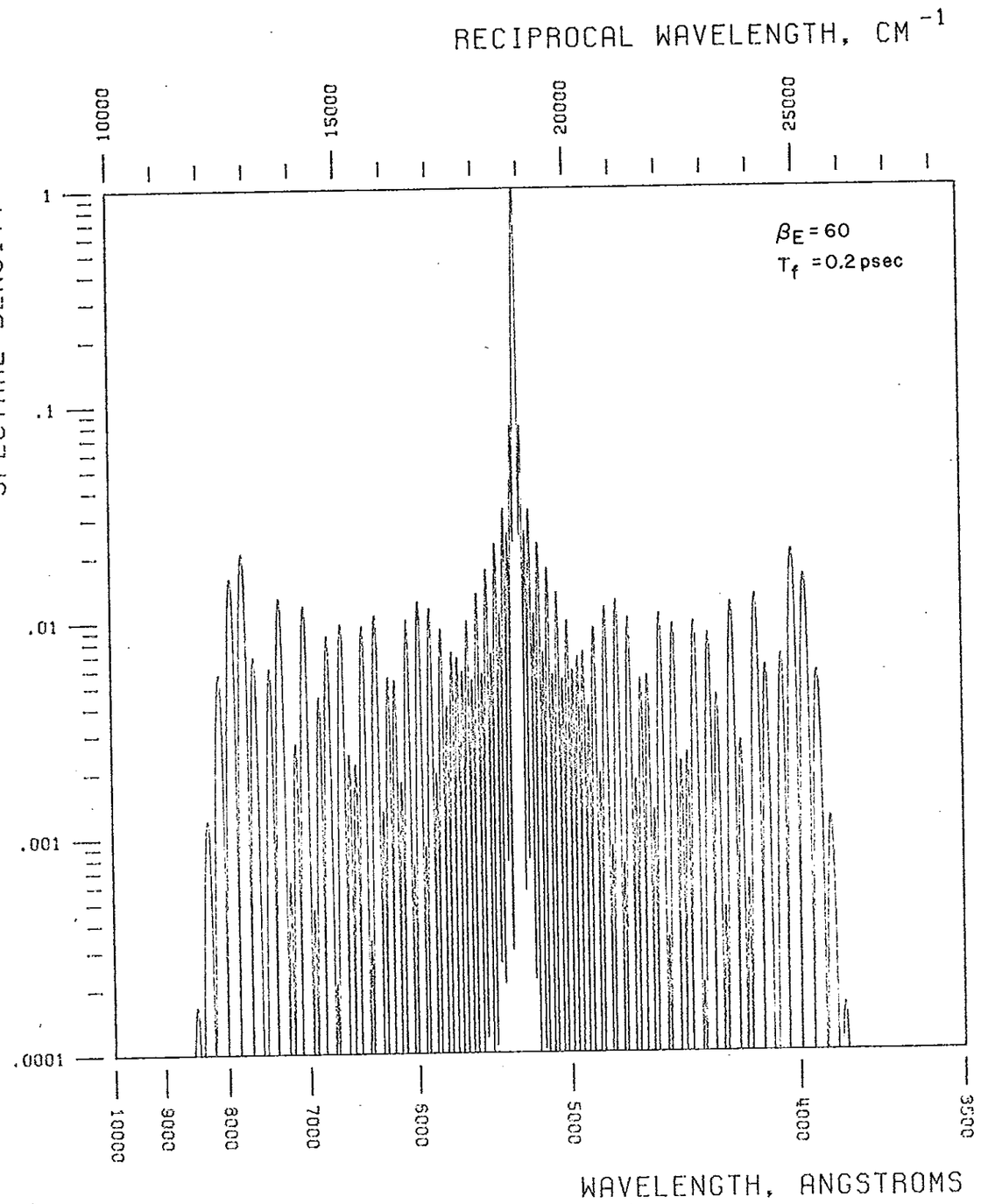

Fig. III-29. Calculated SPM for electronic model (III) for parameters: $\beta_E = 60$, $T_f = 0.2$ psec.

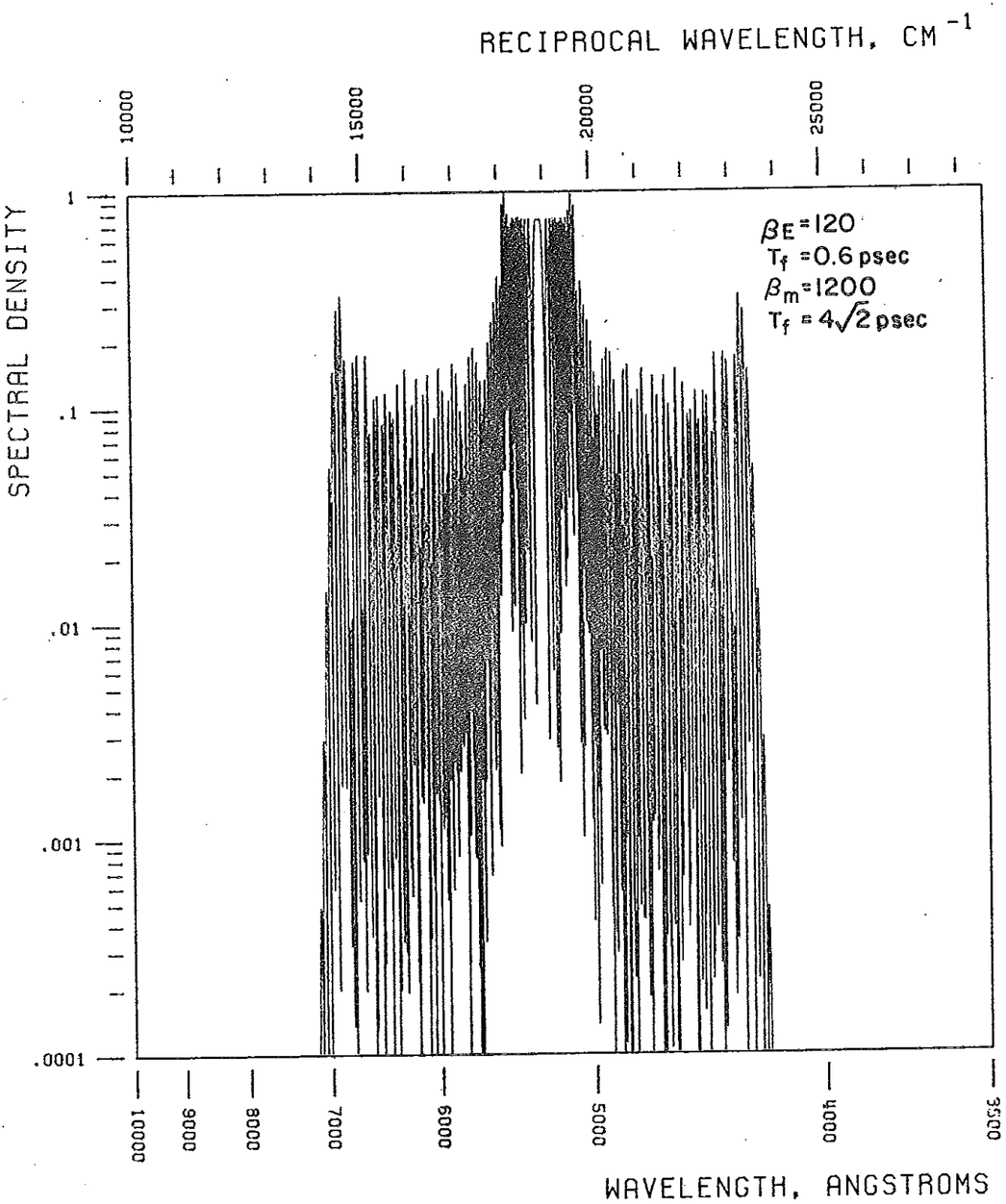

Fig. III-30. Calculated SPM for a combined electronic and molecular mechanism. The parameters are $\beta_E = 120$, $T_f = 0.6$ psec for an electronic model III and $\beta_M = 1200$, $T_f = 4\sqrt{2}$ psec for the molecular model (I).

$$\delta n(t) = \sum_j \delta n_j (E_o, T_p, \tau_j, t) \qquad (39)$$

where the index j defines the various mechanisms and τ_j their response time. The spectral amplitude for a gaussian plane wave in a material having many mechanisms operative is the convolution of the spectra for the separate processes i.e., for three mechanisms:

$$E(\omega) = \int_{-\infty}^{\infty} F_1(\omega_1)\, F_2(\omega_2 - \omega_1)\, F_3(\omega - \omega_2)\, d\omega_1 d\omega_2,$$

where $F_j(\omega)$ is the Fourier transform of $f_j(t)$ and $f_1(t) = E_o(t)\, e^{i\,\delta n_1 \omega_L z/c}$, $f_2(t) = e^{i\,\delta n_2 \omega_L z/c}$ and $f_3(t) = e^{i\,\delta n_3 \omega_L z/c}$. Since the spectral extent of the SPM process depends on β/τ^*, the electronic mechanism dominates the SPM process for the materials because of its ultrafast response $(\beta/\tau^*)_{\text{electronic}} > (\beta/\tau^*)_{\text{other mechanism}}$ Calculation of the SPM spectrum shown in Fig. III-30 for material having both an electronic and a slower molecular mechanism ($\tau^* \sim 10^{-13}$ sec) taking $n_{2\,\text{MOLECULAR}} = 10\ n_{2\,\text{ELECTRONIC}}$ shows that the electronic mechanism dominates giving rise to the wide extent $\sim 4000\ \text{cm}^{-1}$, while the slower mechanisms affects the interval structure of maxima and minima of the sweep near the central frequency within $\sim 500\ \text{cm}^{-1}$.

In conclusion the sub-picosecond model II does have some of the features observed in the spectra but the electronic model (III) with sub-picosecond pulses have most of the features observed in the spectra of the materials studied. Therefore, from arguments given in this section and in sections 1, 2 and 3, the electronic mechanism seems to be an important mechanism for SPM in the materials studied and in some materials it dominates.

5. Future Direction

Many problems on the dynamics of the SPM emission remains to be studied; the following possible experiments are directed to obtain this knowledge:

1. To possibly compress the SPM pulse to a pulse duration of $\sim 10^{-15}$ sec;

2. To find materials where the frequency broadening may extend into uv and possibly x-ray regions.

   The first four experiments require a single ultrashort pulse which has a clean radial structure (single transverse mode).

3. To measure the electronic contribution[43] of n_2 by using the Kerr effect as function of temperature with psec laser pulses.

III. REFERENCES

1. R. R. Alfano and S. L. Shapiro, Phys. Rev. Letters 24, 592 (1970).

2. R. R. Alfano and S. L. Shapiro, Phys. Rev. Letters 24, 1219 (1970).

3. F. Shimuzu, Phys. Rev. Letters 19, 1097 (1967).

4. P. Lallemand, Apply. Phys. Letters 8, 276 (1966); K. Shimoda, Jap. J. Appl. Phys. 5, 615 (1966); A. C. Cheung, D. M. Rank, R. Y. Chiao, C. H. Townes, Phys. Rev. Letters 20, 786 (1968); R. Polloni, C. A. Sacchi and O. Svelto, Phys. Rev. Letters 23, 690 (1969); Phys. Rev. A2, 1955 (1970).

5. E. B. Treacy, Phys Letts. 28A, 34 (1968).

6. Duguay, Private Communication, 1970.

7. R. Y. Chiao, E. Garmire, and C. H. Townes, Phys. Rev. Letters 13, 479 (1964).

8. A. L. Dyshko, V. V. Lugovoi, and A. M. Prokhorov, JETP Lett 6, 146 (1967); V. V. Lugovoi and A. M. Prokhorov, JETP Letters 7, 117 (1968).

9. T. K. Gustafson, J. P. Taran, H. A. Haus, J. R. Lifsitz and P. L. Kelley, Phys. Rev. 177, 306 (1969); F. DeMartini, C. H. Townes, T.K. Gustafson, P. L. Kelley, Phys. Rev. 164, 312 (1969).

   Self steepening is caused from the distortion of envelope of pulse. The tails and front edge of the pulse profile moves faster (c/n) than the peak because of the lower index of the wings. After traveling a distance in the material, the tail catches up with the peak resulting in a sharpened pulse profile. At the distance called the steepening distance, substantial spectral broadening occurs ~ 90 percent. The steepening distance is given by Gustafson[9] et al $Z_s = 0.194\ c\ \tau_e\ n_o/\delta n$ where τ_e is full 1/e width of the initial intensity profile. For $\delta n \sim 10^{-4}$, $n_o \sim 1.5$, $\tau_e \sim 4$ psec the steepening distance is of the order of 3.6 meters and if $\tau_e \sim 0.4$ p sec then Z_s = 36 cm. These distances are much greater than sample length and interaction length. Hence self phase modulation dominates the broadening process.

10. J. R. Lifsitz and H.P.H. Grieneisen, Appl. Phys. Letters 13, 245 (1968); A. C. Cheung, D. M. Rank, R. Y. Chiao, and C. H. Townes, Phys. Rev. Letters 20, 786 (1968); T. K. Gustafson, J. P. Taran, H. A. Haus, J.R. Lifsitz, and P. L. Kelley, Phys. Rev. 177, 306 (1969).

11. R. G. Brewer and C. H. Lee, Phys. Rev. Letters 21, 267 (1968).

12. Y. R. Shen, Phys. Letters 20, 378 (1966); Y. R. Shen and Y. L. Shaham, Phys. Rev. 163, 224 (1967); S. L. Shapiro, J. A. Giordmaine, and K. W. Wecht, Phys. Rev. Letters 19, 1093 (1967).

13. R. W. Hellwarth, J. Chem. Phys. 52, 2128 (1970); R. W. Hellwarth and N. George, Opto-Electron 1, 213 (1970); R. W. Hellwarth, Quantum Optics edited R. J. Glauber, Academic Press 1969, New York p. 563.

14. A calculated estimate of n_2 for molecular redistribution for liquid argon can be made from the Kerr constant calculated by J. A. Brace and J. V. Champion, J. Phys. C. Solid State 2, 2408 (1969) of $B_K = 4 \times 10^{-9}$ esu at $\lambda = 0.6\ \mu$ giving a $n_{2_{MR}} = (2/3)B_K\lambda = 1.6 \times 10^{13}$ esu. From the equation for n_2 given in reference 4 for rocking mechanism, a calculated estimate for n_2 for interrupted rocking can be made to give $n_{2_{ROCKING}} = 0.9 \times 10^{-14}$ esu (for calculation see reference 15a). This value for n_2 is a factor of ten less than molecular redistribution mechanism.

Hellwarth (Ref 13) has shown that n_2 due to all other mechanisms except electronic is proportional to the intensity of the depolarized light scattering wing in liquids ($I \propto n_2$). The depolarized light scattering in liquid argon was measured by J. P. McTague, P. A. Fleury, and D. B. DuPre (Phys. Rev. 188, 303 (1969)) and yields an estimate of n_2 of 1.1×10^{-14} esu (For calculation see ref. 15b) In rare gases n_2 is composed of two parts — electronic and molecular redistribution (A. D. Buckingham and D. A. Dunmur, Trans. Faraday Soc. 64, 1776 (1968)), and possibly interrupted rocking. At low pressures molecular redistribution does not contribute to n_2. The electronic part of n_2 increases linearly with density while the molecular redistribution part increases as the density squared. As the gas pressure increases, the molecular redistribution part becomes proportionately greater because of the density-squared dependence. When Buckingham and Dunmur's data for gases is extrapolated to liquid densities then n_2 due to molecular redistribution would be estimated to be 2×10^{-13} esu in liquid argon (For calculation see reference 15c). However, at liquid densities the intensity of the depolarized scattering is an order of magnitude smaller than expected on the basis of a density-squared dependence (McTague, Fleury, and DuPre). As pointed out by McTague, Fleury, and DuPre, "the major cause of the relative decrease in intensity in the liquid is probably the contribution of 3-, 4-, etc. particle correlations, which tend to make the local liquid environment more symmetrical, leading to a lower anisotropy of the polarizability." This gives a calculated $n_2 \sim 2 \times 10^{-14}$ esu for all mechanism of non-electronic origin.

15a. From Ref. 4, $n_2 = 4\pi L^4 N(a_{\parallel} - a_{\perp})^2/15 n_o \mu$ esu where N is number density $L^4/n_o = (n_o^2+2)^4/81\ n_o$ is local field correction, n_o is index of refraction, $a_{\parallel} - a_{\perp}$ is polarizability anisotropy, $\mu \sim 8\ \pi a^3 G$, G is shear modulus, and a is molecular radius. For liquid argon $N = 2.1 \times 10^{22}/cm^3$, $L^4/n_o = 1.53$, $n_o = 1.23$, $G = 1.25 \times 10^{10}$ dynes/cm^2, $a = 2 \times 10^{-8}$ cm, $N_A = 6.02 \times 10^{23}$/mole, $\rho = 78 \times 10^{-3}$ moles/cm^3; calculated value for $\mu = 2.5 \times 10^{-12}$ dynes/cm, and $a_{\parallel} - a_{\perp}$ is calculated from Buckingham and Dunmur's[14] $B_K = 5.6 \times 10^{-12}$ esu to be $a_{\parallel} - a_{\perp} = 5.5 \times 10^{-25}$ esu. (Note $a_{\parallel} - a_{\perp} = \sqrt{B_K \rho 405\, KT/4\pi N_A}$.) Using these values $n_{2\,(rocking)} = 0.9 \times 10^{-14}$ esu.

15b. The non-electronic contribution to n_2 for argon is estimated from inelastic scattering data. McTague and Fleury[14] found that the total integrated intensity of the Rayleigh wing for argon is times 2 times that of the 459 cm^{-1} Raman line in CCl_4:

$$I_{WING\ ARGON} = 2\, I_{459\ cm^{-1}\ CCl_4} = 2\,(I_{459\ cm^{-1}\ STOKES} + I_{459\ cm^{-1}\ ANTISTOKES})$$

since

$$I_{459\ STOKES} = 0.22\, I_{459\ ANTISTOKES} \quad \text{in } CCl_4$$

then

$$I_{WING\ ARGON} = 2.44\, I_{459\ CCl_4\ STOKES}$$

Substituting the following relationships into the latter equation: the cross section $\sigma_{RAMAN} = 3.5 \times 10^{-3}\, \sigma_{BRILLOUIN}$ in CCl_4 -

and

$$I_{BRILLOUIN\ CS_2} = 4 I_{BRILLOUIN\ CCl_4}$$

and

$$I_{WING\ CS_2} = 3.57\, I_{BRILLOUIN\ CS_2}$$

obtained from S. L. Shapiro, Ph. D. Thesis, University of California, 1967 unpublished. The total integrated intensity for the wing in argon becomes

$$I_{WING\ ARGON} = 6 \times 10^{-4}\, I_{WING\ CS_2}$$

Therefore, the non-electronic contribution to n_2 is estimated to be $n_{2\,ARGON} = 6 \times 10^{-4}\, n_{2\,CS_2} = 1.1 \times 10^{-14}$ esu.

15c. From Buckingham and Dunmur[14] $n_2 = \beta\,(A_K\rho + B_K\rho^2)$ where A_K is electron contribution and B_K is the molecular redistribution coefficients. The ratio of $B_K\rho^2/A_K\rho = 0.26$ at a gas density $\rho = 3 \times 10^{-3}$ moles/cm^3 is obtained from Fig. 1.[14] Therefore $B_K/A_K = .089 \times 10^3$ at $\rho = 3 \times 10^{-3}$ moles/cm^3. At liquid density, $\rho = 35 \times 10^{-3}$ moles/cm^3, $.089\, A_K\rho^2/A_K\rho = 3.15$ and $n_{2\,MR} = (3.15)\, n_{2\,EL} = 1.9 \times 10^{-13}$ esu $\sim 2 \times 10^{-13}$ esu.

16. J. McTague, P. Fleury, and D. DuPre, Phys. Rev. 188, 303 (1969).

17. W. S. Gornall, H. E. Howard-Lock, and B. P. Stoicheff, Phys. Rev. (to be published).

18. M. M. Denariez-Roberge and J. P. E. Taran, Appl. Phys. Letters 14, 205 (1969).

19. R. A. Fisher, P. L. Kelley, and T. K. Gustafson, Appl. Phys. Letters 14, 140 (1969).

20. C. Wang, Phys. Rev. 152, 149 (1966); .B Sept. 1970; M. A. Duguay, Private communication; and R. R. Alfano, measured using gate technique similar to M. A. Duguay and J. W. Hansen, Appl. Phys. Letters 15, 192 (1969); M. A. Duguay and J. Hansen, NBS 341, 45 (1970), Boulder, Colorado.

21. A. Javan and P. L. Kelley, IEEE J. Quantum Electron. 2, 470 (1966).

22. R. Y. Chiao, P. L. Kelley, and E. Garmine, Phys. Rev. Letters 17, 1158 (1966).

23. Pulses broaden from 20 to 80 cm^{-1} in the pulse train of the Nd-glass oscillator; M. A. Duguay, private communication.

24. L. H. Bolz, H. P. Broida, and H. S. Peiser, Acta Cryst. 158, 810 (1962).

25. W. H. Glenn and M. J. Brienza, Appl. Phys. Letters 10, 221 (1967).

26. J. H. Marburger and E. Dawes, Phys. Rev. Letters 21, 556 (1968); E. L. Dawes and J. H. Marburger, Phys. Rev. 179, 862 (1969).

27. A. D. Buckingham and J. A. Pople, Proc. Phys. Soc. (London) 905 (1955); A. D. Buckingham and B. J. Orr, Quart. Rev. (London) 21, 195 (1967); A. D. Buckingham, Proc. Phys. Soc. (London) B69, 344 (1955); L. L. Boyle, A. D. Buckingham, R. L. Disch, and D. A. Dunmur, J. Chem. Phys. 45, 1318 (1966).

28. G. A. Askar'yan, Zh. Eksperim. i Teor. Fiz.—Pis'ma Redakt. 6, 672 (1967) [JETP Letters 6, 157 (1967)]. In notation of Ref. 28 the change in polarizability $\Delta\alpha = dP/dE_L = \gamma E_L^2/2$.

29. P. W. Langhoff, J. D. Lyons, and R. P. Hurst, Phys. Rev. 148, 18 (1966).

30. A. D. Buckingham and D. A. Dunmur, Trans. Faraday Soc. 64, 1776 (1968).

31. The equation for n_2 is calculated from the equations $\delta n_{\parallel} = n_2\langle E^2\rangle$, $\delta n_{\parallel} = 3\delta n_{\perp}$ for electronic mechanism, and $\delta n_{\parallel} - \delta n_{\perp} = (n_o^2+2)^4 2\pi N\gamma\langle E^2\rangle/243\, n_o$ (See Refs. 13 and 30). In the notation of Ref. 30, $n_{xx} = n_o + \delta n_{\parallel}$ and $n_{yy} = n_o + \delta n_{\perp}$.

32. A. C. Sinnock and B. L. Smith, Phys. Rev. 181, 1297 (1969).

33. When a powerful laser pulse propagates through an isotropic dielectric, it charges the refractive index which has been defined by the equations:

$$\delta n_{\parallel} = n_2 \langle E^2 \rangle$$

$$\delta n_{\parallel} - \delta n_{\perp} = n_{2B} \langle E^2 \rangle$$

where $\langle E^2 \rangle$ is mean square of the optical field $\vec{E}$, $\delta n_{\parallel}$ ($\delta n_{\perp}$) is the change in the refractive index ($\delta n_{\parallel} = n_{\parallel} - n_o$, $\delta n_{\perp} = n_{\perp} - n_o$) seen by light polarized parallel (normal) to electric field, n_o is the normal index, and n_{2B} is defined as the nonlinear birefringence index ($n_{2B} = B_K \lambda$, where B_K is the Kerr constant and λ the measuring wavelength). For an electron cloud distortion for spherical atoms Buckingham and Dunmur[30] has shown that $\delta n_{\parallel} = 3\, \delta n_{\perp}$ giving a relationship between n_2, n_{2B} and B_K: $n_2 = \frac{3}{2} n_{2B} = 3 B_K \lambda / 2$ For molecular redistribution Hellwarth[13] has shown that $\delta n_{\parallel} = -2 \delta n_{\perp}$ giving $n_2 = \frac{2}{3} n_{2B} = \frac{2}{3} B_K \lambda$. Therefore for electronic mechanisms for argon:

$$\delta n_{\parallel} - \delta n_{\perp} = n_{2B} \langle E^2 \rangle = \left(\frac{2}{3} n_2 \right) \frac{E_o^2}{2} = \frac{1}{3} n_2 E_o^2 .$$

34. P. L. Kelley, Phys. Rev. Letters 15, 1005 (1965).

35. S. L. Shapiro and M. A. Duguay, Phys. Letters 28A , 698 (1969).
The TPF pattern of a pulse emitted from Nd: glass laser Q-switched with a saturable dye absorber cannot determine the shape of this pulse. It gives the total duration of the pulse which is ~6 psec, and within this 6 psec envelope there are short sub-picosecond pulses ~ 0.1 to 1 psec.

36. A. Erelyi, "Asymptotic Expansions," Dover (1956) pp. 51-53. The technique of stationary phase was learned in Dr. Sirlin's course.

37. The maximum frequency extent is

$$\Delta\omega_{MAX} = \frac{-\omega_L z}{c} \frac{\partial}{\partial t} (\delta n) \Big|_{t'} .$$

Assuming an envelope model $E(t)^2 = \frac{1}{2} E_o^2 e^{-2t^2/T^2}$ and $\delta n = \frac{n_2 E_o^2}{2} e^{-2t^2/T^2}$. The FWHM $T_p = (2 \ln 2)^{1/2} T$ is obtained by setting $e^{-2t^2/T^2} = 1/2$ and $t' = T/2$ is obtained by setting $\frac{\partial^2}{\partial t^2} \delta n = 0$. Substituting these parameters into $\Delta\omega_{MAX}$:

$$\Delta\omega_{MAX} = 0.715 \frac{\omega_L z n_2}{c T_p} E_o^2 \ \text{sec}^{-1},$$

and the frequency extent in wavenumbers

$$\Delta\bar{\nu}_{MAX} = \frac{0.715}{2\pi c} \frac{\omega_L z n_2 E_o^2}{c T_p} \text{ cm}^{-1},$$

or

$$\Delta\bar{\nu} \sim \delta\bar{\nu} \frac{\omega_L z n_2 E_o^2}{c} \text{ cm}^{-1},$$

where $\delta\bar{\nu}$ is bandwidth of laser in cm^{-1}.

38. For calculation purposes only one sub-picosecond pulses of the total burst of radiation is assumed to generate the SPM spectrum. T_p is taken as the pulse width of this spike. This model is oversimplified but gives the general features of the spectrum without a more detailed complex computer evaluation. The SPM spectrum for random array of sub-picosecond pulses within the envelope of the total burst of radiation will approximately be a superposition spectra with similar extent and non-regular modulation as a single pulse. The internal spectral structure (as distinct from the spectral extent) varies from shot to shot. One reason for this is probably the presence of more than one input pulse or subpicosecond pulse components. If the Fourier transform of each subcomponent pulse h(t) is $h(\omega)$, and if the picosecond components of a picosecond pulse are written in the form

$$E(t) = \sum_n a_n h(t - t_n) .$$

Then

$$E(\omega) = h(\omega) \sum_n a_n e^{i\omega t_n} .$$

The internal structure is complicated by the second factor in this last expression.

39. The interaction length for the SPM process in for example BK-7 glass is ≥ 2 mm for the spectral components within the Antistokes 4000 cm^{-1} frequency sweep for the 5300 Å sub-picosecond pulse of 0.3 ps duration. The interaction length $\ell = T_p \bar{V}_g^2 / 2\Delta V_g$ for two pulses is defined to be a distance for which two pulses stay spatially coincident by less than a half-pulse width; $\bar{V}_g$ is average group velocity, and ΔV_g is difference in group velocities. The derivation of this expression is given in Section V. The group velocity is given by

$$V_g = \frac{c}{n} + \frac{\lambda c}{n^2} \frac{\partial n}{\partial \lambda} \text{ and } V_{5300\text{ Å}} = 1.9358 \times 10^{10} \text{ cm/sec}$$

and $V_{4373\text{ Å}} = 1.9090 \times 10^{10}$ cm/sec.

40. The SPM pulse has been shown to be an ideal tool to do picosecond spectroscopy (R. R. Alfano and S. L. Shapiro, Chem. Phys. Letters 8, 631 (1970)). A SPM pulse after propagating a distance z into a material becomes broadened due to dispersion thereby washing out the subpicosecond pulse array —the red frequency components move to the leading edge and the blue to the trailing edge of the picosecond envelope, i.e., a SPM pulse of duration 0.3 psec with a total spectral extent of 8000 cm^{-1} about 5300 Å will broaden to ~ 6 psec after propagating through 4 cm of BK-7 glass.

41. The computer evaluation of the integral $E(\omega)$ and $|E(\omega)|^2$ was made by L. L. Hope of GTE Laboratories.

42. R. L. Carman, M. E. Mack, F. Shimizu, and N. Bloembergen, Phys. Rev. Letters 23, 1327 (1969); M. J. Colles, Optics Commun. 1, 169 (1969); R. R. Alfano and S. L. Shapiro, Phys. Rev. A2, 2376 (1970). Only the leading pulses in a long picosecond pulse train were effective in SRS. It was shown by R. R. Alfano and S. L. Shapiro that absorption present in pure liquid is sufficient to cause self-defocusing due to thermal heating to shorten the SRS train.

43. R. Hellwarth, A. Owyoung, and N. George, Phys. Rev A 1971 to be published.

They deduced from Kerr measurements using 20 nsec laser pulse that the dominate mechanism for the nonlinear refractive index, n_2, is of electronic origin in liquid CCl_4.

IV - FOUR-PHOTON PARAMETRIC GENERATION IN GLASS

1. Introduction

The generation of light over the visible region in an angular pattern is another striking nonlinear optical effect observed when intense 5300 Å picosecond laser pulses are passed through materials. The light at different wavelengths are emitted from the materials at different angles. This chapter reports on the experimental observation and on a theoretical analysis of the angular emission from glass.[1] This angular emission is shown to result from the coupling of four photons via the nonlinear coefficient $n_2(\chi^3)$.

Chiao, Kelley, and Garmire[2] have shown theoretically that when weak Stokes and anti-Stokes waves accompany a strong laser wave, both Stokes and anti-Stokes waves are amplified via χ^3. This process has been called four-photon parametric amplification or light by light scattering.[2] Degenerate four-photon interaction ($\omega_1 = \omega_2 = \omega_3 = \omega_4$) in liquids was first described by Chiao, Kelley, and Garmire[2] and observed by Carman, Chiao, and Kelley[3] in nitrobenzene.

We have observed nondegenerate four-photon stimulated emission ($\omega_1 \neq \omega_2 \neq \omega_3 \neq \omega_4$) in many materials originating from scale filaments created under high power 5300 Å picosecond-pulse excitation. The four-photon coupling process originates through the distortion of the atomic configuration inside the filaments in the materials, Positive and negative SPM frequency components are generated inside the filaments.[4] The frequency-swept photons and laser photons are coupled to the laser field via the third-order susceptibility χ^3 or the intensity-dependent dielectric refractive index coefficient n_2. The four-photon process is of the type $\vec{K}_L + \vec{K}_L = \vec{K}_A + \vec{K}_S$ schematically depicted in Fig. IV-1 where $\vec{K}_L$, $\vec{K}_S$, $\vec{K}_A$ are the wave vectors of the laser beam, Stokes-shifted photons, and anti-Stokes-shifted photons, respectively. The maximum amplification of the weak waves occur along an angular direction governed by phase matching among the four photons.

This process is quite general and we have observed this process in glasses, calcite, and liquids such as CCl_4 and acetone. Borosilicate glass BK-7 is chosen for specific analysis because accurate values of the refractive index are available and because there are no sharp vibrational Raman lines which would interfere with the interpretation of a four-photon nondegenerate process. Amplification

Four-photon coupling in solids

2 laser, 1 antistoke swept photon, 1 stokes swept photon are coupled in a solid and emerge with an angular distribution given by the wave vector diagram:

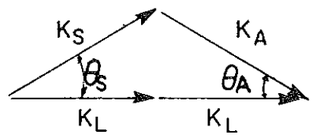

$$\overline{K}_L + \overline{K}_L = \overline{K}_S + \overline{K}_A$$

Fig. IV-1. Four-photon coupling showing volume phase matching among two-laser, anti-Stokes, and Stokes photon.

of Stokes and anti-Stokes waves found in this investigation is different from the Raman process.[5,6] This process cannot be a two-step Raman process requiring coherent optical phonons as an intermediate step because there are no sharp molecular vibrations in borosilicate BK-7 glass, and because Stokes emission appears of about equal intensity to the anti-Stokes emission. The appearance of angular Stokes emission is in sharp contrast to results[6] that show that the Raman process in a liquid is a two-step process with intermediate optical phonons involved and with no Stokes radiation observed at the matching angle. The emission frequency in the Raman process is well defined, while in the four-photon process the frequency is shifted continuously from 0 to as much as 6000 cm^{-1} on both the Stokes and anti-Stokes sides. Our process requires a modulation of the electronic nonlinear polarization.

2. Experimental Observation

The schematic of the experimental setup is shown in Fig. IV-2. In the experiment picosecond light pulses at 1.06 μ are generated from a dye Q-switched Nd:glass mode-locked laser. Second-harmonic generated (SHG) pulses at 5300 Å are derived by passing the beam through a potassium dihydrogen phosphate (KDP) crystal cut at the phase-matched angle. SHG pulses only are then collimated with an inverted telescope to a diameter of 1.2 mm and then passed through the samples. The energy per pulse is ~5 mJ and the pulse length is 4-8 psec so that the power is ~1 GW/cm^2. Five to ten filaments about 20 μ in diameter are formed in the sample so that the power in the filaments could be as high as ~10^4 GW/cm^2. Emission from the sample is displayed as a function of angle and wavelength by placing a lens at the focal distance from the 2-cm-high slit of a $\frac{3}{4}$ - m Jarrell-Ash spectrograph. The sample is near the lens so that light at a given wavelength emerging at the same angle with respect to the laser beam is imaged in a ring on the spectrograph slit. Anti-Stokes shifted light is displayed by placing either one or two 5-60 Corning filters before the lens to attenuate the main laser beam. Stokes light is displayed in an analogous fashion except that three 3-67 and three 3-68 filters are used to attenuate the main 5300 Å beam. Schematic angular spectra are shown in Fig. IV-3.

An anti-Stokes spectrum emitted from borosilicate BK-7 glass of length = 8.9 cm is shown in Fig. IV-4. The light is focused on the slit with a 10-cm focal length lens with the laser beam position at the center of the slit and the spectrograph turned to the second order. The whole anti-Stokes spectrum is

COUPLING OF FOUR PHOTONS

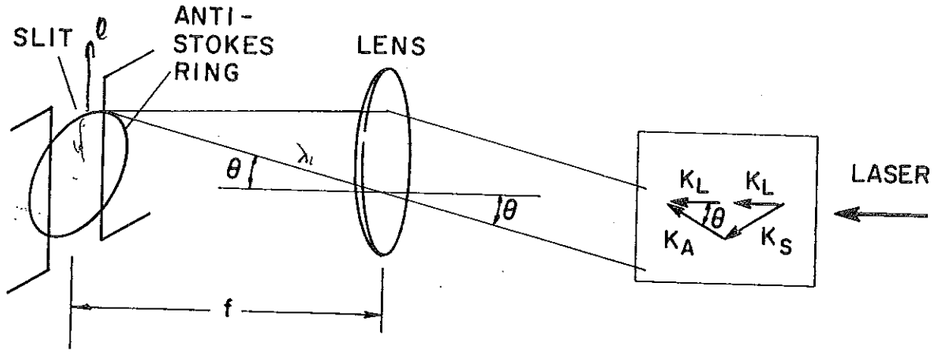

Fig. IV-2. Experimental arrangement for displaying the emission from materials as a function of wavelength and angle.

TYPICAL SPECTRA

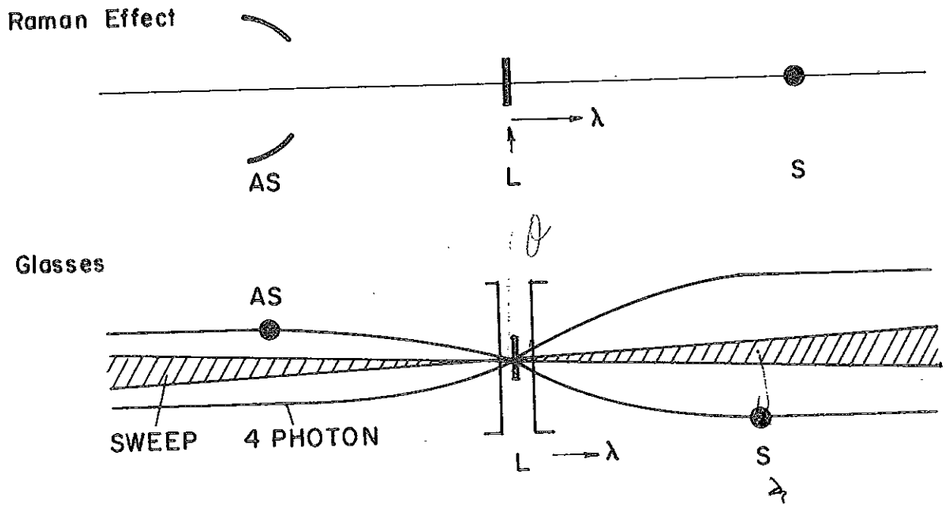

Fig. IV-3. Schematic wavelength and angular spectra for SRS (top) and for SPM and four-photon parametric emission (bottom).

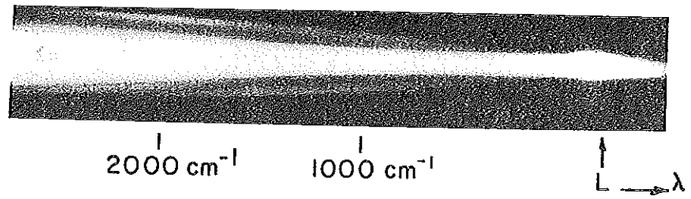

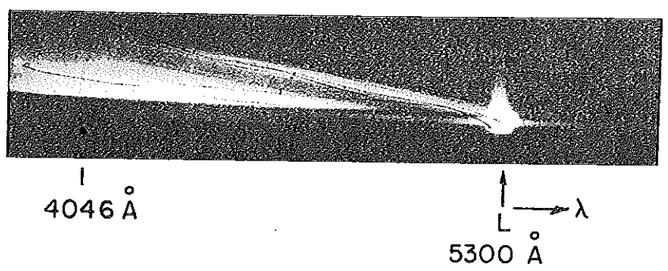

Fig. IV-4. (a) Angular anti-Stokes emission with main laser beam at slit center. Light in center is frequency swept light while outer curves are due to four-photon emission; (b) entire angular anti-Stokes emission curve from 4000 to 5300 Å for BK-7 glass, length 8.9 cm.

displayed with the spectrograph operating in the first order as shown in Fig. IV-4(b). The laser-beam position in Fig. IV-4(b) is near the bottom of the slit so that only the upper half of the anti-Stokes curve is displayed. In this fashion the entire angular variation of the anti-Stokes spectrum is displayed since the spectrum does not go off the slit at large emission angles.

Three salient features are evident in the spectra shown in Fig. IV-4. The first is four-photon continuous emission of radiation in the form of a curve extending from 4000 to 5300 Å, a shift of 6000 cm^{-1}. The intensity is uniform over this frequency range within a factor of 0.7 and is ~ 100 to 1000 times weaker than the laser intensity. The second feature is the forward-scattered frequency-swept radiation identified previously.[1] The third feature is the conical light emission which seems to begin near the forward direction at about 1000-cm^{-1} shift from the main laser line (it may possibly start at 0-cm^{-1} shift) and extends to 6000 cm^{-1}. This third feature is not yet understood but could possibly be frequency-swept light at small angles to the beam axis. This explanation is plausible in part because frequency-swept light at small angles could help to trigger the four-photon process. A similar spectral curve also appears on the Stokes side from 5300 to 7000 Å. A Stokes spectrum from BK-7 glass is shown in Fig. IV-5. Stimulated emission thus occurs over the entire visible region.

One outer curve which fluctuates in angle by about 10 percent at a given frequency always appears from shot to shot along with intense SPM, and this is the curve we analyze. Occasionally only SPM emission is observed, indicating a slightly higher threshold for the generation of this outer curve. One important experimental observation is that this emission at a particular wavelength varies in emission angle from shot to shot. Also curves do not usually go to zero angle at zero frequency shift. The experimental angle φ_A varies from ~ 0.01 to 0.03 at zero frequency shift from shot to shot. On the same shot the angular width of emission at a given frequency can be as large as $\Delta\varphi_A \sim 0.02$ although it can be less than $\Delta\varphi_A \sim 0.01$. This curve is compared with theory in the next section. Also experimentally extra curves of smaller diameter are often observed from shot to shot.

3. Theoretical Analysis

A theoretical model based on a four-photon coupling[2] between two strong waves (laser) and two weak waves (Stokes and anti-Stokes swept photons) via n_2 is presented to explain the angular emission. It is shown that gain occurs for the

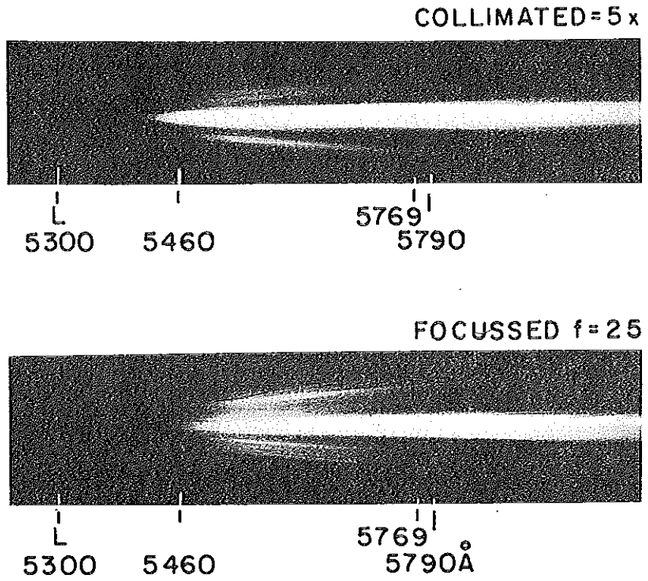

Fig. IV-5. Stokes emission from BK-7 glass, $\ell = 8.9$ cm. Filters 3-67. Light at center is SPM while outer curves are due to four-photon emission.

weak waves at particular angles governed by a momentum triangle between the four photons. In order to exactly fit the experimental data (emission angles for given wavelengths) to theory, emission from small scale filament must be taken into account.

Consider the interaction between four plane waves in a medium with an intensity dependent refractive index, n_2. The total electric field in the medium is

$$\bar{E} = \frac{\bar{E}_L}{2} + \frac{\vec{E}_L}{2} + \bar{E}_S + \bar{E}_A = \bar{E}_L + \bar{E}_S + \bar{E}_A \tag{1}$$

where E_L, E_S and E_A denote the electric field of incident laser, weak Stokes wave, and weak anti-Stokes wave, respectively. The form of the electric field for the plane waves are

$$E_i = \frac{1}{2}\,\mathcal{E}_i\, e^{i(\bar{k}_i \bar{r} - \omega_i t)} + \frac{1}{2}\mathcal{E}_i^{*}\, e^{-i(\bar{k}_i \bar{r} - \omega_i t)} \tag{2}$$

where $i = L, S,$ and A and k_i denotes the propagation constant and ω_i denotes the angular frequency for the i wave. We assume $\mathcal{E}_L > \mathcal{E}_A, \mathcal{E}_S$ — the weak waves negligibly affect the driving strong wave ($\mathcal{E}_L \sim$ constant). For appreciable energy exchange between the waves, the frequencies and propagation vectors of the weak and strong waves are related by

$$\omega_L - \omega_S = \omega_A - \omega_L \tag{3a}$$

$$\bar{K}_L - \bar{K}_S = \bar{K}_A - \bar{K}_L \text{ or } 2\bar{K}_L - \bar{K}_A - \bar{K}_S = 0. \tag{3b}$$

The relation 3b assumes the condition of exact phase matching among the four photons. A small momentum $\hbar\,\delta\bar{K}$ is introduced into Eq. 3b to take into account the effect of any mismatch among the photons propagation vectors:

$$\delta\vec{K} = 2\bar{K}_L - \bar{K}_A - \bar{K}_S. \tag{3c}$$

The weak wave gain in the four-photon process will be calculated using the frequency and momentum relationship given by Eq. 3a and 3c respectively. Two parameters Δ and $\bar{q}$ are introduced and defined via Eq. 3a and Eq. 3b:

$$\Delta \equiv \omega_L - \omega_S = \omega_A - \omega_L \tag{4a}$$

$$\bar{q} = \bar{K}_L - \bar{K}_S - \frac{\delta\bar{K}}{2} = \bar{K}_A - \bar{K}_L + \frac{\delta\bar{K}}{2} \tag{4b}$$

Here Δ and $\bar{q}$ are written only for mathematical convenience. These equations are analogous to Stokes-anti-Stokes coupling in stimulated Raman scattering (SRS), except Δ and $\bar{q}$ are allowed to vary — restricted only by the dispersion of the four photons involved. In the SRS there is an intermediate process involving the emission and absorption of an optical phonon ($\hbar\Delta$ and $\hbar\bar{q}$ are the energy and momentum of the phonon in SRS).

The form of the intensity dependent part of the dielectric constant assuming an electronic mechanism is given by:

$$\Delta\epsilon = \epsilon_2 E^2 \tag{5}$$

where

$$\epsilon_2 = 2n_o n_2. \tag{6}$$

The relationship between the nonlinear coefficients as readily obtained from $\epsilon = n^2$ where $\epsilon = \epsilon_o + \Delta\epsilon$ and $n = n_o + \Delta n$. The total polarization of the material is given by

$$P = \chi E = \frac{\epsilon - 1}{4\pi} E$$

or

$$P = \frac{\mathcal{E}}{2} e^{i[\bar{k}\cdot\bar{r} - \omega t]} + \frac{\mathcal{E}^*}{2} e^{-i[\bar{k}\cdot\bar{r} - \omega t]} \tag{7}$$

The nonlinear part of P due to the charge in the dielectric constant is

$$P^{NL} = \frac{\Delta\epsilon}{4\pi} E = \left(\frac{2\, n_o\, \Delta n}{4\pi}\right) E. \tag{8}$$

The $\Delta\epsilon$ is obtained by substituting Eq. 1 into Eq. 5:

$$\Delta\epsilon = \frac{\epsilon_2}{2}\Bigg\{ |\mathcal{E}_L|^2 + \mathcal{E}_L \mathcal{E}_S^* \, e^{i[\underbrace{(\bar{k}_L - \bar{k}_S)}_{\bar{q}+\delta\bar{k}/2}\cdot\bar{r} - \underbrace{(\omega_L - \omega_S)}_{\Delta} t]}$$

$$+ \mathcal{E}_L^* \mathcal{E}_S \, e^{-i[\underbrace{(\bar{k}_L - \bar{k}_S)}_{\bar{q}+\delta\bar{k}/2}\cdot\bar{r} - \underbrace{(\omega_L - \omega_S)}_{\Delta} t]} \qquad (9)$$

$$+ \mathcal{E}_L^* \mathcal{E}_A \, e^{i[\underbrace{(\bar{k}_A - \bar{k}_L)}_{\bar{q}-\delta\bar{k}/2}\cdot\bar{r} - \underbrace{(\omega_A - \omega_S)}_{\Delta} t]}$$

$$+ \mathcal{E}_L \mathcal{E}_A^* \, e^{-i[\underbrace{(\bar{k}_A - \bar{k}_L)}_{\bar{q}-\delta\bar{k}/2}\cdot\bar{r} - \underbrace{(\omega_A - \omega_L)}_{\Delta} t]} \Bigg\}$$

Notice, that under the differences between the $\bar{k}$'s and ω's in Eq. (9) are written the appropriate $\bar{q} \pm \delta\bar{k}/2$ and Δ. Here we have neglected terms oscillating at $2\omega_L$, $\omega_L + \omega_S$ and $\omega_L + \omega_A$ as well as higher order terms of $\mathcal{E}_A$, $\mathcal{E}_S$. These higher frequencies ($\lambda < 1770$ Å) and damped out in most materials (i.e., BK-7, calcite).

The exact form of P^{NL} is obtained by substituting Eq. (9) and Eq. (1) into Eq. (8). Neglecting terms oscillating at the second harmonic and using the relation given by Eq. (4):

$$P^{NL} = \frac{\epsilon_2}{8\pi}\Bigg\{ |\mathcal{E}_L|^2 (E_L + 2E_S + 2E_A) \qquad (10)$$

$$+ \frac{1}{2}\mathcal{E}_L^2 \mathcal{E}_S^* \, e^{i[(\bar{k}_A + \delta\bar{k})\cdot\bar{r} - \omega_A t]} + \frac{1}{2}\mathcal{E}_L^{*2} \mathcal{E}_S \, e^{-i[(\bar{k}_A + \delta\bar{k})\cdot\bar{r} - \omega_A t]}$$

$$+ \frac{1}{2}\mathcal{E}_L^{*2} \mathcal{E}_A \, e^{-i[(\bar{k}_S + \delta\bar{k})\cdot\bar{r} - \omega_S t]} + \frac{1}{2}\mathcal{E}_L^2 \mathcal{E}_A^* \, e^{i[(\bar{k}_S + \delta\bar{k})\cdot\bar{r} - \omega_S t]} \Bigg\}$$

The term containing $|\mathcal{E}_L|^2$ corresponds to the change in the velocity of the strong and weak waves while the last terms provides the cross-coupling between the waves and the energy transfer among them. The factor of 2 in front of E_S and E_A gives an additional index charge for the weak waves.

From Eqs. (10) and (8), the change in refractive index of the weak waves are

$$\Delta n_A = \frac{4\pi}{2 n_{oA}} \frac{\epsilon_2 \, 2|\mathcal{E}_L|^2}{8\pi} = \frac{1}{2} \frac{\epsilon_2 |\mathcal{E}_L|^2}{n_{oA}} \tag{11}$$

$$\Delta n_S = \frac{1}{2} \frac{\epsilon_2 |\epsilon_L|^2}{n_{oS}} ,$$

and of the strong wave is

$$\Delta n_{strong} = \Delta n_L = \frac{1}{4} \frac{\epsilon_2 |\mathcal{E}_L|^2}{n_L} . \tag{12}$$

where n_{oS} n_{oA}, n_L are the normal refractive index for the Stokes, anti-Stokes and laser waves. The weak wave index charge is twice as large as the strong wave giving an added retardation. Thus the relative index charge, which lengths $|\vec{k}_S|$ and $|\vec{k}_A|$ is

$$\Delta n = \Delta n_{weak} - \Delta n_{strong} \cong \frac{1}{4} \frac{\epsilon_2 |\mathcal{E}_L|^2}{n_L} . \tag{13}$$

The propagation constant for the weak waves are obtained from Equation (11):

$$|k_S|^2 = (k_{oS} + \Delta k_S)^2 = \left(\frac{n_{oS}\omega_S}{c} + \frac{\omega_S \Delta n_S}{c} \right)^2 \cong \frac{n_{oS}^2 \omega_S^2}{c^2} + \frac{\omega_S^2 \epsilon_2 |\mathcal{E}_L|^2}{c^2} ,$$

and (14)

$$|k_A|^2 \cong \frac{n_{oA}^2 \omega_A^2}{c^2} + \frac{\omega_A^2 \epsilon_2 |\mathcal{E}_L|^2}{c^2} .$$

The change in refractive index for the waves differ by a multiplicative constant of 3/2 if terms oscillating at $2\omega_L$, $\omega_L + \omega_S$, and $\omega_L + \omega_A$ are included in $\Delta\epsilon$.[7]

Next, the gain for the amplification of the weak waves and energy flow are calculated. The dielectric constant $\Delta\epsilon$ modulates the total field E to produce polarization source terms which drive Maxwell's wave equation:

$$\left(\nabla^2 - \frac{n_{oS}^2}{c^2} \frac{\partial^2}{\partial t^2} \right) \vec{E}_S = \frac{4\pi}{c^2} \frac{\partial^2}{\partial t^2} \vec{P}_S^{NL}$$

(15)

$$\left(\nabla^2 - \frac{n_{oA}^2}{c^2} \frac{\partial^2}{\partial t^2} \right) \vec{E}_A = \frac{4\pi}{c^2} \frac{\partial^2}{\partial t^2} \vec{P}_A^{NL} ,$$

where n_{oS} and n_{oA} are the normal index of refraction for the Stokes and anti-Stokes wave. The subscript on $\bar{E}_i$, $\bar{P}_i^{NL}$ are terms oscillating at $\mp i\omega_i t$. The waves are assumed linearly polarized parallel along x and are propagating along the z axis.

Maxwell's wave equations given by Eq. (15) are linearized[8] ($\frac{\partial^2 \mathcal{E}}{\partial z^2}$ are neglected) since $\mathcal{E}_S$ and $\mathcal{E}_A$ are assumed slowly varying functions of z (gain $\ll k_L$) and are reduced to:

$$-(k_{Sx}^2 + k_{Sz}^2)\frac{\mathcal{E}_S}{2} + 2i\frac{k_{Sz}}{2}\frac{\partial \mathcal{E}_S}{\partial z} + \frac{n_{oS}^2\,\omega_S^2}{c^2}\frac{\mathcal{E}_S}{2} = -\frac{4\pi\omega_S^2}{c^2}\left(\frac{\mathcal{P}_S^{NL}}{2}\right) \tag{16a}$$

and

$$-(k_{Ax}^2 + k_{Az}^2)\frac{\mathcal{E}_A^*}{2} - 2ik_{Az}\frac{\partial \mathcal{E}_A^*}{\partial z} + \frac{n_{oA}^2\,\omega_A^2}{c^2}\frac{\mathcal{E}_A^*}{2} = -\frac{4\pi\omega_S^2}{c^2}\left(\frac{\mathcal{P}_A^{NL*}}{2}\right) \tag{16b}$$

where

$$\left.\begin{aligned}
\frac{\mathcal{P}_S^{NL}}{2} &= \frac{\epsilon_2}{8\pi}\left\{2|\mathcal{E}_L|^2\frac{\mathcal{E}_S}{2} + \frac{1}{2}\mathcal{E}_L^2\,\mathcal{E}_A^*\,e^{i\delta\bar{k}\cdot\bar{r}}\right\}\\
\frac{\mathcal{P}_A^{NL}}{2} &= \frac{\epsilon_2}{8\pi}\left\{2|\mathcal{E}_L|^2\frac{\mathcal{E}_A}{2} + \frac{1}{2}\mathcal{E}_L^2\,\mathcal{E}_S^*\,e^{i\delta\bar{k}\cdot\bar{r}}\right\}
\end{aligned}\right\} \tag{17}$$

and taking complex conjugate of $\mathcal{P}_A^{NL}/2$ gives

$$\frac{\mathcal{P}_A^{NL*}}{2} = \frac{\epsilon_2}{8\pi}\left\{2|\mathcal{E}_L|^2\frac{\mathcal{E}_A^*}{2} + \frac{1}{2}\mathcal{E}_L^{*2}\,\mathcal{E}_S\,e^{-i\delta\bar{k}\cdot\bar{r}}\right\}.$$

We have written the Maxwell's wave equation for $\mathcal{E}_A^*$ (Eq. 16b) instead for $\mathcal{E}_A$ because the source term for the behavior of $\mathcal{E}_S$ (Eq. 16a) is proportional to $\mathcal{E}_A^*$. This technique allows us to simply solve the coupled equations (Eq. 16). Substituting Eqs. 14 for k^2 and 17 for $\mathcal{P}$ into Eq. 16, Maxwell's equation reduces to:

$$2ik_{Sz}\frac{\partial \mathcal{E}_S}{2z} = -\frac{\omega_S^2 \epsilon_2}{c^2}\left(\frac{1}{2}\,\mathcal{E}_L^2\,\mathcal{E}_A^*\,e^{i\delta\vec{k}\cdot\vec{r}}\right)$$

$$-2ik_{Az}\frac{\partial \mathcal{E}_A^*}{\partial z} = -\frac{\omega_A^2 \epsilon_2}{c^2}\left(\frac{1}{2}\,\mathcal{E}_L^{*2}\,\mathcal{E}_S\,e^{-i\delta k\cdot r}\right) \qquad (18)$$

Notice, the propagation constants k_S^2 and k_A^2 given by Eq. 14 have cancelled out the wave retardation for the weak waves in these equations.

The form of the trial solution for $\mathcal{E}_S$ and $\mathcal{E}_A^*$ is

$$\mathcal{E}_S = \mathcal{E}_{So}\,e^{i(\gamma+\frac{\delta k}{2})z}$$

$$\mathcal{E}_A^* = \mathcal{E}_{Ao}^*\,e^{i(\gamma-\frac{\delta k}{2})z} \qquad (19)$$

where γ is complex and $\mathcal{E}_{So}$, $\mathcal{E}_{Ao}$ are the noise amplitudes. (This form of solution is similar to the ones used by Giordmaine[9] for the 3-photon parametric effect.) Putting these trial solutions (Eq. 19) into the coupled equations, the exponents cancel out. The reduced equations become:

$$-2k_{Sz}(\gamma+\frac{\delta k}{2})\,\mathcal{E}_{So} = -\frac{\omega_S^2\epsilon_2}{2c^2}\,\mathcal{E}_L^2\,\mathcal{E}_{Ao}^*,$$

$$2k_{Az}(\gamma-\frac{\delta k}{2})\,\mathcal{E}_{Ao}^* = -\frac{\omega_A^2\epsilon_2}{2c^2}\,\mathcal{E}_L^2\,\mathcal{E}_{So}. \qquad (20)$$

These are two linear homogeneous algebric equations. For a nontrivial solution to exit, the determinant of the coefficients of $\mathcal{E}_{So}$ and $\mathcal{E}_{Ao}^*$ must vanish:

$$\begin{vmatrix} -2k_{Sz}(\gamma+\frac{\delta k}{2}) & \frac{\omega_S^2\epsilon_2\,\mathcal{E}_L^2}{2c^2} \\ \frac{\omega_A^2\epsilon_2}{2c^2}\,\mathcal{E}_L^{*2} & 2k_{Az}(\gamma-\frac{\delta k}{2}) \end{vmatrix} = 0. \qquad (21)$$

Hence, solving for γ:

$$\gamma_{\pm} = \pm i \left(\frac{\omega_A^2 \omega_S^2 \epsilon_2^2 |\mathcal{E}_L|^4}{16\, C^4 k_{Sz} k_{Az}} - \left(\frac{\delta k}{2}\right)^2 \right)^{1/2} \tag{22}$$

For power gain $\propto \mathcal{E}\mathcal{E}^* \propto |\mathcal{E}_o|^2 e^{-2 \mathrm{Im}\gamma_- \ell}$, the gain

$$g = -2\ \mathrm{Im}\ \gamma_- = 2 \left(\frac{\omega_A^2 \omega_S^2 \epsilon_2^2 |\mathcal{E}_L|^4}{16\, C^4 k_{Sz} k_{Az}} - \left(\frac{\delta k}{2}\right)^2 \right)^{1/2} \tag{23}$$

The positive solution γ_+ damps out for large $g\ell$. Maximum gain occurs when $\delta k = 0$ and is given by

$$g_o = \frac{2 \omega_A \omega_S \epsilon_2 |\mathcal{E}_L|^2}{4 C^2 \sqrt{k_{Sz} k_{Az}}} \equiv 2 \gamma_o . \tag{24}$$

where $k_{Sz} = k_S \cos \theta_S$ and $k_{Az} = k_A \cos \theta_A$, and θ_S, θ_A are the emission angles for Stokes and anti-Stokes waves.

The gain given by Eq. 23 or Eq. 24 depends only slightly on angle through the term $1/\sqrt{\cos \theta_A \cos \theta_S}$. This angle factor ≈ 1 since $n_S \theta_S$ and $n_A \theta_A$ are observed to be less than 8° and $\cos \theta_S$ and $\cos \theta_A \leq 0.990$. Substituting $\omega_A = \omega_L + \Delta$, $\omega_S = \omega_L - \Delta$ and the approximations $\sqrt{\cos \theta_S \cos \theta_A} \cong 1$ for angles $\leq 8°$ and $\sqrt{n_A n_S} \cong n_L$ into Eq. 24, the phase matched gain reduces to:

$$g_o \cong \frac{\omega_L \epsilon_2 |\mathcal{E}_L|^2}{2 n_L c} - \left(\frac{\Delta^2}{2\omega_L^2} \right)^2 \frac{\omega_L \epsilon_2 |\mathcal{E}_L|^2}{2 n_L c} . \tag{25}$$

For a frequency shift $\frac{\Delta}{2\pi c} \sim 4000\ \mathrm{cm}^{-1}$ and $\frac{\omega_L}{2\pi c} \sim 19{,}000\ \mathrm{cm}^{-1}$, $\frac{1}{2}\left(\frac{\Delta}{\omega_L}\right)^2 \sim \frac{1}{45}$. Therefore, by neglecting the second term in Eq. 25 would lead to an error $\leq 2.2\%$ in the gain calculated for frequencies within a $4000\ \mathrm{cm}^{-1}$ range. Hence, the gain is approximately constant over a $\pm 4000\ \mathrm{cm}^{-1}$ frequency shift and for a 8° phase matched angle variation — a fact observed experimental!

Using Eq. 25 to evaluate the gain for typical parameters for BK-7 glass: $n_2 = 3 \times 10^{-13}$ esu, $\omega_L/c \sim 1.18 \times 10^5\ \mathrm{cm}^{-1}$, $\Delta = 0$, and $|\mathcal{E}_L| \sim 1.3 \times 10^4$ esu gives

$$g_o \sim \frac{\omega_L n_2 |\mathcal{E}_L|^2}{c} = 6 \text{ cm}^{-1}. \tag{26}$$

For an interaction length of 3 cm, $g_o \ell = 18$ which is a comparable gain to SRS gain in solids and liquids.[10] Therefore, there is sufficient gain for the four-photon parametric process to be readily observed!

The complete solution for $\mathcal{E}_S$ and $\mathcal{E}_A^*$ are

$$\mathcal{E}_S = \mathcal{E}_{So1} e^{+\gamma x + i \delta k x/2} + \mathcal{E}_{So2}^* e^{-\gamma x + i \delta k x/2} \tag{27}$$

and

$$\mathcal{E}_A^* = \mathcal{E}_{Ao1} e^{+\gamma x + i \delta k x/2} + \mathcal{E}_{Ao2}^* e^{-\gamma x + i \delta k x/2}$$

where $\gamma \equiv \sqrt{\gamma_o^2 - (\delta k/2)^2}$, and $\mathcal{E}_{So1}$, $\mathcal{E}_{So2}$, $\mathcal{E}_{Ao1}^*$ and $\mathcal{E}_{Ao2}^*$ are determined by the boundary condition at $z = 0$. Assuming that no Stokes or anti-Stokes waves are present at $z = 0$, the solution becomes:

$$\mathcal{E}_S = \mathcal{E}_{So1} \left(e^{\gamma x} - e^{-\gamma x} \right) e^{i \delta k x/2} \tag{28}$$

and

$$\mathcal{E}_A^* = \mathcal{E}_{Ao1}^* \left(e^{\gamma x} - e^{-\gamma x} \right) e^{i \delta k x/2}.$$

The power flow $\propto \mathcal{E}\mathcal{E}^*$ over a distance ℓ for the Stokes or the anti-Stokes is:

$$P = P_o \left\{ e^{(\gamma+\gamma^*)\ell} + e^{-(\gamma+\gamma^*)\ell} - \left(e^{(\gamma-\gamma^*)\ell} + e^{-(\gamma-\gamma^*)\ell} \right) \right\} \tag{29}$$

where P_o is the power density at the entrance of the crystal. (The zero-point fluctuation noise power $P_o = \epsilon h\nu \Delta\nu / A$ where $\Delta\nu$ is the bandwidth, ϵ is the number of modes of the laser, and A is beam area.) The power flow equation reduces to:

$$P = 2P_o \left\{ \cosh (2\ell \operatorname{Re}\gamma) - \cos (2\ell \operatorname{Im}\gamma) \right\} \tag{30}$$

where Re and Im means take real and imaginary part of γ respectively. For large $\gamma\ell$ (gain), the power flow becomes

$$\frac{P}{P_o} \sim e^{2\gamma\ell} = e^{-2\ell \operatorname{Im}\gamma}. \tag{31}$$

$P_o \sim 10^{-1} - 10^{-2}$ W/cm^2 for $\epsilon \sim 10^3$, $\Delta\nu \sim 10^{12}$ sec^{-1}, $h\nu \sim 10^{-12}$ ergs, and $A \sim 10^{-2}$ cm^2. For $g_o \ell \sim 20$, $P \sim 10^7$ W/cm^2. The normalized power flow versus momentum mismatch ($\delta k/2$) is plotted in Fig. IV-6 for various γ_o and interaction length, ℓ. For $g_o \ell < 4$ the power profile has a central peak about the phase matching angle ($\delta k = 0$) and an oscillatory behavior about this angle (finite δk). For larger $g_o \ell$ the peak about $\delta k = 0$ dominates. Notice, for $\gamma_o = 10$ cm^{-1} and $\ell = 0.5$ cm (Fig. 6-b) that the 1/2 power point occurs at $\delta k/2 \cong \pm 3.5$ cm^{-1} and zero gain occurs at $\delta k/2 = \pm 10$ cm^{-1}. A momentum mismatch of $\delta k/2 = \pm 10$ cm^{-1} transform to an angular spread[11] of $\leq \pm 0.163$ degrees for photons emitted for angles $\geq \pm 2$ degrees. Therefore, four-photon gain occurs over a small angular spread — 0.326 degrees about the phase matching angle of 2°, for this case. The experimental observed angular spread measured outside the crystal is $\Delta\varphi_A \sim 0.1$ rad. Correcting for the refractive index, the experimental angular spread inside the crystal is $\Delta\varphi_A/n_A \sim 0.38$ degrees — fair agreement with the calculated angle spread of .326°.

Historically, two types of SRS anti-Stokes radiation have been reported called class I and class II. Class I radiation was first observed in calcite[12] and obeys the volume phase-matching equation $\vec{K}_L + \vec{K}_L = \vec{K}_A + \vec{K}_S$. Class II radiation fails to obey the volume phase-matching relation and originates in filaments.[10] Detailed explanations of anti-Stokes radiation from filaments have been given by Shimoda[13,14] and Sacchi, Townes, and Lifsitz.[15] Shimoda[13] calculated the angular emission for a general four-photon coupling created from "the interference of radiation produced by dipole in filaments."[13] He showed that class I emission dominates when the diameter of the filaments were $\gg 200\,\mu$. However, for small diameter filaments $\ll 200\,\mu$ in diameter, class II emission is observed.

In the following section, the theoretical angles for Class I and class II emission[13] will be compared with the experimental observed emission angles from BK-7 glass.

In Fig. IV-7 different four-photon scattering processes are compared with one of our experimentally measured curves. The first curve labeled I is calculated for volume phase matching where $2\vec{K}_L = \vec{K}_A + \vec{K}_S$. Refractive indices for borosilicate BK-7 glass are known accurately to five decimal places,[16] and thus the calculated curve is accurate. Class I radiation originates either from phase matching over a large volume or from phase matching in large-diameter filaments. Curve I deviates from the experimental curve for two main reasons: (1) the light is formed in small filaments of diameter $\sim 20\,\mu$ and (2) high-power short-pulse lasers which are multimode induce a nonlinear refractive index

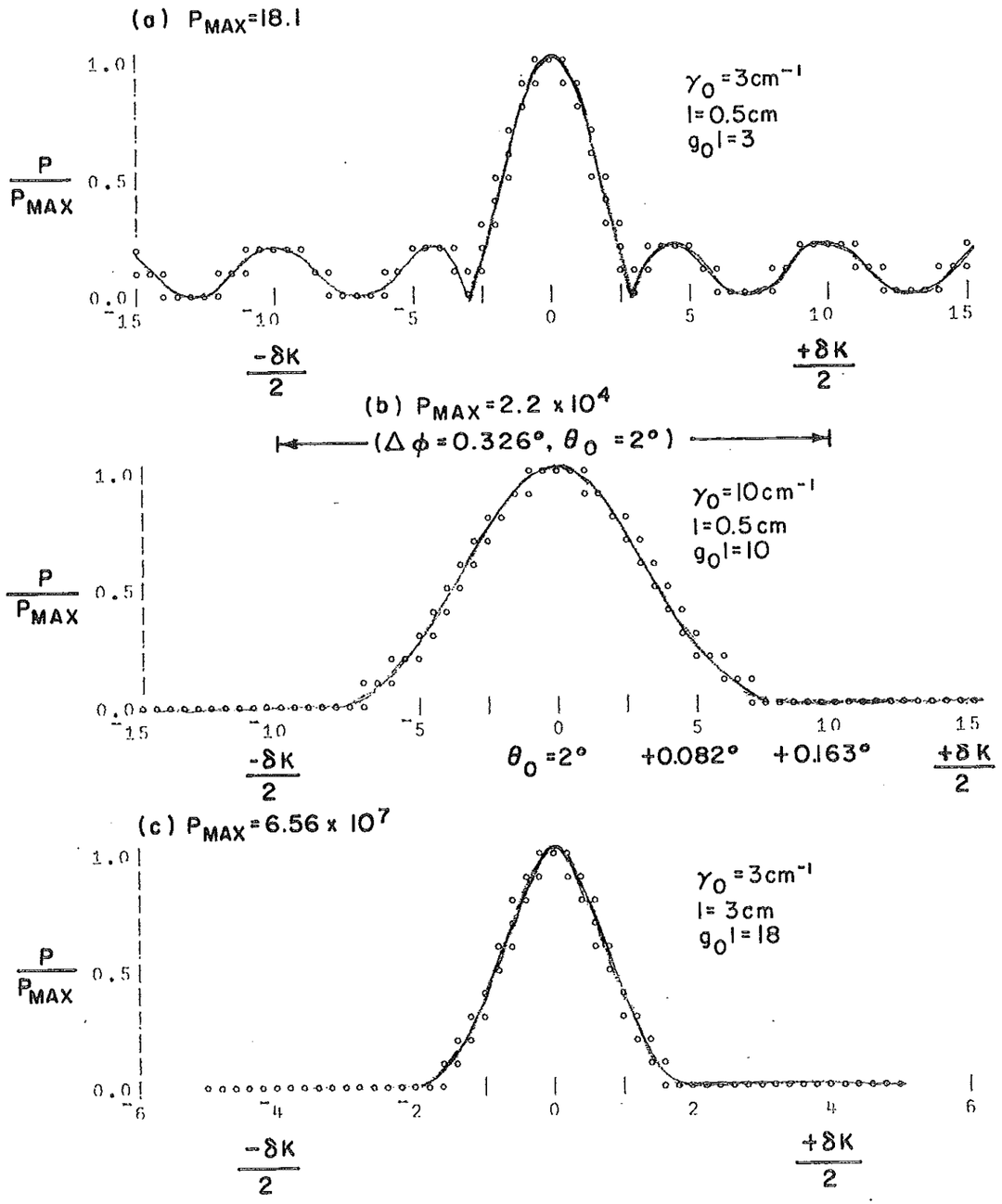

Fig. IV-6. Calculated four-photon power flow versus momentum mismatch centered at the phase matching anti-Stokes angle for the following parameters (a) $\gamma_0 = 3\ \mathrm{cm}^{-1}$, $\ell = 0.5$ cm, $g_0\ell = 3$; (b) $\gamma_0 = 10\ \mathrm{cm}^{-1}$, $\ell = 0.5$ cm, $g_0\ell = 10$; (c) $\gamma_0 = 3\ \mathrm{cm}^{-1}$, $\ell = 3$ cm, $g_0\ell = 18$. The zero-point flucutation noise power, $P_0 \sim 10^{-2}$ watts/cm^2 - 10^{-1} watts/cm^2.

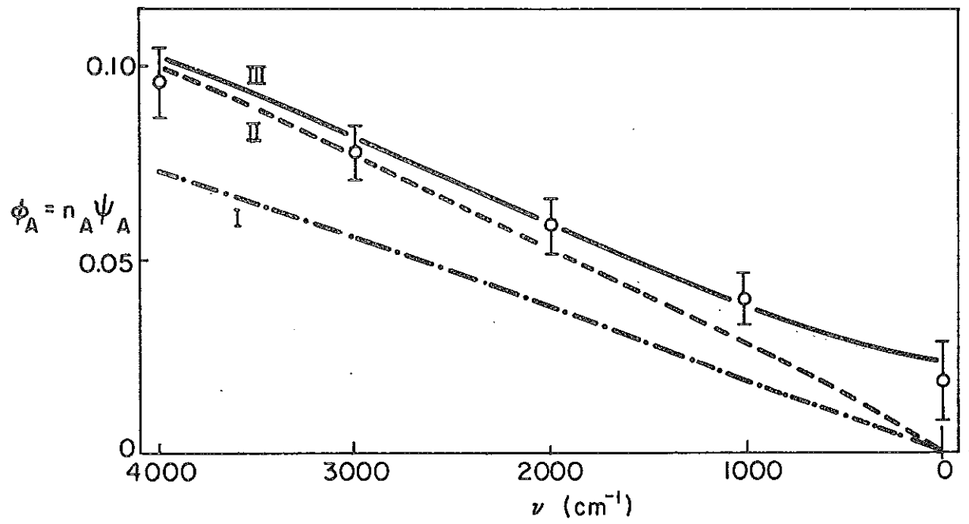

Fig. IV-7. Anti-Stokes angle outside materials: circles, experimental points; dash-dot, curve I calculated for Class-I emission; dash, curve II calculated for Class-II emission; solid line, curve III calculated for small scale filaments plus a nonlinear index change.

change in the material. The Class-I model correctly predicts one qualitative feature, however — the greater angle of emission at a given frequency shift for the Stokes curve than for the anti-Stokes curve and by about the right amount, i.e., $\varphi_S = (K_A/K_S)\varphi_A$ at small angles where φ_S is the Stokes emission angle and φ_A is the anti-Stokes emission angle.

The curve labeled II in Fig. IV-7 is a calculated curve for Class-II emission from small-scale filaments. Following Shimoda[13] (Eq. 17) the anti-Stokes angle φ_A is calculated from

$$\varphi_A^2 = 2\Delta K_A/K_A - a^2/2\ell^2, \tag{32}$$

where $\Delta K_A = K_A + K_S - 2K_L$, 2a is the filament diameter, and ℓ is the filament length. Unfortunately it is not clear which values to use for a/ℓ. Taking $a = 10\mu$ and ℓ = 2mm to 1 cm, which are typical experimental values, the term $a^2/2\ell^2$ is small compared with $2\Delta K_A/K_A$. As shown in Fig. IV-7 the curve labeled II and calculated from $\varphi_A^2 = 2\Delta K_A/K_A$ is much closer to the experimental data than the volume phase-matching curve labeled I.

An important correction to the emission angle is produced by the nonlinear change of refractive index induced by the short, intense laser pulses. This correction tends to increase both anti-Stokes and Stokes emission angles and is most important at small angles. Chiao, Kelley, and Garmire[2] have shown that the refractive index increase for weak waves is twice that of the strong wave. This is verified by Eqs. 11 and 12. Thus instead of Eq. (32) for the radiation angle for the filaments we write a new ΔK_A, $\Delta K_A'$, which takes into account the nonlinear increase in refractive index, i.e., $\Delta K_A' = (K_A + 2\Delta K) + (K_S + 2\Delta K) - 2(K_L + \Delta K)$ so that

$$\varphi_A^2 = \frac{2\Delta K_A}{K_A} + \frac{4\Delta K}{K_A} - \frac{a^2}{2\ell^2}, \tag{33}$$

where $\Delta K = \Delta n_L \omega_L/c$ and Δn_L is the change of refractive index for strong wave induced by the intense pulse. The electronic index change Δn_L for the strong wave is $\frac{1}{4}\epsilon_2|\mathcal{E}_L|^2/n_L$ while for the weak waves Δn_S, $\Delta n_A \cong \frac{1}{2}\epsilon_2|\mathcal{E}_L|^2/n_L$ where ϵ_2 is the electronic Kerr coefficient. For a laser pulse which changes n for the strong wave by 10^{-4}, Eq. (33) is plotted in Fig. IV-7. This curve, labeled III provides an excellent fit to the experimental data and is a reasonable model because it takes into account both that the radiation pattern is from filaments and

that the refractive index increases as a result of short, intense pulses. Equation (33) provides an explanation of the finite emission angle observed at zero frequency shift because of the refractive index increase. Fluctuations in emission angle from shot to shot as well as the extra curves observed experimentally could be explained by the $a^2/2\ell^2$ and $4\Delta K/K_1$ terms in Eq. (33) which vary for different filaments

Figure IV-8 shows angular spectra from calcite. We do observe Class II Raman anti-Stokes ring besides an angular emission from calcite. The Raman ring angle as measured from Fig. IV-8 is 3.75° when the laser (5300 Å) propagates as an O-wave in the calcite.[17] This ring angle agrees with the class II ring angle calculated from $2n_A\varphi_A^{II} = 2n_A (2\Delta K_A/K_A) = 3.758°$. (The calculated Class I ring angle is $2n_A\varphi_A^{I} = 2.61°$).

The four-photon coupling mechanism in borosilicate glass is surely electronic,[4] but in liquids a possible coupling mechanism could be the optical orientational Kerr effect, although this mechanism appears to be ruled out since the spectral extent in liquids are thousands of wavenumbers which is much greater than the inverse of the orientational relaxation times. In summary, four-photon stimulated emission has been observed in BK-7 glass under high power 5300 Å picosecond pulse excitation. The emission is generated from 4000 Å to 7000 Å from filaments formed in the glass, the wavelength depending on emission angle. The gain, energy flow, and angular dependence of the process are calculated and compared with this experiment. In veiw of experimental complications — i.e., short intense pulses, filaments, self-phase modulation — agreement between experiment and theory is excellent.

4. Future Direction

A tunable device will be investigated in the near future. Four-photon parametric oscillation should be enhanced by placing resonator mirrors at the Stokes or anti-Stokes emission angles.

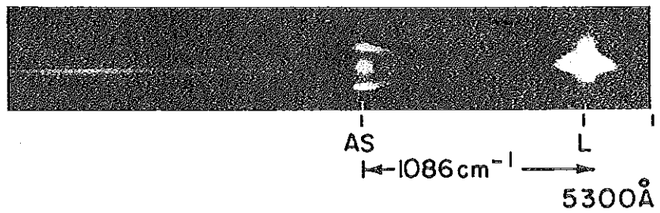

AS RING: $\psi_{EXP} = 3.57°$
FILTER = 5-60, 5-61
ℓ = 6.5 cm
FOCUSED: f = 25 cm
ANGULAR: f = 10 cm

Fig. IV-8. Angular anti-Stokes spectra from calcite for O-wave excitation. Length 6.5 cm; beam is focused by f = 25 cm; filters: 5-60 and 5-61; and the collecting lens f = 10 cm is located 10 cm from the slit of spectrograph.

IV - REFERENCES

1. R. R. Alfano and S. L. Shapiro, Phys. Rev. Letters 24, 584 (1970).

2. R. Y. Chiao, P. L. Kelley, and E. Garmire, Phys. Rev. Letters 17, 1158 (1966).

3. R. L. Carman, R. Y. Chiao, and P. L. Kelley, Phys. Rev. Letters 17, 1281 (1966).

4. R. R. Alfano and S. L. Shapiro, Phys. Rev. Letters 24, 592 (1970).

5. E. Garmire, F. Pandarese, and C. H. Townes, Phys. Rev. Letters 11, 160 (1963).

6. H. J. Zeiger, P. E. Tannenwald, S. Kern, and R. Herendeen, Phys. Rev. Letters 11, 419 (1963).

7. Keeping terms oscillating at $2\omega_L$, $\omega_L + \omega_S$ and $\omega_L + \omega_A$ and $\delta k = 0$, the nonlinear dielectric constant is:

$$\Delta\epsilon = \frac{\epsilon_2}{2}\left\{ |\mathcal{E}_L|^2 + \frac{1}{2}\,\mathcal{E}_L^{*2}\, e^{-2i(\bar{k}_L\cdot\bar{r} - \omega_L t)} + c.c \right.$$

$$+ \mathcal{E}_L^{*}\mathcal{E}_S\, e^{-i[\underbrace{(\bar{k}_L - \bar{k}_S)}_{\bar{q}}\cdot\bar{r} - i\underbrace{(\omega_L - \omega_S)}_{\Delta}t]} + c.c$$

$$+ \mathcal{E}_L^{*}\mathcal{E}_A\, e^{i[\underbrace{(\bar{k}_A - \bar{k}_L)}_{\bar{q}}\cdot\bar{r} - i\underbrace{(\omega_A - \omega_L)}_{\Delta}t]} + c.c$$

$$+ \mathcal{E}_S\mathcal{E}_L\, e^{i[(\bar{k}_S + \bar{k}_L)\cdot\bar{r} - (\omega_L + \omega_S)t]} + c.c$$

$$\left. + \mathcal{E}_A\mathcal{E}_L\, e^{i[(\bar{k}_A + \bar{k}_L)\cdot\bar{r} - (\omega_L + \omega_A)t]} + c.c \right\},$$

and the nonlinear polarization is:

$$P^{NL} = \frac{\epsilon_2}{8\pi}\left\{ \frac{3}{2}\,|\mathcal{E}_L|^2 (E_L + 2E_S + 2E_A) \right.$$

$$+ \frac{1}{2}\,\mathcal{E}_L^{*2}\,\mathcal{E}_S\, e^{i\omega_A t - i\bar{k}_A\cdot\bar{r}} + c.c$$

$$\left. + \frac{1}{2}\,\mathcal{E}_L^{*2}\,\mathcal{E}_A\, e^{i\omega_S t - i\bar{k}_S\cdot\bar{r}} + c.c \right\}$$

From this P^{NL} the change in refractive index for weak waves is

$$\Delta n_{weak} \cong \frac{4\pi}{2n_L}\left(\frac{3}{2}\,\frac{\epsilon_2}{8\pi}\,2\,|\mathcal{E}_L|^2\right) = \frac{3}{4}\,\frac{\epsilon_2}{n_L}\,|\mathcal{E}_L|^2$$

and of the strong wave is

$$\Delta n_{strong} = \frac{3}{8}\,\frac{\epsilon_2}{n_L}\,|\mathcal{E}_L|^2.$$

The relative change is

$$\Delta n = \Delta n_{weak} - \Delta n_{strong} \cong \frac{3}{8}\,\frac{\epsilon_2 |\mathcal{E}_L|^2}{n_L}.$$

These index changes are only valid for u.v. transparent materials. However the gain equation (Eq. (23) is still the same since the extra retardation is cancelled out by choice of k^2.

8. The time dependence of the electric field is assumed and treated as a constant in time because the four-photon parametric process is assumed electronic tronic in origin (i.e., harmonic generation and three-photon parametric effect). There is no intermediate real excitation involved in this process. This is different from SRS where phonons play intermediate real excitation with a lifetime ~of the laser's pulsewidth.

9. J. A. Giordmaine in Quantum OPTICS, edited by R. J. Glauber, International School of Physics, Course XLII, Academic Press, 492 (1969).

10. E. Garmire, Thesis, Massachusetts Institute of Technology, 1965 (unpublished).

11. To obtain the transform from a momentum mismatch to an angular spread in the four-photon process, we assume $K_A = K_A + \delta K$ and $\theta_S = \theta_{So} + \delta\theta$.

These changes are shown in the momentum triangles

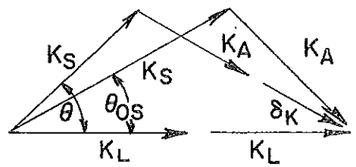

From trigonometry the equations are obtained from these triangles:

$$K_S^2 + 4K_L^2 - 4K_L K_S \cos\theta_o = K_A^2$$
$$K_S^2 + 4K_L^2 - 4K_L K_S \cos\theta = (K_A + \delta K)^2.$$

Solving these equations gives

$$\delta\theta \cong \frac{\delta K/2}{K_L \sin\theta_{oS}} \text{ rad.}$$

12. R. Y. Chiao, and B. P. Stoicheff, Phys. Rev. Letters 12, 290 (1964).

13. K. Shimoda, Japan J. Appl. Phys. 5, 86 (1966).

14. K. Shimoda, Japan. J. Appl. Phys. 5, 615 (1966).

15. C. A. Sacchi, C. H. Townes, and J. R. Lifsitz, Phys. Rev. 174, 439 (1968).

16. Optical Glass Tables, Jena Glaswerk Schott and Gen, Mainz, Germany, p. 18.

17. In Figure 8, there is also an axial emission from the anti-Stokes Raman process (ASR) with a total angular spread of 1.15° and from SPM. The reason is not understood for the axial ASR but it may result from non-self focused laser light where a is large, and the term $a^2/2\ell^2$ in Eq. 32 may be as large as $2\Delta K_A/K_A$.

V. DIRECT MEASUREMENT OF OPTICAL PHONON LIFETIME

1. Introduction

Despite the importance and great interest in the temporal behavior of an optical phonon in solid-state physics and nonlinear optics, the optical-phonon lifetime has never been measured directly. In the past the lifetime has been deduced from the linewidth of spontaneous Raman scattering and neutron scattering data. This lifetime is typically $\sim 10^{-11}$ sec, too short to measure directly by conventional means. The advent of a mode-locked laser with resolution on a picosecond scale makes such a measurement possible. This section reports on the first direct measurement[1] of an optical-phonon lifetime in a crystal. A calcite crystal has been chosen for this experiment. The experimental techniques for measuring the phonon lifetime are discussed along with a theoretical analysis on the underlying physical principles.

The essential features of the phonon spectra of a crystal are best illustrated by the consideration of a simple diatomic lattice. As shown in Fig. V-1 dispersion curve ω versus k for this lattice consists of three acoustic branches and three optical branches. A phonon is a quantized lattice vibration characterized by its energy $\hbar\omega$ and crystal momentum $\hbar k$. The optical modes arise from atoms vibrating against one another while the acoustical modes arise from atoms moving together. When the displacement of the atoms are parallel (perpendicular) to the propagation direction of the phonon wave, the polarization of the phonon wave is said to be longitudinal (transverse). In thermal equilibrium the phonon occupancy at given k is given by the Bose-Einstein distribution: $n_k = [e^{\hbar\omega/k_B T} - 1]^{-1}$ where k_B is the Boltzmann constant and T is the temperature.

The anharmonic terms of the lattice potential energy gives rise to the coupling between different phonons.[2] A given phonon may collide or scatter with other phonons in the crystal, or it may break up into multi-phonons. The dominate phonon-phonon interaction at high temperature is the scattering among the thermal phonons while at low temperatures a phonon spontaneously breaks up into two other phonons. These multi-phonon processes via the anharmonicity of the crystal give rise to the thermal properties of the materials.[2] The dispersion curve of the material and the conservation of energy and crystal momentum restricts the phonons involved in the decay process of a given phonon. For illustration, Fig. V-2 depicts the spontaneous decay of an optical phonon into two acoustic phonons.

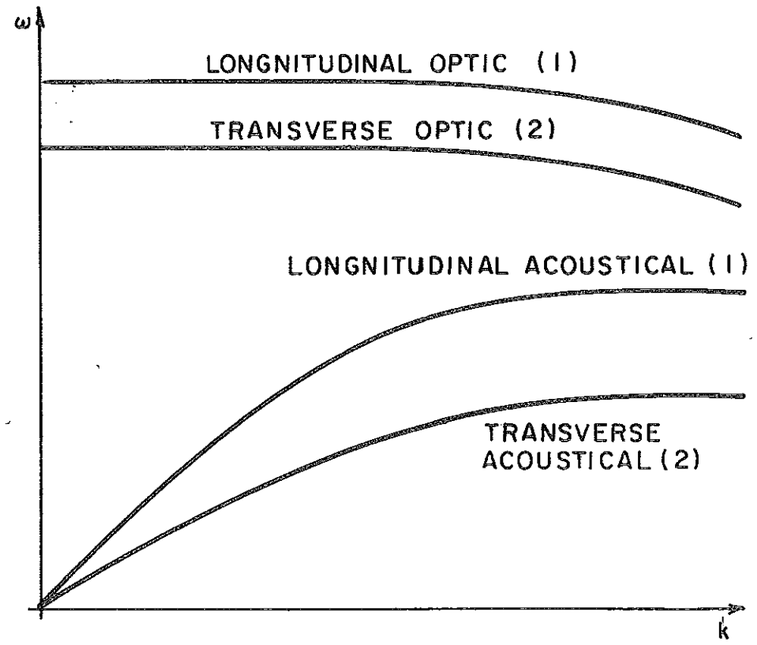

Fig. V-1. Phonon dispersion curve of diatomic lattice.

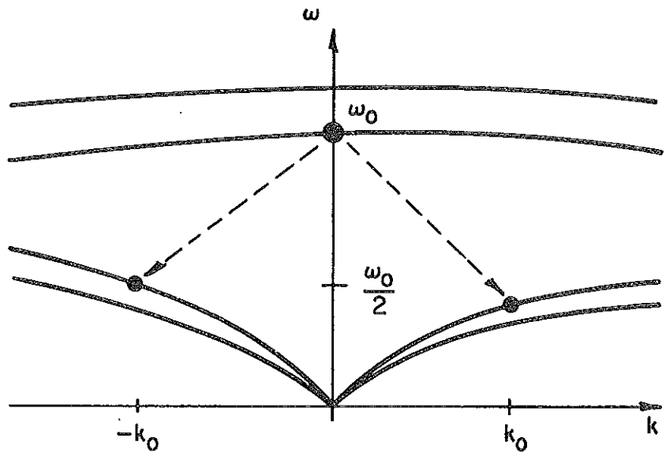

$$\omega_0 = \omega_1 + \omega_2$$
$$\bar{k}_0 = \bar{k}_1 + \bar{k}_2$$

Fig. V-2. Decay of optical phonon into two acoustic phonons.

The phonon dispersion curve of calcite ($CaCO_3$) is not known. There are two molecules of $CaCO_3$ per unit cell with five atoms per molecule. Therefore, there are (3) (5) (2) = 30 branches — including five Raman active vibrations and eight infrared active vibrations.[3] Stimulated Raman scattering (SRS) in calcite is only observed for the totally symmetric 1086 cm^{-1} phonons because of the large Raman cross section. The SRS gain[4] (cm^{-1}) at 5300 Å for calcite is 5.5 I_L which is comparable to the gain for benzene of 5.2 I_L where I_L is the intensity of the laser in GW/cm^2. The Raman linewidth of 1086 cm^{-1} has been measured by Park[4] at various temperatures. This linewidth data suggests that two different mechanisms for the decay of the 1086 cm^{-1} phonon is operative below and above 200°K. Above the temperature of 200°K the dominate decay mechanism is probably due to the scattering of the 1086 cm^{-1} phonon with the thermal phonon background while below this temperature the 1086 cm^{-1} phonons are spontaneously breaking up into two phonons due to the lattice anharmonicity. In this section of the thesis, the lifetime of the 1086 cm^{-1} phonon in calcite is measured directly in the different phonon decay regimes — above and below 200°K.

2. Experimental

In the experiment a high-power picosecond laser beam operating at a wavelength of 1.06 μm creates the optical phonons in calcite by stimulated Raman scattering (SRS). A second, but much weaker, picosecond laser beam operating at a wavelength of 0.53 μm, acting as a probe, travels along a variable optical delay path and undergoes Raman scattering off the created phonons. Such probe scattering off created phonons in calcite has been previously demonstrated,[6] and collisional de-excitation of vibrational levels in hydrogen gas[7] of the order of 10^{-5} sec and acoustic-phonon lifetimes in liquids[8] of the order of 10^{-7} sec have been measured previously by probe techniques. The decay rate of the optical-phonon population is obtained by measuring the intensity of the Raman light produced by the probe as a function of delay between the laser and probe pulses.

To obtain substantial interaction between the probe laser pulses (0.53 μ) and the created flux of optical phonons (1086 cm^{-1}): (1) the probe laser beam must be Raman phase-matched to the phonons, and (2) the energy of the probe pulses (0.53 μ) and exciting laser pulses (1.06 μ) must propagate collinearly and stay spatially coincident. In isotropic materials, the normal dispersion of the refractive index would not allow these two conditions to be obeyed. However,

the large birefringence of calcite allows the above conditions to be satisfied. The 1.06 μ laser which generates the flux of phonons is polarized as an ordinary wave while the 0.53 μ probe laser beam is polarized as an extraordinary wave.

Following the analysis of Giordmaine[6] of probe scattering from phonons, the angles of incidence, refraction and transmission for the exciting laser (1.06 μ) probe laser beam (0.53 μ), and the Raman scattered beams (1.19 μ, 0.56 μ) are calculated satisfying the above two conditions. Before calculating these angles it is necessary to review the relevant and important aspects of crystal optics[9] related to the scattering process.

The emphasis is now placed on the passage of linear polarized light through an optically anisotropic crystal. Such a crystal is called birefringent. The velocity of the light in a birefringent crystal, in general, varies with direction of propagation. The refractive index depends on the angle of incidence. An unpolarized light beam entering an anisotropic crystal will divide into two rays which travel at different velocities and in different directions. This process is called double refraction. A ray is defined as the path followed by the energy of the light wave as it propagates from one point to another in the crystal. The wave front of the light wave is a surface passing through all points on the wave having the same phase. The wave normal or wave vector $\vec{k} = n\omega\hat{k}/c$ is perpendicular to the front and according to Maxwell's equations, it is perpendicular to $\vec{D}$ and $\vec{H}$ (displacement and magnetic intensity) which forms the light wave. There is one direction of propagation where double refraction does not occur. This direction in the crystal is called the optic axis. The change of refractive index with direction of propagation of the light is visualized by using an indicatrix — a geometrical figure showing the variation of indices of refraction in the crystal with propagation direction and state of polarization. This is shown in Fig. V-3 for an uniaxial crystal. The refractive index n_o is called the ordinary index and n_e is called the extraordinary index. For a polarized light wave vibrating in a plane including the optic axis, the crystal has refractive index which depends on the direction of propagation of the wave (a mixture of n_o and n_e). Such a wave is called an extraordinary wave or E-wave. The index of refraction for a wave vibrating parallel to the optics axis is either a maximum or a minimum depending on whether the crystal is positive ($n_e > n_o$) or negative ($n_o > n_e$). Calcite is a negative crystal. For a polarized light wave vibrating in a plane perpendicular to the optic axis, the index of refraction is the same for any propagation direction. Such a wave is called an ordinary wave or O-wave.

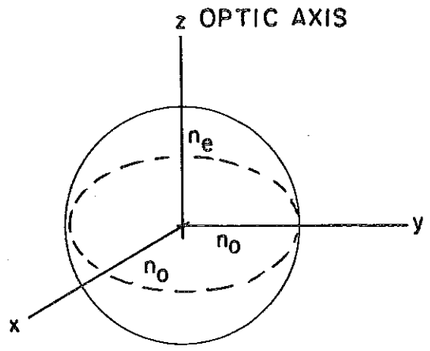

$n_e > n_o$ POSITIVE CRYSTAL
$n_o > n_e$ NEGATIVE CRYSTAL
(a)

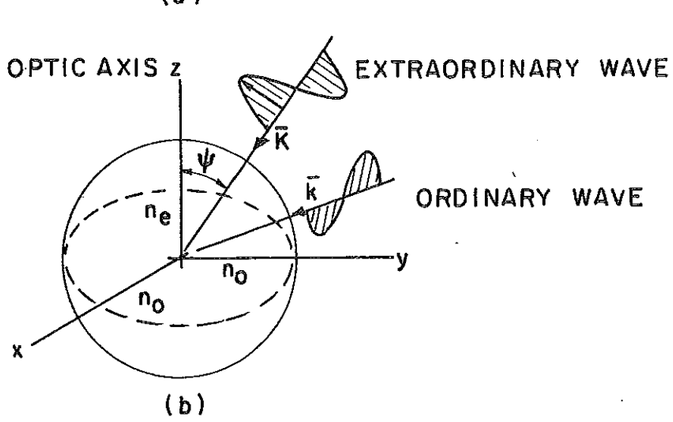

(b)

Fig. V-3. Refractive index indicatrix for uniaxial crystal.

The phase or wave normal velocity is given by $V_p = c/n$ where n is the refractive index of the wave and it is in a direction parallel to the wave vector $\bar{k}$. $\bar{V}_p$ is perpendicular to $\bar{D}$ and $\bar{H}$ of the light wave. The momentum density of light wave is given by $\bar{D} \times \bar{H}/4\pi c$ which is $\propto \hbar\vec{k}$. The ray velocity $\bar{V}_r$ is the velocity at which energy propagates and it is in the same direction as the Poynting vector $\bar{S} = c\bar{E} \times \bar{H}/4\pi$. The magnitude of $\bar{V}_r$ is $V_r = V_p/\cos\alpha$ where α is the angle between $\bar{E}$ and $\bar{D}$.[9] Since the dielectric constant $\underline{\underline{\epsilon}}$ is a tensor in an anisotropic crystal, $\bar{D}$ and $\bar{E}$ are not parallel to each other: $\bar{D} = \underline{\underline{\epsilon}}\,\bar{E}$. Therefore, $\bar{V}_r$ and $\bar{V}_p$ propagate at different velocities.

Born and Wolf[9] gives the relationship between the velocity of wave and the direction of propagation:

$$\frac{\hat{k}_x}{V_p^2 - V_x^2} + \frac{\hat{k}_y}{V_p^2 - V_y^2} + \frac{\hat{k}_z}{V_p^2 - V_z^2} = 0 \qquad (1)$$

where V_p is the phase velocity of wave traveling in the crystal, $\hat{k}_x$, $\hat{k}_y$ and $\hat{k}_z$ are unit vectors of the wave normal $\bar{k}$; V_x, V_y, and V_z are the principal phase velocities in the crystal along the x, y, and z crystal axis. For a uniaxial crystal with the optic axis in the z direction ($V_z = V_e$ and $V_x = V_y = V_o$) and for the wave normal propagating at angle φ to the optic axis, two roots are obtained from Eq. (1):[9]

$$V_p'^2 = V_o^2 \qquad (2)$$

$$V_p''^2 = V_o^2 \cos\varphi + V_e^2 \sin^2\varphi$$

Dividing these equations by ω^2 and using $V_o^2/\omega^2 = c^2/\omega^2 n_o^2$ and $V_e^2/\omega^2 = c^2/\omega^2 n_e$ one obtains:

$$1/(k_o)^2 = c^2/\omega^2 n_o^2 \qquad (3)$$

$$1/(k_e)^2 = (c^2/\omega^2 n_o^2)\cos^2\varphi + (c^2/\omega^2 n_e^2)\sin^2\varphi\,.$$

$\vec{k}_o(\varphi)$ and $\bar{k}_e(\varphi)$ are the ordinary and extraordinary wave vectors of the light propagating at angle φ to the optic axis (Fig. V-3b).

The angle relationship[10] between the wave normal $\vec{k}$ and Poynting vector S ($\vec{D}$ and $\vec{E}$ or $\vec{V}_p$ and $\vec{V}_r$) is given by:

$$\tan \alpha = (n_e^2 - n_o^2) \tan \varphi / (n_e^2 + n_o^2 \tan \varphi) \tag{4}$$

The relationship between $\vec{E}$, $\vec{D}$, $\vec{S}$, $\vec{k}$ and optic axis is shown in Fig. V-4. The refractive index of calcite are shown in Fig. V-5: Table I obtained from critical Tables[11] interpolated for the relevant wavelengths.

In the experiment the phonons are collinearly produced by the exciting laser (1.06 μ) via SRS. The wave vector of the phonons is given by

$$\vec{k}_p = \vec{k}_{1L} - \vec{k}_{1S} \tag{5a}$$

or

$$k_p = 2\pi \left(\frac{n_{o1L}}{\lambda_{1L}} - \frac{n_{o1S}}{\lambda_{1S}} \right) \tag{5b}$$

where $\vec{k}_{1L}$ and $\vec{k}_{1S}$ are the laser and Stokes wave vectors. The phonons are produced in a direction such that the probe beam (0.53 μ) can be phase-matched to the phonons:

$$\vec{k}'_{2S} = \vec{k}_{2L} - \vec{k}_p \tag{6a}$$

or

$$k'_{2S} = \sqrt{k_{2L}^2 + k_p^2 - 2k_{2L}k_p \cos \alpha_S} \tag{6b}$$

where α_S is the angle between the probe wave vector $\vec{k}_{2L}$ and the phonon wave vector $\vec{k}_p$ (which should be the ray direction of $\vec{k}_{2L}$), and $\vec{k}_{2S}$ is Stokes probe wave vector. Also, the probe ray direction is to travel collinearly with respect to the laser and phonons. The relevant angles of the laser and the probe beams are calculated using the following procedure: (1) the phonon wave constant k_p is calculated from Eq. (5b); (2) for a range of φ_2 (0 - 90°) for the probe beam $k_{2L}(\varphi_2)$ is calculated from Eq. (3). The probe ray direction, α_S, is obtained from Eq. (4) for which the ray and laser beam are collinear. (3) k'_{2S} is calculated from Eq. (6b) for

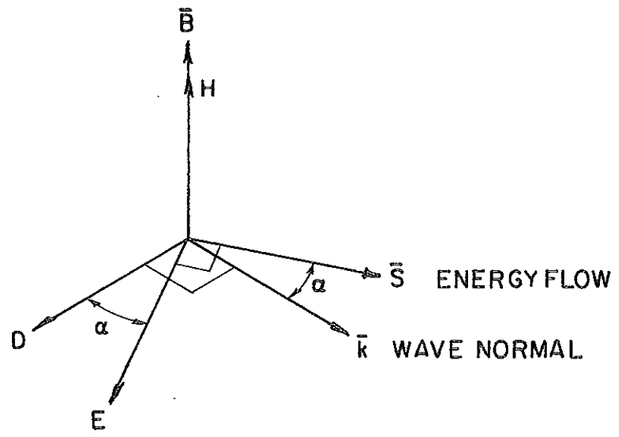

Fig. V-4. Direction of wave normal, of the field vectors and energy flow in an anisotropic crystal.

TABLE I

Light	Wavelength (μ)	n_o	n_e
Exciting Glass Laser ω_{1L}	1.06 μ	1.6426	-
Laser Stokes ω_{1S}	1.1978	1.6398	-
Probe ω_{2L}	0.5300	1.66312	1.4886
Probe Stokes ω_{2S}	0.5624	1.6604	1.4873
Probe Anti-Stokes ω_{2A}	0.5012	1.66605	1.4899

Fig. V-5. Table I: Ordinary and extraordinary refractive index of calcite (18°C) from critical tables.[11]

varies α_S and $k_2(\varphi_2)$. (4) From the angle, θ_S, between $\bar{k}_2$ and $\bar{k}'_{2S}$, φ_{2S} is obtained. (5) For varies φ_{2S}, k_{2S} is calculated from the refractive index data and from Eq. (3). (6) The mismatch $\Delta k = k'_{2S} - k_{2S}$ is calculated versus φ_2. The value of $\varphi_2 = \varphi_2^o$ is obtained when $\Delta k = 0$. (7) Then φ_2^o is recycled calculating α_S^o, $k_{2S}(\varphi_2^o)$, θ_S^o, φ_{2S}^o . (8) Using the angle that the optic axis makes with the surface normal B = 44° 45' and Snell's law, the angles of refraction incidence and transmission are obtained.[12]

Figure V-6: Table II contains a summary of the important parameters required for Stokes phase matching and collinear energy propagation. Figure V-7 shows propagation angles for the probe and exciting laser outside calcite and non-collinear phase-matching inside the calcite.

When dealing with the interaction between short pulses a most important consideration is the spatial overlap of the pulses throughout the crystal. The interaction legnth, ℓ_c, for the two pulses is defined to be the distance for which two pulse stay spatially coincident by less than half-pulse width. For two pulses of duration T_L having different group velocities V_{1g} and V_{2g}. The distance traveled in the material by the two pulses are $\ell_1 = V_{1g}t$ and $\ell_2 = V_{2g}t$. The distance between the pulses is $\ell_1 - \ell_2 = (V_{1g} - V_{2g})t = \Delta V_g t$. After a time $t = \ell_c/\bar{V}_g$ for which a pulse propagates a distance ℓ_c with the average group velocity $\bar{V}_g$, $\ell_1 - \ell_2 = \Delta V_g \ell_c/\bar{V}_g$. For two pulses displaced by half a pulse width: $\ell_1 - \ell_2 = \bar{V}_g T_L/2$. Therefore, $\ell_c = \bar{V}_g^2 T_L/2\Delta V_g$. The group velocity of a pulse is given by $V_g = c/n - (\lambda c/n^2)\, \partial n/\partial\lambda$, where n is refractive index and λ is wavelength. Figure V-8 (Table III) lists the group velocity calculated for $\Delta\lambda = 200$ Å and refractive index data for calcite[11] for the laser, probe, and Raman pulses. The interaction length for $T_L = 4$ psec for the exciting laser (1.06 μ) pulse and probe laser (0.53 μ) pulse is ~ 9.3 cm, and for the probe (0.53 μ) and probe Stokes (0.56 μ) pulses is ~ 11 cm. Therefore, the distance between the 1.06, 0.53 μ, and Raman pulses 0.56 μ remains constant through the sample.

The calcite samples used in the work is type B+ quality. The exit surface of the calcite is cut and polished parallel to (104) natural entrance face by J. Steiner of GTE Optics Shop. The length of calcite is 3 cm, and the aperture varied from crystal to crystal, typically 5 x 3 cm^2. The orientation of the optic axis was found by X-ray measurement by GTE X-Ray Group to be 44° 45' relative to the surface face normal.

TABLE II

$\varphi_2^o = 24° 37.5^1$

$\alpha_s^o = 5^o 9^1$

$\theta_s^o = 19.3^1$

$d(\Delta k)/d\varphi_2 = 22.2 \text{ cm}^{-1} \text{ deg}^{-1}$

$\varphi_{2S}^o = 24° 18.3^1$

$k_{1L} = 0.9736 \times 10^5 \text{ cm}^{-1}$

$k_p = 0.1135 \times 10^5 \text{ cm}^{-1}$

$k_{2L} = 0.1930 \times 10^6 \text{ cm}^{-1}$

$k_{2S} = 0.1817 \times 10^6 \text{ cm}^{-1}$

Fig. V-6. Table II: Useful parameters for phase-matched probe Stokes scattering.

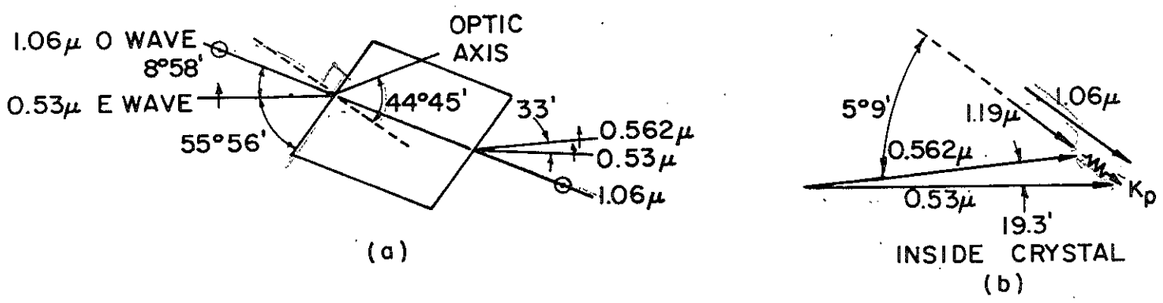

Fig. V-7. Angles for the probe and exciting laser beams (a) outside calcite, (b) noncollinear phase matching inside the calcite.

TABLE III

Light	Wavelength (μ)	Mode	Group Velocity (10^{10} cm/sec)
Laser	1.06	O-Wave	1.809
Probe	0.53	E-Wave ($\varphi = 24° 37'$)	1.816
Probe	0.53	E-Wave ($\varphi = 90°$)	1.982
Probe Raman Stokes	0.562	E-Wave ($\varphi = 90°$)	1.989

Fig. V-8. Table III: Group velocity for probe, laser, and Stokes Raman pulses.

The experimental arrangement is shown in Fig. V-9. The Nd-glass mode-locked laser is described[6] in Section II and emits about 50 pulses of $\sim 5 \times 10^9$ W peak power. A fraction of the beam is converted to second harmonic with a peak power of $\sim 2 \times 10^8$ W. The total bursts of radiation for the fundamental and harmonic are 6 and 4 psec, respectively, as measured by two-photon fluorescence.[13] A dielectric mirror (M_1) reflects 99.9% at 1.06 μm and transmits 90% at 0.53 μm. The 1.06-μm beam is collimated to 1 mm in diameter over the sample length of 3 cm and is polarized as an ordinary wave. The 0.53-μm beam is collimated to 4 mm in diameter and traverses the crystal as an extraordinary wave. Figure V-7 shows the experimental angles for Stokes phase matching of the probe beam to the phonons generated by the 1.06-μm beam and also having the ray direction (Poynting vector) of the probe beam collinear with the propagation direction of the phonons and 1.06-μm beams. These conditions can be satisfied in calcite because of its large birefringence. A variable time delay is introduced between the 1.06- and 0.53-μm beams by the movable prism P. The time of coincidence between the probe beam and the exciting beam is found by using the optical Kerr-effect gate[14] of a 1-cm sample of CS_2.[15] Cooled nitrogen gas is used to obtain a temperature of 100°K.

The condensing system for the 1.06-μm beam is carefully adjusted so that no crystal damage occurs. This adjustment is of critical importance to the success of the experiment. Occasionally the crystal is damaged, but when this occurs, the data for the entire run are rejected. Only one of six crystals we tried had a high damage threshold. This crystal — type B+ quality — is used for all the experimental data at room temperature. However, at low temperatures many crystals had high damage thresholds.

Self-focusing is observed in the calcite over the last 2 cm. SRS is observed at 1.19 μm with a conversion efficiency of $\geq 1\%$. The Raman pulse widths are estimated from transient Raman-gain equations[16] to be ≤ 2.7 psec. The Raman pulse widths could be shorter because approximately the first ten laser pulses of the train produce SRS,[17] and these pulses are the shortest pulses in time.[18] Therefore, the optical phonons are created in a time less than 2.7 psec. The 0.53-μm light scatters off the phonons and produces probe Stokes light at 0.562 μm with a conversion efficiency of $\cong 0.1\%$. The interaction length[19] calculated previously is $\gg$ than the sample length. Therefore, the distance between the pulses remain constant throughout the sample.

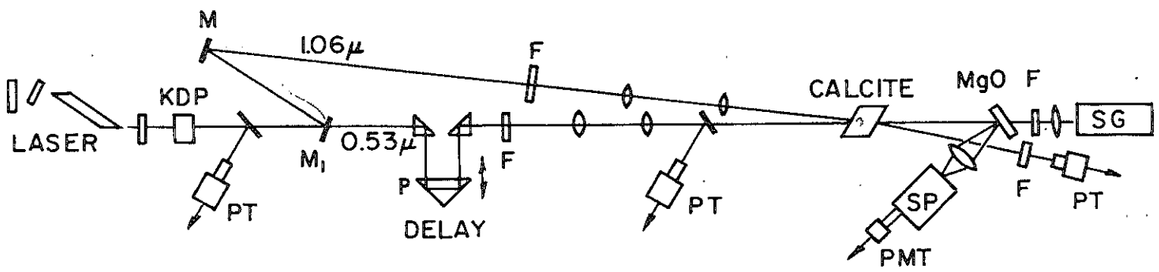

Fig. V-9. Experimental arrangement.

The presence of optical phonons is indicated by the Stokes Raman-scattered probe light at a wavelength of 0.562 μm which strikes an MgO plate and is imaged on the slit of a 1/2-m Jarrell-Ash spectrometer. The light is detected by an RCA 7265 photomultiplier. Typically 25 shots are taken at each delay position, and the intensity of the 0.562-μm light is normalized by dividing by the intensity of the 0.53-μm probe beam and 1.19-μm beam. Only about seven shots at each position are analyzed as a datum point — they are chosen on a basis of nearly the same laser intensity and "perfect" mode-locked train as displayed on a Tektronix 519 scope. A typical photograph of the detected signals is depicted in Fig. V-10. The 1.06-, 1.19-, 0.53-, and 0.562-μm beams are displayed coincidently on a Tektronix 555 scope. The intensity of the 0.562-μm light is found to be linear with respect to the 1.19-μm intensity. This is shown in Fig. V-11.

The following experimental procedures are used to insure that the Raman probe light arises from the created phonons: (1) At room temperature Raman spectra occur at 0.562 μm in a 100-cm^{-1} wide band and appear only when the 1.06-μm beam is present and coincident within ~40 psec with the 0.53-μm light beam. (2) The 0.562-μm light disappears when the 0.53-μm beam is not present. (3) The intensity of the 0.562-μm light depends critically on the orientation of the calcite crystal — the intensity decreases with a full width at half-maximum of 0.6° from the phase-matching angle at room temperature. Figure V-12 shows the variation in probe Raman scattering intensity with rotation of the crystal. (4) The 0.562-μm radiation is emitted from the calcite crystal an an angle of 28' from the propagation direction of the 5300-Å radiation which is in good agreement with calculation. Figure V-13 shows a photograph of the angular and wavelength dependence of the probe (0.53 μ) scattering off the phonons taken with and without the 1.06 μ beam present. Without the 1.06 μ - no phonons are created — no probe is observed. However, with the 1.06 μ producing SRS (phonons) a signal is observed at the probe Raman wavelength of 0.562 μ.

We have completed the discussion of the necessary experimental procedures and now proceed to the crux of this section — the optical-phonon lifetime which is obtained from the curve displayed in Fig. V-14 of the probe Stokes scattering energy vs delay time between the laser and probe beam. Figure V-14 shows the best individual runs. The profile of the tail of the curves in Fig. V-14 is exponential. It represents a convolution of the exponentially decaying phonon-density profile and the probe laser pulse. The lifetime is obtained from these tails for times much greater than the pulse width of the laser. The curves in Fig. V-14 are exponential for ten pulse widths of the probe beam. As long as the phonons decay exponentially,

TYPICAL PICTURE FOR CALCITE

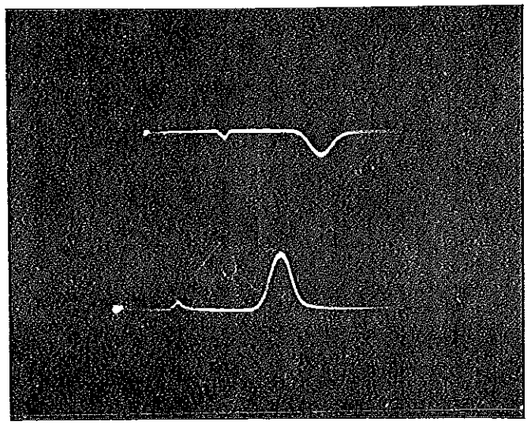

Fig. V-10. Signals detected and displayed coincident on 555 scope.

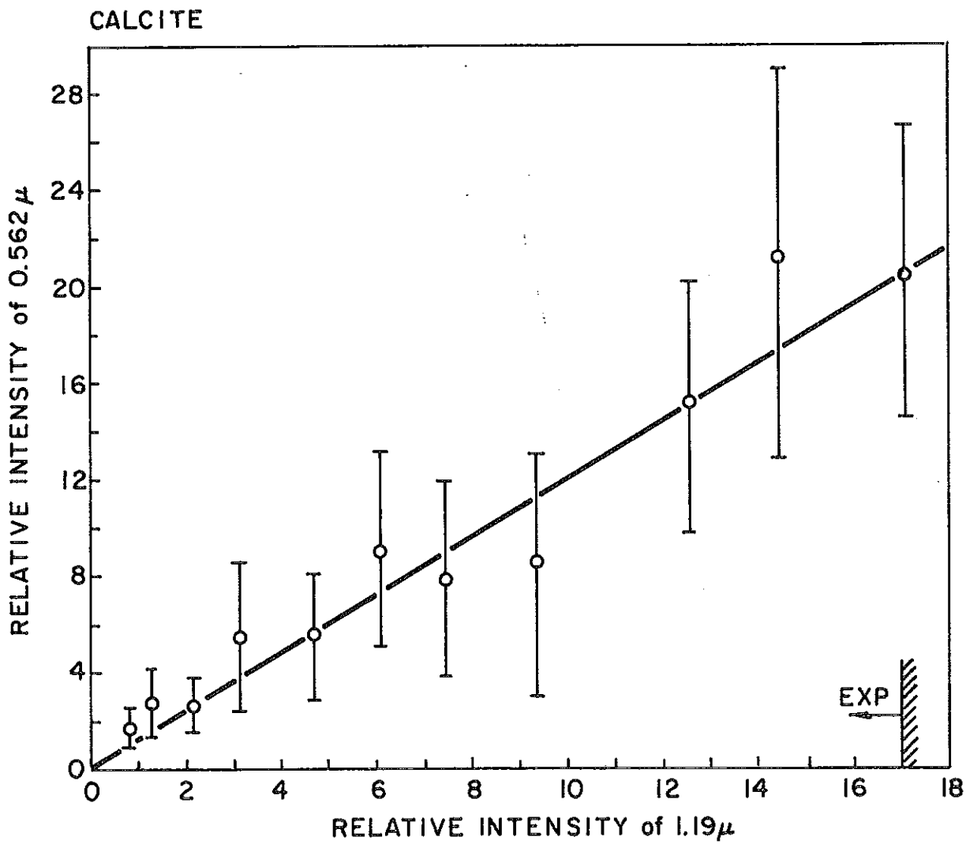

Fig. V-11. Probe Stokes scattering intensity versus stimulated Raman scattering intensity (number of phonon scattering versus number of phonon produced.

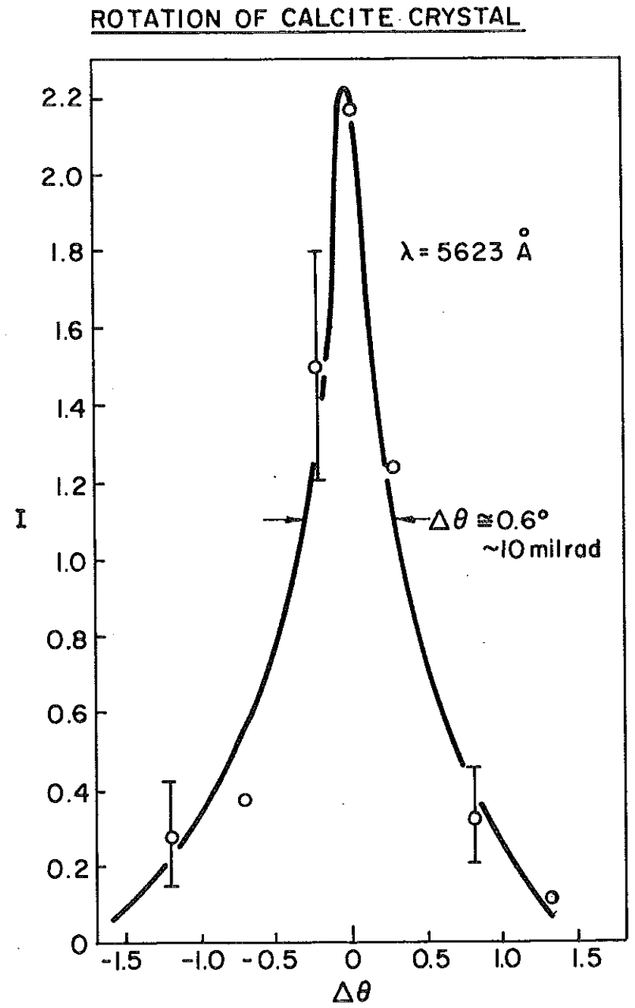

Fig. V-12. Effect of phase matching on probe scattering.

SCATTERING OFF CREATED PHONONS

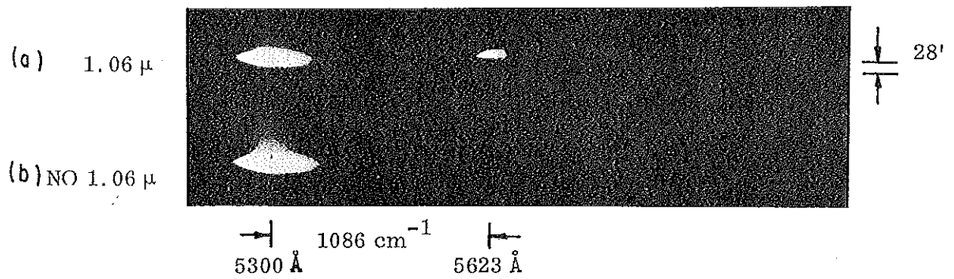

Fig. V-13. Probe Stokes Raman angular and wavelength dependence (a) 1.06 present (b) 1.06 absence. Probe: 5300 Å.

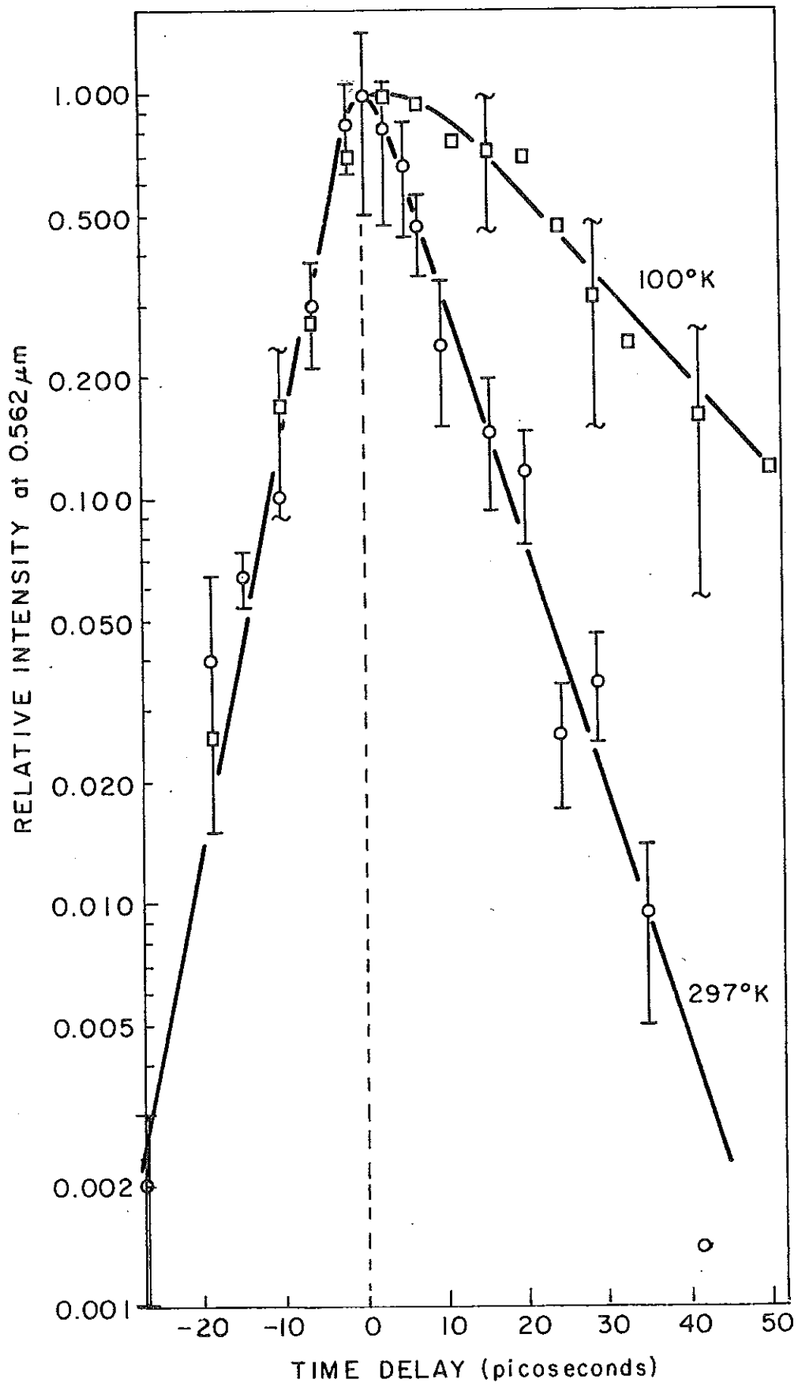

Fig. V-14. Normalized Stokes Raman-scattered probe intensity versus delay time between 1.06- and 0.53-μm beams at R. T. and 100°K.

convolution calculations (see theoretical section 4 for calculations) show that the shape of the tail[20] is not altered by the shape of the laser pulses.[21] The best fit to the experimental tail in Fig. V-14 is found for the decay rate of 19.1 ± 4 psec at 100°K and 8.5 ± 2 psec at 297°K. At 100°K the average lifetime measured for seven runs is 22 ± 4 psec.

A comparison will be made of the number of optical phonons created by SRS in this experiment to the thermal number. The number of optical phonons are calculated from the Stokes Raman conversion of ≥ 0.1% and from the incident power density of $\sim 10^{10}$ W/cm^2. The number of incident photon at 1.06 μ is 3×10^{18} photons/cm^3. Therefore, the number of optical phonon created by SRS is $N_p = 3 \times 10^{15}$ phonons/cm^3. The density of states excited in the experiment is calculated from $N_{STATES, \Delta k} = k^2 \Delta k \, \Delta\Omega/(2\pi)^3 = 5 \times 10^3$ States/cm^3 which is estimated from $k = 1.1 \times 10^4$ cm^{-1}, $\Delta k = 10^2$cm^{-1}, and $\Delta\Omega = 10^{-4}$ sr (laser beam solid angle). For comparison, the approximate total density of states in the branch is obtained from $N_{BRANCH} = 4\pi Q^3/3(2\pi)^3 = 10^{22}$ states/cm^3, where Q is the Brillouin wave number $\sim 10^8$ cm^{-1}. The number of created optical phonons per state is $n_p = N_p/N_{STATE, \Delta k} = 6 \times 10^{11}$ phonons/STATE. The thermal number of optical phonons/STATE is

$$n_T = \left[e^{\hbar\omega_p/k_BT} - 1\right]^{-1} = 3 \times 10^{-2} \text{ phonons/STATE}$$

at 300°K and the density of thermal phonons in Δk, $N_{pT} = n_T N_{STATES, \Delta k} = 1.5 \times 10^2$ phonons/cm^3. These phonon numbers indicate that the number of optical phonons created by SRS is significantly larger than the thermal phonon number in that state: $N_p/N_{pT} = 2 \times 10^{13}$.

Spontaneous Raman linewidth measurements[22] indicate a phonon lifetime at room temperature of ≅3.6 - 4.8 psec and a lifetime of ≅7.7 psec at 100°K. These results are not within our experimental error. The question arises, why should there be a disparity between the direct lifetime measurement and the spontaneous measurement? We offer two possible explanations for the difference. First, decay rates may differ for coherent phonons andthermal phonons.[23] The coherent phonons created by SRS have a state characterized by frequency $\omega_{p_2} = 1086$ cm^{-1} and wave number $k \cong 0.11 \times 10^5$ cm^{-1}, and within an angle of 10^{-2} rad. The population of coherent phonons in the same state (element of phase

space) is about 10^{13} times greater than the thermal background at room temperature and many times greater than 100°K.

The relative number of thermal phonons available to scatter with the created phonons is far less than for a thermal distribution of phonons in this state. If the decay mechanism involves interaction with thermal phonons, these coherent phonons will live longer in this state because the thermal phonon background cannot thermalize the large flux of coherent phonons. As evidence supporting this hypothesis, we note that not only is our measurement at room temperature in closer agreement with the decay time obtained from the spontaneous Raman linewidth near liquid-nitrogen temperature[22] (77°K), but also the measurement at 100°K is closer to the spontaneous linewidth measurement of 13.4 ± 4 psec at 4°K. Also, besides thermal saturation effects the decay rate of intense coherent phonons may be influenced by mutual interactions[24] (increasing the lifetime) and parametric-generation decay[25] processes (decreasing the lifetime).

A second explanation for the disparity between the lifetime measurements is that thermal and coherent phonons are located at different points on the optical-phonon branch and thus may have intrinsically different lifetimes.[26] Spontaneous Raman measurements at 90° to the incident beam of wavelength 6328 Å propagating along the c axis determine the linewidth for a phonon with momentum $k_p = 2.3 \times 10^5$ cm^{-1} whereas the direct technique detects a phonon of $k_p = 1.1 \times 10^4$ cm^{-1} propagating at a different angle in the crystal. Since the dispersion curve in calcite is incompletely known,[27] it is impossible to accurately calculate the decay rate for these two different phonons. However, a calculation is given in the next section on the relative values of the phonon lifetime at different $\bar{k}$ which supports the above statements.

In conclusion the first direct measurements of the optical-phonon lifetime show that the optical-phonon lifetime in calcite at both room temperature and at 100°K is considerably longer than that deduced previously from spontaneous measurements.

3. Theoretical Calculation of the Optical Phonon Lifetime

A. Introduction

An optical phonon distribution in a crystal interchanges energy with other lattice modes through collisions due to the anharmonicity of the lattice forces.[28]

The principal anharmonic interaction is due to the cubic anharmonicities[29] — resulting from the splitting of an optical phonon into two acoustic phonons of opposite momentum or by scattering of an optical phonon with acoustic or optical phonon to create another optical phonon. Calculations of the optical phonon lifetime have been reported by Cowley,[30] Klemens,[31] and Pines et al.[32] Their calculations are based on the same principles as the present treatment — but differs in that the most important object of this section is to get an expression for the variation of the lifetime $\tau(k)$ of an optical phonon of wave number $|\bar{k}|$ with respect to $\bar{k}$. With the idea to correlate the calculated lifetime at different $\bar{k}$ to the lifetime measured directly at $|\bar{k}| \sim 10^4$ cm^{-1} to that deduced from the spontaneous Raman linewidth at $|\bar{k}| \sim 10^5$ cm^{-1}. Herring[29] has calculated the dependence of τ on $|\bar{k}|$ for acoustic phonons via a three-phonon decay process and found $\tau^{-1} \propto k^n$ where $n = 1, 2, 3$, or 4 depending on the mode, on the branch point of an anisotropic dispersion curve, or on a different crystal class. Since the phonon dispersion curves in calcite are not known, only the functional dependence on k is obtained — not the exact lifetime values. Simple and isotropic dispersion relationships for the optical and acoustic branches are assumed.

B. General Formulation

Before considering particular phonon decay schemes consider an interaction Hamiltonian, H', which involves products of boson operators. The eigenfunctions $|n_{k1}\ n_{k2} \cdots n_{ki} \cdots\rangle$ of such a H' are represented by the number of phonons (boson) in each state, n_i. From the standard commutation properties the nonvanishing matrix elements[31, 33] are:

$$\langle n_{k1} \cdots n_{ki}-1 \cdots | \hat{A}_{ki} | n_{k1} \cdots n_{ki} \cdots \rangle = \left(\frac{\hbar}{M\omega_i}\right)^{1/2} \sqrt{n_{ki}}, \qquad (7)$$

$$\langle n_{k1} \cdots n_{ki}+1 \cdots | \hat{A}_{ki} | n_{k1} \cdots n_{ki} \cdots \rangle = \left(\frac{\hbar}{M\omega_i}\right)^{1/2} \sqrt{n_{ki}+1}.$$

Now consider the problem of calculating the relaxation time or lifetime of a given optical phonon via three phonon decay processes. From time-dependent perturbation theory[34] we find the transition probability per unit time, TP, that a system initially in some $|i\rangle = |n_{k1}\ n_{k2}\ n_{k3}\rangle$ makes a transition to another state $|f\rangle \equiv |n_{k1}'\ n_{k2}'\ n_{k3}'\rangle$ is:

$$TP = \frac{2\pi}{\hbar} |\langle f | H' | i \rangle|^2 \delta(\hbar\omega_f - \hbar\omega_i) \qquad (8)$$

where H' is the Hamiltonian responsible for the scattering between the states. Rather than considering transitions to well define discrete states, we may consider transitions to a group of states or a state which is broadened due to damping. In this case, the delta function in Eq. 8 may be replaced by line shape factor[33] or density of final states[34]: $\rho(\hbar\omega)$ depends on the particular problem.[35]

The interaction Hamiltonian due to three phonon (cubic anharmonicities) has been shown[28-33] to be

$$H' = \sum_{\ell,m,n} C_{\ell mn}\,\Delta(\bar{k}_\ell + \bar{k}_m + \bar{k}_n)\,\hat{A}_\ell\,\hat{A}_m^+\,\hat{A}_n^+ + c.c \qquad (9)$$

where $C_{\ell mn}$ is the coupling coefficient between the phonons, Δ is the Kronnecker delta function which vanishes unless $\bar{k}_\ell + \bar{k}_m + \bar{k}_n = 0$ or $\bar{b}$ (inverse lattice vector) — interference between the phonon waves. The value of the coupling coefficient in terms of Gruneiser constant[31] γ is

$$|C_{\ell mn}| = \frac{2M}{G3v}\,\gamma\,\omega_\ell\,\omega_m\,\omega_n \equiv A\,\omega_\ell\,\omega_m\,\omega_n \qquad (10)$$

where v is typically acoustic velocity, M is atomic mass, and G is the number of atoms in the crystal.

Following Sparks[33] calculation technique for magnon decay, we calculate the lifetime of a given optical phonon denoted by 1 has energy, ω_1, and momentum k_1 due to scattering and splitting processes. An example of the scattering of an optical phonon with a second phonon to form a third phonon is shown in Fig. V-15a. The splitting processes is depicted in Fig. V-15b. The splitting process dominates at low temperature while the scattering process dominates at high temperature because of large population of thermal phonon at high temperatures.

The matrix element for the scattering process of Fig. V-15a is:

$$\langle n_1\text{-}1,\ n_2\text{-}1,\ n_3\text{+}1 | C_{\ell mn}\hat{A}_\ell\hat{A}_\ell\hat{A}_n + C^*_{\ell mn}\,\hat{A}_\ell\,\hat{A}_m\,\hat{A}_n | n_1 n_2 n_3 \rangle. \qquad (11)$$

The only nonvanishing terms in the sum over ℓ, m, n are two terms:

$$\langle n_1\text{-}1, n_2\text{-}1, n_3\text{+}1 | C^*_{321}\,\hat{A}_1\,\hat{A}_2\,\hat{A}_3^+ + C^*_{312}\,\hat{A}_1\,\hat{A}_2\,\hat{A}_3^+ | n_1 n_2 n_3 \rangle$$
$$= \left(C^*_{321} + C^*_{312}\right)\left(n_1 n_2 (n_3\text{+}1)\,\frac{\hbar^3}{M^3\omega_1\omega_2\omega_3}\right)^{1/2}. \qquad (12)$$

(b)
PHONON DECAY

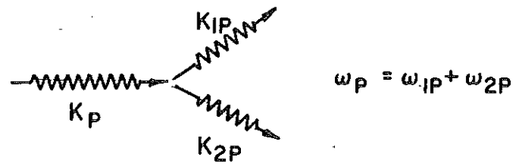

(a)
PHONON SCATTERING

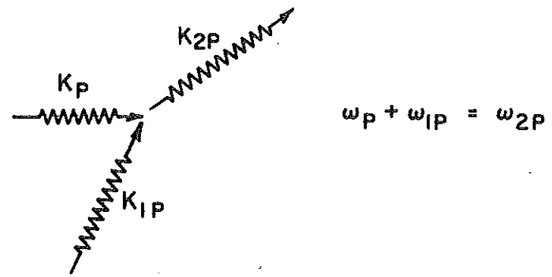

Fig. V-15. Three-phonon decay process: (a) scattering process, (b) splitting process.

The matrix element for the splitting process of Fig. V-15b is:

$$\langle n_1-1, n_2+1, n_3+1 \,|\, H' \,|\, n_1 n_2 n_3 \rangle = \left(C_{123} + C_{132}\right)\left(n_1 n_2 (n_3+1) \frac{\hbar^3}{(M^3 \omega_1 \omega_2 \omega_3)}\right)^{1/2}. \tag{13}$$

The rate of change of the occupation number[33] for the optical phonons; n_1, is given by:

$$\frac{dn_1}{dt} = \sum_{k_2, k_3} \left(\text{TP } (n_1 \text{ decrease by 1}) - \text{TP } (n_1 \text{ increase by 1})\right). \tag{14}$$

The rate of equation for n_1 for the scattering and splitting process[33] can be written as:

$$\frac{dn_1}{dt} = \frac{2\pi}{\hbar} \sum_{k_2 k_3} |C|^2 \, \Delta(\bar{k}) \, \frac{\delta(\omega)}{\hbar} \, (n) \, \frac{\hbar^3}{M^3 \omega_1 \omega_2 \omega_3}. \tag{15}$$

where, for the scattering process:

$$\begin{aligned} (n) &= (n_1 + 1)\,(n_2 + 1) n_3 - n_1 n_2\,(n_3+1) \\ (\bar{k}) &= \bar{k}_1 + \bar{k}_2 - \bar{k}_3 \\ (\omega) &= \omega_1 + \omega_2 - \omega_3 \\ |C|^2 &= |C_{321} + C_{312}|^2 , \end{aligned} \tag{16}$$

and for the splitting process:

$$\begin{aligned} (n) &= \frac{1}{2}\left[(n_1+1)(n_2)(n_3) - n_1 (n_2+1)(n_3+1)\right] \\ (\bar{k}) &= \bar{k}_1 - \bar{k}_2 - \bar{k}_3 \\ (\omega) &= \omega_1 - \omega_2 - \omega_3 \\ |C|^2 &= |C_{123} + C_{132}|^2. \end{aligned} \tag{17}$$

C. Relaxation Equation

The lifetime τ for n_1 optical phonons is defined by the relaxation equation:[33]

$$\frac{dn_1}{dt} = -\frac{1}{\tau_1}(n_1 - \bar{n}_1) \tag{18}$$

where $\bar{n}_1$ is the thermal-equilibrium value of n_1 phonons. In order to reduce Eq. (15) into the relaxation equation form (Eq. 18), it is necessary to make the assumption[33] that the occupation numbers of n_2 and n_3 phonons are maintained at its thermal equilibrium values $n_2 \cong \bar{n}_2$ and $n_3 \cong \bar{n}_3$ by subsequent relaxation processes:

(i) Scattering Lifetime

The relaxation equation is calculated for the scattering process. We calculate $\frac{d}{dt}(n_1-\bar{n}_1)$ by subtracting dn_1/dt and $\overline{dn}_1/dt$. From Eqs. 15 and 16

$$\frac{dn_1}{dt} = B\left[(n_1+1)\ (\bar{n}_2+1)\bar{n}_3 - n_1\ \bar{n}_2\ (\bar{n}_3+1)\right]$$

where B involves the Σ, and taking the average of dn_1/dt:

$$\frac{\overline{dn}_1}{dt} = B\left[(\bar{n}_1+1)\ (\bar{n}_2+1)\bar{n}_3 - \bar{n}_1\bar{n}_2(\bar{n}_3+1)\right] = 0. \tag{19}$$

This reduces to

$$\frac{dn_1}{dt} - \frac{d\bar{n}_1}{dt} = \frac{dn_1}{dt} = -B(n-\bar{n}_1)(\bar{n}_2-\bar{n}_3). \tag{20}$$

Substituting Eq. 20 into Eq. 18, the relaxation time is obtained:

$$\frac{1}{\tau_1}(\text{scattering}) = \frac{2\pi\hbar}{M^3}\sum_{k_2,k_3}\frac{|C|^2}{\omega_1\omega_2\omega_3}\Delta(\bar{k}_1+\bar{k}_2-\bar{k}_3)(\bar{n}_2-\bar{n}_3)\,\delta(\omega_1+\omega_2-\omega_3). \tag{21}$$

The thermal-equilibrium value of the occupation number of a phonon k_i having energy $\hbar\omega_{ki}$ is:

$$\bar{n}_{ki} = \left(e^{\hbar\omega_{ki}/k_B T} - 1\right)^{-1} \tag{22}$$

Substituting the thermal equilibrium $\bar{n}_{ki}$ into

$$\bar{n}_2 - \bar{n}_3 = e^{\hbar\omega_2/k_B T}\, \bar{n}_2\, \bar{n}_{1+2}/\bar{n}_1 \tag{23}$$

where $\bar{n}_1 = (e^{\hbar\omega_1/k_B T} - 1)^{-1}$, $\bar{n}_2 = (e^{\hbar\omega_2/k_B T} - 1)^{-1}$,

and $\bar{n}_{1+2} = (e^{\hbar(\omega_1+\omega_2)/k_B T} - 1)^{-1}$.

(ii) Splitting Lifetime

Now, the relaxation equation is calculated for the splitting process. We calculated $\frac{d}{dt}(n_1 - \bar{n}_1)$ using the above technique. From Eq. 15 and Eq. 17

$$\frac{dn_1}{dt} = \frac{d(n_1 - \bar{n}_1)}{dt} = -B\,\frac{1}{2}\,(n - \bar{n}_1)(\bar{n}_3 + \bar{n}_2 + 1). \tag{24}$$

Substituting the thermal equilibrium $\bar{n}_{ki}$ into

$$(\bar{n}_2 + \bar{n}_3 + 1) = \frac{\bar{n}_2\, n_{1-2}}{\bar{n}_1} \tag{25}$$

where $\bar{n}_{1-2} = (e^{\hbar(\omega_1 - \omega_2)/k_B T} - 1)^{-1}$.

Substituting Eq. 24 into Eq. 18, the relaxation time is obtained:

$$\frac{1}{\tau_1}\,(\text{splitting}) = \frac{2\pi\hbar}{M^3} \sum_{k_2, k_3} \frac{|C|^2}{\omega_1\omega_2\omega_3}\, \Delta\,(\bar{k}_1 - \bar{k}_2 - \bar{k}_3)(\bar{n}_2 + \bar{n}_3 + 1)\,\delta(\omega_1 - \omega_2 - \omega_3)\,. \tag{26}$$

The dependence on $\bar{k}_3$ may be eliminated by the conservation of momentum. The summation in Eqs. 21 and 26 is independent of $\bar{k}_3$ and the sum over $\bar{k}_3$ of the Kronecker delta gives unity.[33]

The lifetimes reduce to:

$$\frac{1}{\tau_1}\,(\text{scattering}) = \frac{2\pi\hbar}{M^3} \sum_{k_2} A^2\, \omega_1\, \omega_2\, \omega_3\, (\bar{n}_2 - \bar{n}_3)\, \delta\,(\omega_1 + \omega_2 - \omega_3),$$

and

$$\frac{1}{\tau_1}\,(\text{splitting}) = \frac{2\pi\hbar}{M^3}\sum_{k_2} A^2\,\omega_1\omega_2\omega_3\,(\bar{n}_2+\bar{n}_3+1)\,\delta\,(\omega_1-\omega_2-\omega_3) \qquad (28)$$

where $|C|^2 = A^2\,(\omega_1\omega_2\omega_3)^2$.

D. Different Phonon Decay Schemes

Using the lifetime given by Eqs. 27 and 28 calculations are made for different types of phonon decay schemes to obtain the functional dependence of τ_1 on $|k_1|$. The following four collinear schemes are examined: (1) splitting of an optical phonon into two acoustic phonons, (2) splitting of optical phonon into two optical phonons, (3) scattering of two optical phonons to give another optical phonon, and (4) scattering of an optical phonon with acoustic phonon to give another optical phonon.

Case (1): Optical → 2 Acoustic

We consider the decay of optical phonons at ω_1, k_1 into two acoustic phonons of ~ equal energy and opposite wave vector. This is shown in Fig. V-16. Substituting into Eq. 28 $\sum_{k_2} \rightarrow \int d^3k_2$ and

$$\delta(\omega_1-\omega_2-\omega_3) \rightarrow \frac{(\Gamma_1+\Gamma_2)/\pi}{(\omega_1-\omega_2-\omega_2)^2+(\Gamma_1+\Gamma_2)^2} \equiv \mathcal{L}\,, \qquad (29)$$

the convoluted density of final states (two-phonon, or combined density of states at ω_1)[31,,32] for the acoustic phonons where Γ are acoustic damping constant. Hence,

$$\frac{1}{\tau_1}(\text{splitting}) = \frac{2\pi\hbar\,A^2\omega_1}{M^3}\int_0^Q \frac{d^3k_2\,\omega_2\omega_3\,(\bar{n}_2+\bar{n}_3+1)}{(\omega_1-\omega_2-\omega_3)^2+(\Gamma_1+\Gamma_2)^2}\left(\frac{\Gamma_1+\Gamma_2}{\pi}\right). \qquad (29b)$$

Since the dispersion curves in calcite are not known, we assume a simple dispersion curve.[28] Here $\omega_1(k_1) = \omega_1 - \beta_1 k_1^2$ and $\omega_2 = Vk_2$. Expanding ω_2 in a Taylor series about k_{20} where $\omega_2 \cong 1/2\,\omega_1$ gives $\omega_2 \sim 1/2\,\omega_1 + \partial\omega_2/\partial k_2\,(k_2-k_{20})$. Also $\omega_2 \sim \omega_3$ and $\Gamma_1 = \Gamma_2 \equiv \Gamma_{AS}$. The boson factor $\bar{n}$ and Γ_{AS} are slowly varying with respect to k and may be pulled outside the integral (Eq. 29b) and evaluated at $\omega_1/2$. The angular variations are ignored in this isotropic case . Therefore, Eq. 29 becomes

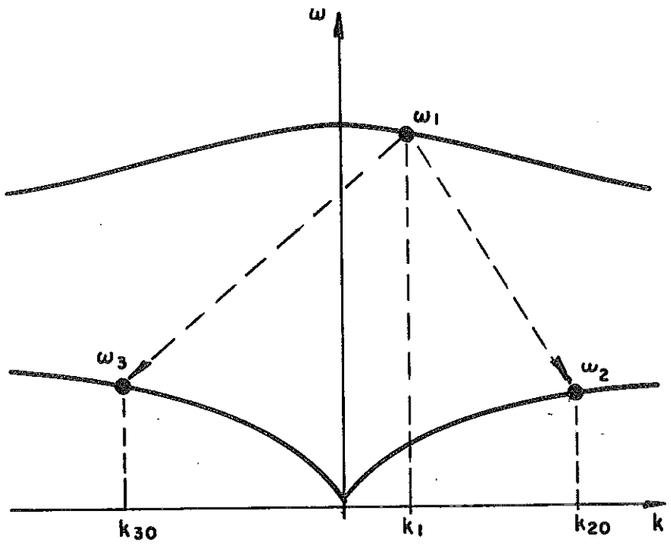

Fig. V-16. Phonon dispersion curve showing the decay of optical phonon splitting into two acoustic phonons.

$$\frac{1}{\tau_1}(\text{Splitting}) = A'\omega_1 \int_0^Q \frac{d^2k_2 (Vk_2)^2}{\left[(\omega_1 - \beta_1 k_1^2) - 2(1/2\,\omega_1 - \frac{\partial\omega_2}{\partial k_2}(k_2 - k_{20}))\right]^2 + 4\Gamma_{AS}^2}$$

where

$$A' = \frac{2\pi\hbar A^2}{M^3}(2\bar{n}_2 + 1) \tag{30}$$

which reduces to

$$= \frac{A' 4\pi V^2 \omega_1}{\left(\frac{\partial\omega_2}{\partial k_2}\right)^2} \int_0^Q \frac{k_2^4\, dk_2}{\left[k_2 - k_{20} - \frac{\beta k_1^2}{\left(\frac{\partial\omega_2}{\partial k_2}\right)}\right]^2 + \frac{4\Gamma_{AS}^2}{\left(\frac{\partial\omega_2}{\partial k_2}\right)^2}} .$$

Setting

$$k_o \equiv k_{20} + \frac{\beta k_1^2}{\left(\frac{\partial\omega_2}{\partial k_2}\right)} \quad \text{and} \quad a^2 \equiv \frac{4\Gamma_{AS}^2}{\left(\frac{\partial\omega_2}{\partial k_2}\right)^2}$$

and substituting into Eq. (30):

$$\frac{1}{\tau_1}(\text{Splitting}) \frac{A' 4\pi V^2 \omega_1}{\left(\frac{\partial\omega_2}{\partial k_2}\right)^2} \int_0^Q \frac{k_2^4\, dk_2}{(k_2 - k_o)^2 + a^2} . \tag{31}$$

Here Q is the Brillouin zone edge wave vector. The decay to acoustic phonons occurs near critical points where $\partial\omega_2/\partial k_2 \sim 0$. A plot of τ versus $|\bar{k}_1|$ is shown in Fig. V-17 for the following parameters :[28, 35, 36] $\beta = 1$ cm^2/sec, $\Gamma_{AS} = 10^7$ sec^{-1}, and $Q = 10^8$ cm^{-1}; (a) $\partial\omega_2/\partial k_2 = 10^2$ cm/sec; (b) $\partial\omega_2/\partial k_2 = 3 \times 10^2$ cm/sec. The lifetime decreases with wave vector for $k_1 > 10^4$cm^{-1}.

Case 2: Optical → Optical + Optical

We consider the decay of an optical phonon at k_1 decaying into two optical phonons of ~ equal energy and opposite momentum . This is shown in Fig. V-18.

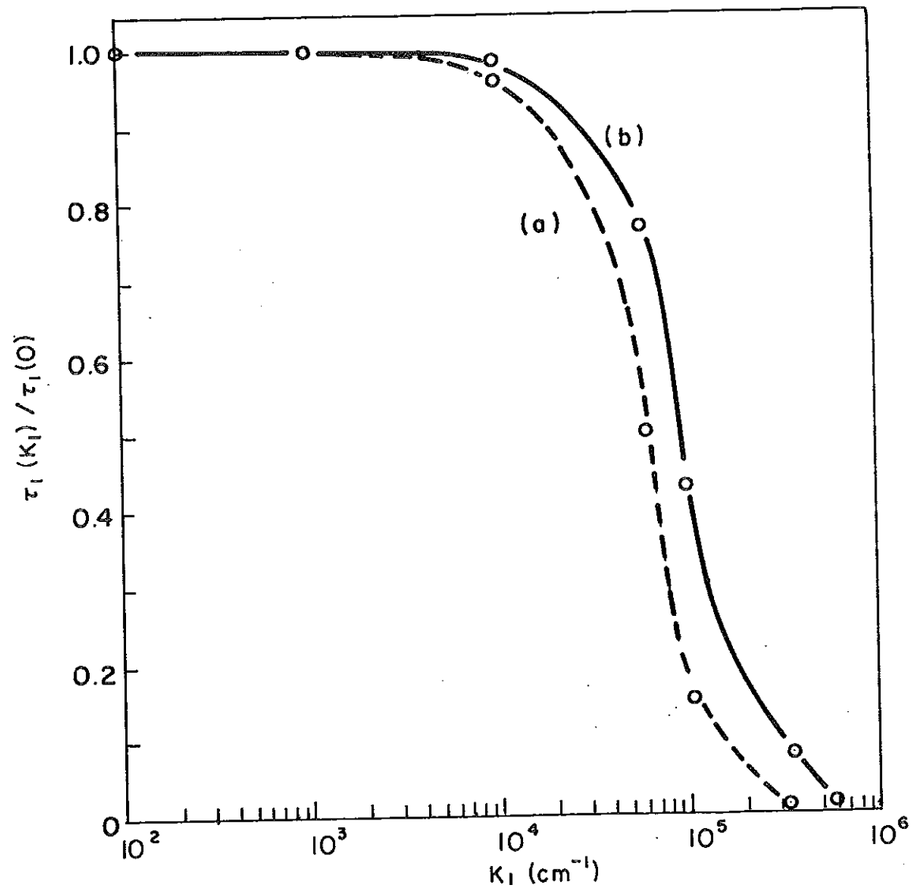

Fig. V-17. Optical phonon lifetime, τ, as function of its momentum, k_1, for the splitting process (op → 2 as): $\beta = 1\,cm^2/sec$, $\Gamma_{AS} = 10^7\ sec^{-1}$, $Q = 10^8\ cm^{-1}$; (a) $\partial\omega_2/\partial k_2 = 10^2$ cm/sec; (b) $\partial\omega_2/\partial k_2 = 3 \times 10^2$ cm/sec.

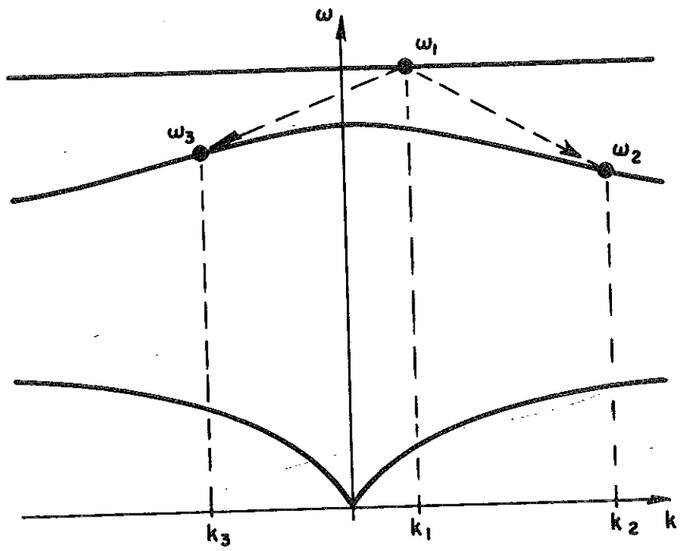

Fig. V-18. Phonon dispersion curve showing the decay of optical phonon splitting into two optical phonons.

Substituting into Eq. (28), $\sum_{k_2} \rightarrow \int d^3k_2$, $\omega_1(k_1) \cong \omega_1 - \beta_1 k_1^2$, $\omega_2(k_2) = \omega_2 - \beta_2 k_2^2$, and $\omega_2(k) = \omega_3(k)$ we obtain:

$$\frac{1}{\tau_1}(\text{Splitting}) = \frac{2\pi\hbar A^2\omega_1}{M^3} \int_0^Q d^3k_2\, \omega_2(k)\, \omega_3(k)\, (\bar{n}_2 + \bar{n}_3 + 1)\, \delta(\omega_1 - \omega_2 - \omega_3). \tag{32}$$

Neglecting the dispersion of ω_2 and ω_3 in the numerator gives:

$$\frac{1}{\tau_1}(\text{Splitting}) = \frac{2\pi\hbar A^2\omega_1\omega_2^2}{M^3} (\bar{n}_2 + \bar{n}_3 + 1) \int_0^Q 4\pi k_2^2\, dk_2\, \delta(2\beta_2 k_2^2 - \beta_1 k_1^2). \tag{33}$$

Setting $k^2 \equiv 2\beta_2 k_2^2$ and $k_o^2 \equiv \beta_1 k_1^2$, Eq. (33) becomes

$$\frac{1}{\tau_1}(\text{Splitting}) = A_o \omega_1 \omega_2^2 \int_0^{Q\sqrt{2\beta_2}} k^2 dk\, \delta(k^2 - k_o^2), \tag{34}$$

where

$$A_o = \frac{2\pi k A^2 (2\bar{n}_2 + 1)}{M^3 (2\beta_2)^{3/2}}.$$

It is not necessary to replace the delta function by the density of state since the delta function is a fair approximation for the shape function.[28, 33] From Sparks[33]

$$\delta(k^2 - k_o^2) = \frac{\delta(k + k_o) + \delta(k - k_o)}{|k_o|} \tag{35}$$

Substituting Eq. (35) into Eq. (32) gives

$$\frac{1}{\tau_1}(\text{Splitting}) = A_o\, \omega_1 \omega_2^2 \int_0^{\sqrt{2\beta_2}Q} k^2 dk \left[\frac{\delta(k + k_o) + \delta(k - k_o)}{|k_o|}\right] \tag{36}$$

Integrating Eq. (36) gives

$$\frac{1}{\tau_1(\text{Splitting})} = \frac{A_o \omega_1 \omega_2^2 k_o^2}{|k_o|} = A_o \omega_1 \omega_2^2 k_o . \tag{37}$$

Substituting $k_o = \sqrt{\beta_1} k_1$ into Eq. (37) gives

$$\tau_1(\text{Splitting}) = \frac{1}{A_o \omega_1 \omega_2^2 \sqrt{\beta_1} k_1} \tag{38}$$

for $k_1 \ll Q$. Therefore, the lifetime of the decrease is k_1 via splitting into two optical phonons.

Case 3: Optical + Optical → Optical

A similar functional dependence given by Eq. (32) occurs for the scattering of optical phonon (ω_1, k_1) with a thermal optical phonon (ω_2, k_2) to create another optical phonon (ω_3, k_3).

Case 4: Optical + Acoustic → Optical

Now consider the scattering of optical phonon with thermal acoustic phonon to generate another optical phonon. This process is depicted in Fig. V-19. Here $\omega_1(k_1) = \omega_1 - \beta_1 k_1^2$, $\omega_3(k) \cong \omega_3 - \beta_3 k_3^2 \cong \omega_3$, and $\omega_2 = Vk_2$ - expanding ω_2 in Taylor series about k_{20} where $\omega_2 = \omega_3 - \omega_1$: $\omega_2 = \omega_3 - \omega_1 + \frac{\partial \omega_2}{\partial k_2}(k_2 - k_{20})$. Substituting into Eq. (27), $\sum_{k_2} \rightarrow \int d^3k_2$ and a convoluted spectral density of optical phonon and acoustic phonons:

$$\delta(\omega_1 + \omega_2 - \omega_3) \rightarrow \underset{\text{optical}}{\delta} \otimes \underset{\text{acoustic}}{\mathfrak{L}} = \mathfrak{L}_{\text{acoustic}} , \tag{39}$$

Eq. (27) becomes

$$\frac{1}{\tau_1(\text{Scattering})} = \frac{2\pi\hbar A^2 \omega_1 (\bar{n}_2 - \bar{n}_3)}{M^3} \int_o^Q \frac{d^3k_2 (Vk_2)\, \omega_3}{\left[(\omega_1 - \beta_1 k_1^2) + (\omega_3 - \omega_1) + \frac{\partial \omega_2}{\partial k_2}(k_2 - k_{20})\right]^2 + \Gamma_{AS}^2} . \tag{40}$$

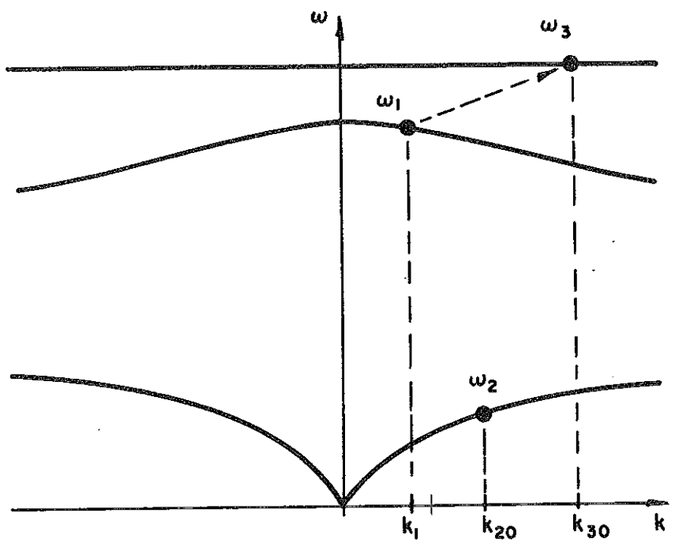

Fig. V-19. Phonon dispersion curve showing the scattering of the optical phonon with an acoustic phonon to give another optical phonon.

This equation reduces to

$$\frac{1}{\tau_1}(\text{Scattering}) = \frac{A_1 \omega_1 \omega_3 4\pi V}{\left(\frac{\partial \omega_2}{\partial k_2}\right)^2} \int_o^Q \frac{k_2^3 \, dk_2}{\left[k_2 - k_o\right]^2 + \alpha^2} \tag{41}$$

where

$$k_o \equiv k_{20} + \frac{\beta_1 k_1^2}{\left(\frac{\partial \omega_2}{\partial k_2}\right)^2}, \quad \alpha^2 \equiv \frac{\Gamma_{AS}^2}{\left(\frac{\partial \omega_2}{\partial k_2}\right)^2},$$

and $A_1 = \frac{2\pi\hbar A^2}{M^3}(\bar{n}_2 - \bar{n}_3)$. A plot of τ versus k_1 from Eq. (41) is shown in Fig. V-20 for parameters: $\beta = 1$ cm^2/sec, $\Gamma_{AS} = 10^7$ sec^{-1}, $Q = 10^8$ cm^{-1}; (a) $\partial\omega_2/\partial k_2 = 10^2$ cm/sec; (b) $\partial\omega_2/\partial k_2 = 3 \times 10^2$ cm/sec. The lifetime decrease with k_1.

E. Conclusion

The lifetime of optical phonon: $\tau_1(k_1)$ is sum over all the possible decay schemes:

$$\frac{1}{\tau_1(k_1)} = \sum_{i=1}^{n} \frac{1}{\tau_1(k_1)_i} = \sum_{j=o} b_j k_1^j \tag{42}$$

where n = number of different types of decay process. It has been qualitatively estimated that the optical phonon lifetime is constant for small k ($< 10^3$ cm^{-1}) and decreases for large k ($> 10^3$ cm^{-1}). Therefore, it is not unreasonable that this may account for the difference between the lifetime measured directly ($k_1 \sim 10^4$ cm^{-1}) and the lifetime deduced from linewidth ($k_1 \sim 10^5$ cm^{-1}) — the calculated ratio is $\tau_1(10^4 \text{ cm}^{-1})/\tau_1(10^5 \text{cm}^{-1}) \sim 2$ to 10, depending on decay process.

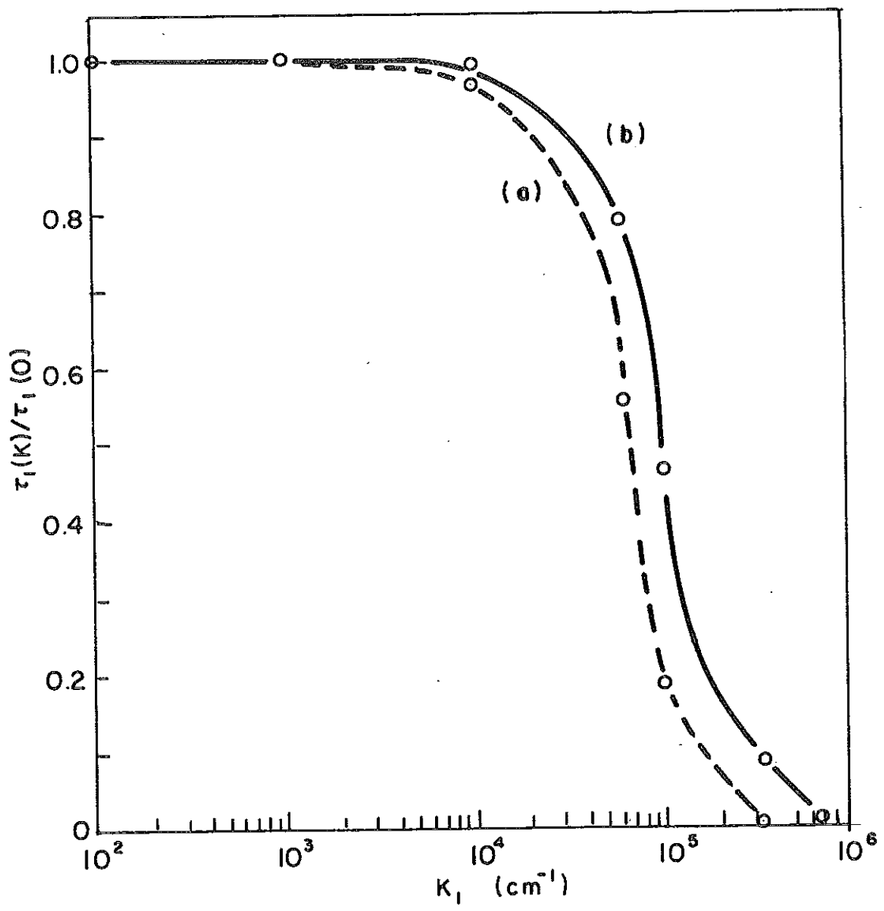

Fig. V-20. Optical phonon lifetime as function of its momentum for the scattering process: (op + as → op): $\beta = 1\ cm^2/sec$, $\Gamma_{AS} = 10^7\ sec^{-1}$, $Q = 10^8\ cm^{-1}$, (a) $\partial\omega_2/\partial k_2 = 10^2$ cm/sec; (b) $\partial\omega_2/\partial k_2 \cong 3x10^2$cm/sec.

4. Theory of Transient Probe Raman Scattering

A. Introduction

In this section, the coupled wave equations[37] are derived describing: (1) the generation of the optical phonons by stimulated Raman scattering (SRS) caused by an intense ultrashort laser pulse, and (2) the Raman scattering of these phonons by a weaker ultrashort probe laser pulse as a function of delay time between the laser beams — (probe Raman intensity profile). The solution of these coupled equation for the probe Raman intensity profile is shown to depend on the time convolution of the probe laser and phonon distribution. Since the exact shape of the laser is not known,[38] a series of convolution calculations are given for different laser pulse shapes and pulse widths. These calculations allow an error to be estimated for the experimental extracted phonon lifetimes. Finally, a comparison is made between the experimental observed probe Raman intensity profile and a theoretical calculated profile for exponential laser pulses.

B. Coupled Wave Equations

The theory of transient stimulated Raman scattering (SRS) has been developed by ultrashort laser pulses by Carman et al.[39] Theoretical equations governing the growth and decay of the optical phonon distribution has also been discussed previously.[39, 40] Giordmaine[40] theoretically calculated and experimentally demonstrated probe scattering from phonons with a Q-switched ruby laser pulse of 30 nsec duration. The main contribution to the theory of probe scattering in this thesis is to calculate[41] the Raman probe intensity at various delay times using ultrashort laser pulses ($\sim 10^{-12}$ sec).

The equation of motion for the lattice can be derived from the Lagrangian density of the system:[42]

$$L = L_{\text{RADIATION}} + L_{\substack{\text{OPTICAL} \\ \text{PHONON}}} + L_{\text{INTERACTION}} \tag{43}$$

The Lagrangian density for the radiation field[42] is

$$L_{\text{RADIATION}} = \frac{1}{2}(E^2 - B^2), \tag{44}$$

and for the optical phonons[42] (no dispersion $V_g \cong 0$) is

$$L_{\substack{\text{OPTICAL}\\\text{PHONONS}}} = \frac{1}{2}\,\dot{Q}^2 - \frac{1}{2}\,\omega_p^2\,Q^2, \tag{45}$$

where Q is the normal coordinate, ω_p is the phonon angular frequency. The interaction Lagrangian[42] is

$$L_{\text{INTERACTION}} = N\,\underline{\underline{\alpha}}\,\vec{E}\,\vec{E}, \tag{46}$$

where N is number density of the lattice ions and $\underline{\underline{\alpha}} = \underline{\underline{\alpha}}_o + \left(\frac{\partial \underline{\underline{\alpha}}}{\partial Q}\right)_o \vec{Q}$ is the polarizability tensor. In tensor notation, $(\alpha)_{ij} = (\alpha_o)_{ij} + \left(\frac{\partial \alpha}{\partial Q}\right)_{ij} Q \equiv (\alpha_o)_{ij} + \alpha'_{ij}\,Q$. Q is the amplitude of stimulated normal vibrational mode, $(\alpha_o)_{ij}$ is normal polarizability of an equilibrium lattice, and $\alpha'_{ij} \equiv N\left(\frac{\partial \alpha}{\partial Q}\right)_{ij}$ is Raman scattering tensor.

The equation of motion for the optical phonons is obtained from the Lagrangian density equation:[43]

$$\frac{\partial L}{\partial Q} - \frac{\partial}{\partial x^i}\left(\frac{\partial L}{\partial\left(\frac{\partial Q}{\partial x^i}\right)}\right) - \frac{\partial}{\partial t}\left(\frac{\partial L}{\partial\left(\frac{\partial Q}{\partial t}\right)}\right) = 0. \tag{47}$$

where $x^i = x, y, z$.

The equation of motion becomes

$$\ddot{Q} + \omega_p^2\,Q + 2\Gamma\dot{Q} = \alpha'_{ij}\,E^i E^j, \tag{48}$$

where the phonon damping term $2\Gamma\dot{Q}$ is added phenomenologically.[42]

The form of the fields are expressed in terms of complex amplitudes:

$$\begin{aligned} E_L &= \mathcal{E}_L\, e^{i(k_L z - \omega_L t)} \\ E_S &= \mathcal{E}_S\, e^{i(k_S z - \omega_S t)} \\ Q &= q\, e^{i(k_p z - \omega_p t)} \end{aligned} \tag{49}$$

Substituting Eq. 49 into Eq. 48 and considering terms oscillating at ω_p, the equation of motion for the vibrational amplitude q reduces to

$$\dot{q} + \Gamma q = \frac{a'}{2i\omega_p} \mathcal{E}_L \mathcal{E}_S^* e^{i(k_L - k_S - k_p)z} . \tag{50}$$

In SRS, the maximum gain occurs when $k_L - k_s - k_p = 0$ (phase matching). Taking the complex conjugate of Eq 50 ($\Delta k = 0$)

$$\dot{q}^* + \Gamma q^* = i \kappa_1 \mathcal{E}_L^* \mathcal{E}_S, \tag{51}$$

where $\kappa_1 \equiv \frac{a'}{2\omega_p}$. It is assumed that the Stokes and laser pulses propagate at the same group velocities.

Now, the equation for Stokes generation is derived for propagation in an isotropic material. The relevant Maxwell equations are:

$$\begin{aligned} \nabla \cdot \vec{D} &= \rho \\ \nabla \times \vec{H} &= \frac{4\pi \vec{J}}{c} + \frac{1}{c} \frac{\partial \vec{D}}{\partial t} \\ \nabla \times \vec{E} &= -\frac{1}{c} \frac{\partial \vec{B}}{\partial t}, \end{aligned} \tag{52}$$

and the constitutive relation:

$$\vec{D} = \epsilon \vec{E} + P^{NL} \tag{53}$$

where ϵ is the linear dielectric constant and P^{NL} is the nonlinear part of the polarization, P. The wave equation for $\mu = 1$, $J = 0$, and $\rho = 0$ becomes

$$\nabla^2 \vec{E} = \frac{\epsilon}{c^2} \frac{\partial^2 \vec{E}}{\partial t^2} + \frac{4\pi}{c^2} \frac{\partial^2 P^{NL}}{\partial t^2}. \tag{54}$$

The equation governing the Stokes wave generation and propagation is obtained from the terms oscillating at ω_s in Eq. 54 . For small gain, the linearized (neglecting second derivatives) Stokes equation is:

$$2ik_s \frac{\partial \mathcal{E}_s}{\partial z} + 2i \frac{\omega_s \epsilon}{c^2} \frac{\partial \mathcal{E}_s}{\partial t} = \frac{\partial^2 \mathcal{P}_s^{NL}}{\partial t^2} . \tag{55}$$

The polarization of material is given by $\vec{P} = \underline{\underline{a}} \vec{E}$ where $\vec{E} = \vec{E}_L + \vec{E}_S + \vec{E}_A$ and $\underline{\underline{a}} = \underline{\underline{a}}_o + \underline{\underline{a}}' \underline{Q}$.

Therefore, the polarization oscillating at ω_s is

$$\mathcal{P}_S = a_o \mathcal{E}_S + \underbrace{a' q^* \mathcal{E}_L}_{\mathcal{P}_S^{NL}} \tag{56}$$

Hence, substituting Eq. (56) into Eq. (55), the linearized wave equation for the Stokes wave is

$$\frac{\partial \mathcal{E}_S}{\partial z} + \frac{1}{V_s} \frac{\partial \mathcal{E}_S}{\partial t} = \frac{i 4\pi \omega_s^2}{2k_s c^2} a' q^* \mathcal{E}_L , \tag{57}$$

where $V_s = c/n_s$ is the phase velocity of the Stokes wave.

Making a change of variables: [39]

$$t' \equiv t - z/v_s, \tag{58}$$

$$z' \equiv z.$$

The linearized wave equation for Stokes wave (Eq. 57) becomes

$$\frac{\partial \mathcal{E}_S}{\partial z'} = i \frac{4\pi \omega_s^2 a'}{2k_s c^2} q^* \mathcal{E}_L, \tag{59}$$

or

$$\frac{\partial \mathcal{E}_S}{\partial z'} = i \kappa_2 q^* \mathcal{E}_L$$

where the coupling constant

$$\kappa_2 \equiv 4\pi \omega_s^2 a' / 2 k_s c^2.$$

In the probe scattering experiment, an intense laser $\mathcal{E}_{1L}(t')$ produces a phonon population $q^*(t')$ at a time t'; then, a second weak probe laser $\mathcal{E}_{2L}(t'+\tau_D)$ enters the material after a time $t' + \tau_D$ and scatters off the decaying phonon population. The driving term for the phonon amplitude is given by Eq. (51).

$$\mathcal{E}_L^* \mathcal{E}_S = \mathcal{E}_{1S}(t') \mathcal{E}_{1L}^*(t') \underbrace{+ \mathcal{E}_{2S}(t'+\tau_D) \mathcal{E}_{2L}^*(t'+\tau_D)}_{\text{small}} \cong \mathcal{E}_{1S}(t') \mathcal{E}_{1L}^*(t') \tag{60}$$

The phonon amplitude equation of motion has the same form:

$$\dot{q}^* + \Gamma q^* = -i\kappa_i \, \mathcal{E}_{1S}(t') \, \mathcal{E}^*_{1L}(t') \tag{61}$$

However, the probe Stokes wave resulting from the scattering of $\mathcal{E}_{2L}(t'+\tau_D)$ off $q^*(t')$ is governed by

$$\frac{\partial \mathcal{E}_{2S}}{\partial z'} \, e^{ik_{2s}z} = i\kappa_2 \, q^*(t') \, e^{-ik_p z} \, \mathcal{E}_2(t'+\tau_D) \, e^{ik_{2L}z} \tag{62}$$

where we have included in Eq. (59) the possible phase mismatch among q^*, $\mathcal{E}_{2L}$ and $\mathcal{E}_{2S}$ (the phonon's wave vector is $k_p = k_{1L} - k_{1S}$). Therefore, Eq. (62) reduces to:

$$\frac{\partial \mathcal{E}_{2S}}{\partial z'} = i\kappa_2 \, q(t') \, \mathcal{E}_{2L}(t'+\tau_D) \, e^{-i\Delta k \cdot z} \tag{63}$$

where $\Delta k = k_{2L} - k_p - k_{2S} = k_{2L} - (k_{1L} - k_{1S}) - k_{2S}$.

The integral of Eq. (63) over sample length ℓ is

$$\mathcal{E}_{2S} = i\kappa_2 \, q^*(t') \, \mathcal{E}_2(t'+\tau_D) \, \ell \, e^{i\Delta k \ell/2} \, \frac{\sin(\Delta k \ell/2)}{(\Delta k \ell/2)} \, . \tag{64}$$

The total probe Stokes energy scattered at time τ_D which is observed experimentally is given by:

$$I_{2S}(\tau_D) = \frac{cn_{2S}}{4\pi} \int |\mathcal{E}_{2S}|^2 \, dt'$$

$$= \frac{cn_{2S}}{4\pi} \, \kappa_2^2 \left(\frac{\sin \Delta k \ell/2}{\Delta k \ell/2}\right)^2 \ell^2 \int |q(t')|^2 \, |\mathcal{E}_{2L}(t'+\tau_D)|^2 \, dt' \tag{65}$$

Therefore, the scattered energy depends on the convolution of the phonon and laser profiles. For the probe Stokes scattering in calcite, the probe Stokes scattered energy has the same form except the coupling constant $\kappa_2 \to \kappa'_2$ where

$$\kappa'_2 \equiv \frac{4\pi\omega_{2s}^2 \, \underline{\underline{\alpha}}' : \hat{e}_{2L} \hat{e}_{2S}}{2k_{2s}c^2 \cos\alpha_S} \tag{66}$$

where α_S is angle between ray and wave direction for Stokes wave, and $\hat{e}$ is the polarization direction. For a derivation of equation 65 and 66 for anisotropic crystal (calcite) see reference 44.

C. Convolution Calculations

The probe Raman scattered energy has been shown in Section B to depend on the convolution of the phonons and probe laser intensity profile $\sim \int q^2(t') \mathcal{E}_{2L}^2(t'+\tau_D)\, dt'$. Since the laser pulse shape is not exactly known, convolutions for different laser pulse shapes are calculated to determine the error by which the phonon lifetime can be extracted from the tail of the probe scattered profile. Various laser pulse shapes that are convoluted[45] with an exponential phonon profile ($e^{-t/T_1}\,\mu(t)$) are a Gaussian; $e^{-t^2 4\ell n2/T_L^2}$; a Lorenztian: $1/(t^2+T_L^2/4)$; and a full exponential: $e^{-|t|\,2\ell n2/T_L}$ where $\mu(t)$ is unit step function, T_L is the full width at half maximum of the laser pulse, and T_1 is the phonon lifetime. Figures V-21 through V-23 plot the extracted lifetime obtained from the slope of the convolution tail versus the phonon lifetime defined by the equation e^{-t/T_1} for different laser shapes. The convolution calculation plotted in Figs. V-21, V-22, and V-23 are for a guassian, full exponential and Lorentzian laser pulse shape respectively. A summary of the results obtained from these three figures are: The convolution of an exponential phonon decay time (T_1) with a Gaussian-shaped laser pulse rapidly assumes the exponential decay T_1 with an error of $\leq 1\%$ for $T_1 > T_L$ for $t > T_L$. With an exponentially shaped laser pulse the convolution rapidly assumes the exponential decay T_1 with an error $\leq 10\%$ for $T_1 \geq T_L$ for $t > T_L$. For a Lorenztian shaped laser pulse the error in T_1 is $\leq 50\%$ for $T_1 \geq T_L$ and for $t \geq T_L$. For all the lifetimes measured in the thesis the error is $< 18\%$ due to convolution if Lorenztian laser shape is taken into account and $<1\%$ if the Gaussian and exponentially shape is assumed. The laser pulse has been shown to be between exponential and Gaussian in shape by Autson.[38]

Calculated Raman probe scattered energy profiles versus τ_D are plotted in Fig. V-24. These curves arise from the convolution of an exponential decaying phonon population (T_1 = 22 psec) with (a) Gaussian, (b) full exponential, (c) Lorenztian laser pulse shape with FWHM T_L = 3 psec. Notice the rise portion of these curves depends on the shape of the laser pulse while the tail decays at the same rate T_1 (when $T_1 > T_L$ for $t \geq T_L$). Therefore, as long as $T_1 \geq T_L$ there is a small error in extracting the phonon lifetime. The % errors are depicted in Figs. V-21–V-24 for a given T_1/T_p ratio.

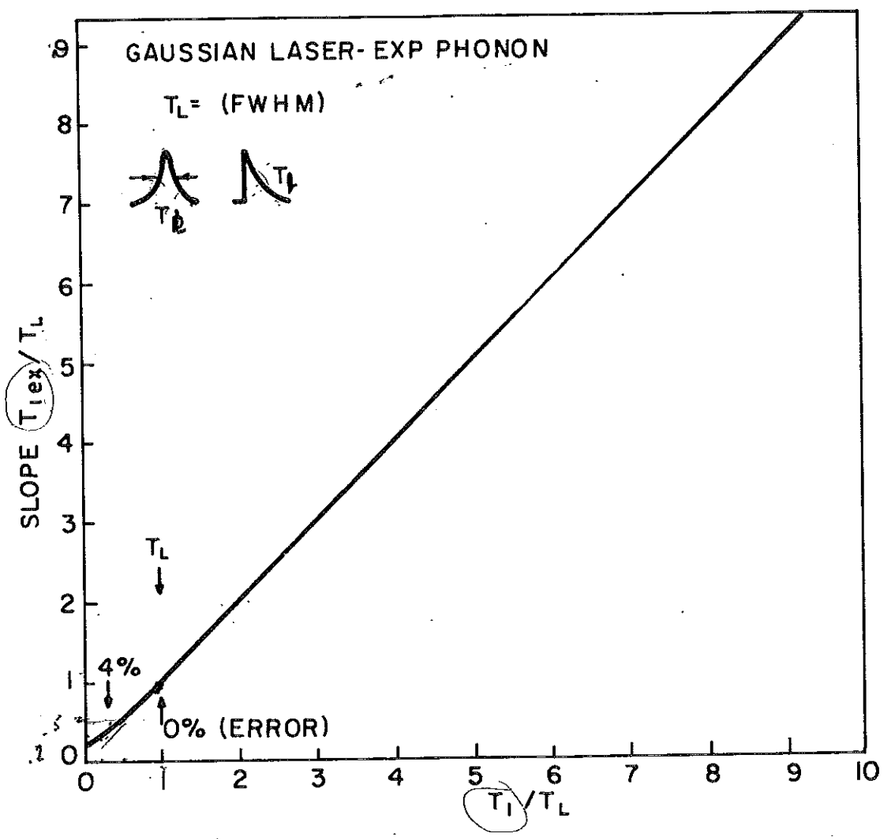

Fig. V-21. A plot of the phonon lifetime T_1 versus the phonon lifetime T_{1ex} extracted from the tail of the convolution of an exponential decaying phonon population at a rate T_1 with a Gaussian shape laser pulse of duration T_L. The T_{1ex} is obtained from the slope of tail at $\tau_D > T_L$. The percent error in T_1 is shown at varius T_1/T_L ratios.

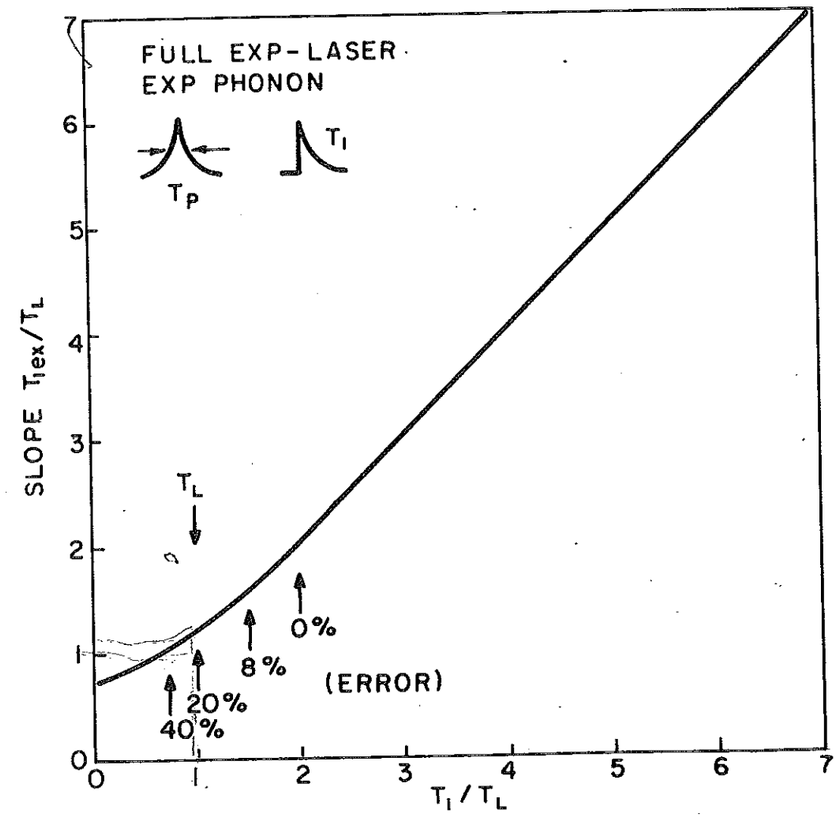

Fig. V-22. A plot of the phonon lifetime T_1 versus the phonon lifetime T_{1ex} extracted from the tail of the convolution of an exponential decaying phonon population at a rate T_1 with full exponential shape laser pulse of duration T_L.

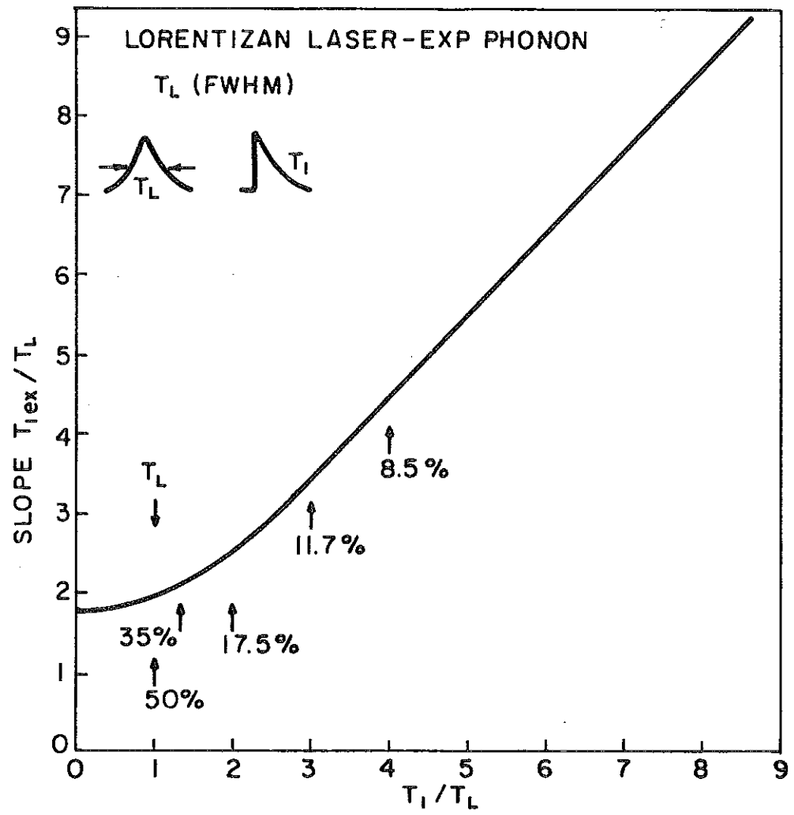

Fig. V-23. A plot of the phonon lifetime T_1 versus the lifetime T_{1ex} extracted from the tail of the convolution of an exponential decaying phonon population at a rate T_1 with a Lorenztian shape laser pulse of duration T_L.

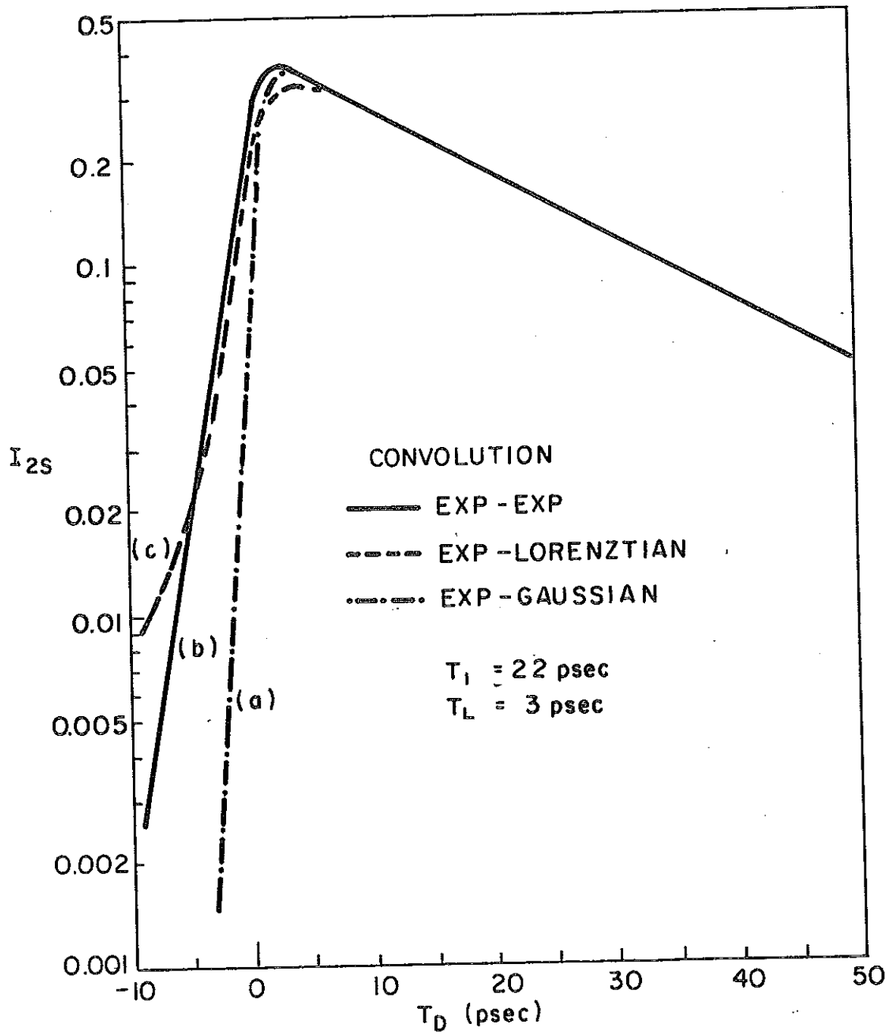

Fig. V-24. Plot of an exponentially decaying phonon population (T_1 = 22 psec) convoluted with (a) Gaussian, (b) full exponential, and (c) Lorenztian laser shape pulse of FWHM of 3 psec.

The rise portion of the experimental observed probe Stokes scattering energy in Fig. V-14 can be fitted with an exponential shape laser pulse of FWHM of T_L = 5 psec. This is illustrated in Fig. V-25 where a plot of the experimental Raman probe energy at 100°K versus τ_D is fitted within the experimental error to a plot of a convoluted profile for an exponential decaying phonon population (T_1 = 19 psec) with an exponential shape laser pulse (T_L = 5 psec.)

D. Future Direction

The probe technique developed in this thesis can be used to probe the lifetime of molecular vibrations in liquids. The spontaneous Raman linewidth measurements in, for example, liquid nitrogen indicates a linewidth[45] of 0.067 cm^{-1}. From the inverse of this linewidth, one deduces a lifetime of 75 psec. The Raman line in liquid nitrogen is not composed of a single damped vibration but is a damped vibrational-rotational entity. Therefore, the direct measurement of this lifetime should reveal interesting results.

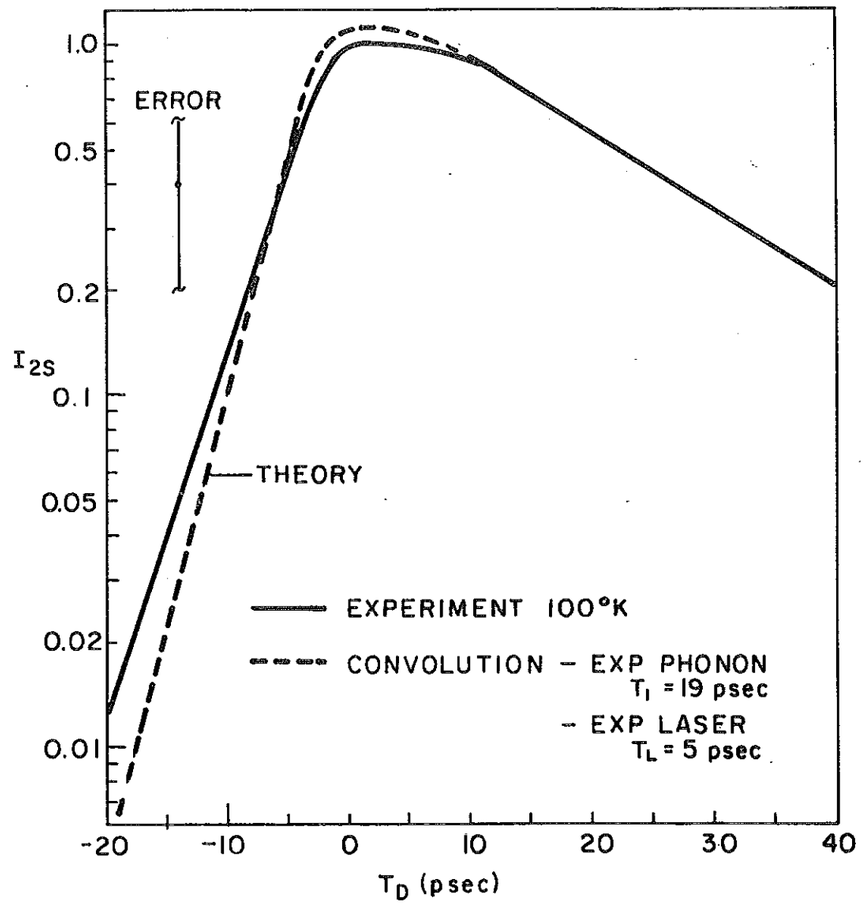

Fig. V-25. Plot (a) is the calculated probe Stokes energy versus delay time τ_D (convolution of exponentially decaying phonon population with lifetimes T_1 = 19 psec with an exponentially shaped laser pulse of duration T_L = 5 psec); and a plot (b) is the experimentally measured probe Stokes energy at 100°K from calcite (the measured lifetime from the tail is T_1 = 19.1 psec). The convolution curve is shifted in time by 5 psec to match the tails.

V. REFERENCES

1. R. R. Alfano, Bull. Amer. Phys. Soc. 15, 1324 (1970); R. R. Alfano and S. L. Shapiro, Phys. Rev. Letts. 26, 1247 (1971).

2. P. G. Klemens, Phys. Rev. 148845 (1964); in Solid State Physics edited by F. Seitz and D. Turbull (Academic Press, NY, 1958, vol 7, p 1.

3. J. P. Mathieu, Spectres de Vibration et Symetie (Herman and Cie) Paris 1945.

4. M. J. Colles, Opt. Comm. 1, 170 (1969).

5. K. Park, Phys. Letts. 22, 39 (1966); 25A, 490 (1967).

6. J. A. Giordmaine and W. Kaiser, Phys. Rev. 144, 676 (1966).

7. F. DeMartini and J. Ducuing, Phys. Rev. Letts. 17, 117 (1966).

8. W. Heinicke, G. Winterling, and K. Dransfeld, Phys. Rev. Letts. 22, 170 (1969).

9. M. Born and E. Wolf, Principles of Optics (Pergamon Press, London, 1959), Chap. 14.

10. Rossi, OPTICS, (Academic Press, N.Y. 1960).

11. International Critical Tables, (McGraw Hill Book Co. Inc., New York, 1930) Vol. 7, p. 24.

12. These angles where computer calculated using the procedure outlined by L. Hadley of GTE Computer Group.

13. We conservatively choose the total burst of radiation as the pulse width instead of the sharp correlation peak of the two-photon fluorescence pattern which is 2 psec full width at half-maximum for the fundamental; see, for example, S. L. Shapiro and M. A. Duguay, Phys. Lett. 28A, 698 (1969).

14. M. A. Duguay and J. W. Hansen, Appl. Phys. Lett. 15, 192 (1969).

15. The intensity of the probe beam versus the delay time between the 1.06- and 0.53-μm beams is a symmetric curve of FWHM ~8 psec, which is approximately the convolution of the 6-psec pulse width of the 1.06-μm beam, 4-psec pulse width of the 0.53-μm beam, and 2-psec Kerr relaxation time of CS_2. This overestimates the prompt curve which is the convolution of the Raman light, of pulse width < 2.7 psec, and the effective pulse width of the probe laser off the created phonons, <4 psec.

16. R. L. Carman, F. Shimizu, C. S. Wang, and N. Bloembergen, Phys. Rev. A 2, 60 (1970).

17. M. J. Colles, Opt. Commun. 1, 169 (1969); R. L. Carman, M. E. Mack, F. Shimizu, and N. Bloembergen, Phys. Rev. Lett. 23, 1327 (1969); R. R. Alfano and S. L. Shapiro, Phys. Rev. A 2, 2376 (1970).

18. W. H. Glenn and M. J. Brienza, Appl. Phys. Lett. 10, 221 (1967).

19. The interaction length $l_c = T_L \bar{V}_g / 2\Delta V_g$ for two pulses has been defined as the distance for which two pulses stay spatially coincident by less than a half-pulse width; T_L is the pulse width, $\bar{V}_g$ is the average group velocity, and ΔV_g is the difference in group velocities. The Raman interaction length of 3.0 cm for calcite stated by Colles (Ref. 16) is for ~ 1 psec pulses. A pulse width of 4 psec is used to compute l_c in this paper.

20. Convolution calculations are given in detail in Section 4. A summary of the results are as follows: The convolution of an exponential phonon decay (T_1) with a Gaussian-shaped laser pulse (full width T_L at half-maximum) rapidly assumes the exponential decay T_1 with an error of $\leq 1\%$ for $T_1 \geq T_L$ for $t > T_L$. With an exponential-shaped laser pulse the convolution rapidly assumes the exponential decay T_1 with an error $\leq 10\%$ for $T_1 \geq T_L$ for $t > T_L$. For both the lifetimes measured in this paper the error is $< 1\%$ due to deconvolution. The precision of the results is not altered for the conservative pulse widths we have chosen (See Ref. 13).

21. The rise of the intensity curve in Fig. V-14could be fitted by the convolution of exponentially shape probe laser (T_L=5 psec), decaying phonons (T_1=19 psec).

22. K. Park, Phys. Lett. 22, 39 (1966). The linewidth and corresponding calculated lifetime assuming a Lorentzian shape are $\Delta\bar{\nu}_{300°K} \cong 1.1 \pm 0.12$ cm^{-1}, $\tau_{300°K} \cong 4.8 \pm 0.5$ psec; $\Delta\bar{\nu}_{100°K} \cong 0.69 \pm 0.12$ cm^{-1}, $\tau_{100°K} \cong 7.7 \pm 1.4$ psec; and $\Delta\bar{\nu}_{10°K} \cong 0.4 \pm 0.12$ cm^{-1}. $\tau_{10K} \cong 13.4 \pm 4$ psec. However, the linewidths are in slight disagreement with later reported values by K. Park, Phys. Lett. 25A, 490 (1967), of $\Delta\bar{\nu}_{300°K} \cong 1.5$ cm^{-1}, $\tau_{300°K} \cong 3.6$ psec, $\Delta\bar{\nu}_{100°K} \cong 0.69$ cm^{-1}, $\tau_{100°K} \cong 7.7$ psec; and $\Delta\bar{\nu}_{10°K} \cong 0.5$ cm^{-1}, $\tau = 10.7$ psec (no error bar given).

23. The discrepancy between the lifetimes may be related to the depopulation(T_1) and dephasing (T_2) lifetimes since these may be different for thermal and coherent phonons. Alternatively the two measuring techniques may weight differently the relative contributions of T_1 and T_2. The relevance of T_1 and T_2 to the experiment was pointed out by Dr. A. Lempicki.

24. S. Simons, Proc. Phys. Soc., London 82, 401 (1963).

25. R. Orbach, Phys. Rev. Lett. 16, 15 (1966).

26. See, for example, E. R. Cowley and R. A. Cowley, Proc. Roy. Soc., Ser. A287, 259 (1965); W. J. L. Buyers and R. A. Cowley, Phys. Rev. 180, 755 (1969).

27. E. R. Cowley, private communication.

28. M. Born and K. Huang, Dynamical Theory of Crystal Lattice, Oxford Press, London 1962).

29. C. Herring, Phys. Rev. 95, 954 (1954) and reference therein.

30. R. A. Cowley, J. Phys. (Paris) 26, 659 (1965); Reports on Progress in Physics, Vol. XXXI, Part I, 123 (1968).

31. P. G. Klemens, Phys. Rev. 148, 845 (1964); in Solid State Physics, edited by F. Seitz and D. Turbull (Academic Press, N.Y., 1958), Vol. 7, p. 1.

32. A. Pines and P. E. Tannewald, Phys. Rev. 178, 1424 (1968).

33. M. Sparks, Ferromagnetic Relaxation Theory, (McGraw Hill, N.Y., 1964).

34. A. Messiah, Quantum Mechanics (John Wiley and Sons, NY, 1963), Vol. II.

35. Kittel, in Phonons, edited by R. Stevenson (Plenum Press, NY, 1966), p. 1.

36. G. Winterling, W. Heinicki, and K. Dransfield, in Light Scattering in Solids, edited by G. White, (Springer-Verlag, NY 1969) p. 589.

37. N. Bloembergen, Nonlinear Optics (Benjamin, New York, 1965).

38. D. H. Autson, Appl. Phys. Letters 18, 249 (1971). The laser pulse emitted from mode-locked Nd:glass laser has been shown to be between an exponential and Gaussian in shape.

39. R. L. Carman, preprint (1970); R. L. Carman, F. Shimizu, C. S. Wang, N. Bloembergen, Phys. Rev. A2, 60 (1970).

40. J. A. Giordmaine and W. Kaiser, Phys. Rev. 144, 676 (1966).

41. R. R. Alfano and S. L. Shapiro, Phonons, edited by M. Nusimovici, Proceeding of International Conference of Phonons, Rennes, France, July 1971, p. 191 (Flammarion Sciences, Paris, France). After completing this work and submission to the conference in February 1971, D. von der Linde, A. Laubereau, and W. Kaiser, Phys. Rev. Letters 26, 954 (1971) published a similar analysis in only liquids.

42. Y. R. Shen and W. Bloembergen, Phys. Rev. 137, A1787 (1965).

43. Panofsky and Philips, Classical Electricity and Magnetism, (Addison and Wilsy, New York 1962) p. 449.

44. In order to phase match the created phonons in calcite to the probe beams, the probe beam must propagate as E-wave. Therefore, the probe scattering analysis for the isotropic material must be modified. The wave equation is given by

$$\nabla \times \nabla \times \bar{E}_s = -\frac{1}{C^2} \frac{\partial^2 \bar{D}_s}{\partial t^2} - \frac{4\pi}{C^2} \frac{\partial^2 \bar{P}_{NL}}{\partial t^2} . \qquad \text{(i)}$$

The Stokes field has the form

$$\bar{E}_s = \hat{e}_s \mathcal{E}_s e^{i(\bar{k}_s \cdot \bar{r} - \omega_s t)} . \qquad \text{(ii)}$$

It can be shown[40] that

$$\nabla \times \nabla \times E = (i\bar{k} \times \nabla \mathcal{E} \times \hat{e} - \bar{k} \times \bar{k} \times \hat{e}\,\mathcal{E} + i \nabla \mathcal{E} \times \bar{k} \times \hat{e})\, e^{i\bar{k} \cdot \bar{r}}$$

$$\bar{D} = -n^2 \hat{k} \times \hat{k} \times \bar{E} \qquad \text{(iii)}$$

and

$$\frac{1}{c^2}\frac{\partial^2 \bar{D}}{\partial t^2} = \left(\bar{k}\times\bar{k}\times\hat{e}\,\mathcal{E} + \frac{2i}{\omega}\,\bar{k}\times\bar{k}\times\hat{e}\,\dot{\mathcal{E}}\right) e^{i\bar{k}\cdot\bar{r}}$$

where second derivatives are neglected.

Substituting Eqs. iii into Eq. i and dotting with e, one obtains:

$$\left(\frac{\partial \mathcal{E}_s}{\partial z} + \frac{1}{\bar{V}_s}\frac{\partial \mathcal{E}_s}{\partial t}\right)\cos\gamma\cos\alpha_s e^{i\bar{k}_s\cdot\bar{r}} = \frac{4\pi}{2k_s ic^2}\,\hat{e}_s\cdot\frac{\partial^2}{\partial t^2}\,\bar{P}_s^{NL} \qquad \text{(iv)}$$

where γ is the angle between the ray direction (Poynting) S and the normal to the surface (z) and α_s is the angle between $\vec{k}$ and S. The nonlinear polarization $\bar{P}_s^{NL} = \underline{\underline{a}}'\cdot\hat{e}_L Q^* E_L$ and $\hat{e}_s\cdot\vec{P}_x^{NL} = \hat{e}_s\cdot\underline{\underline{a}}'\cdot\hat{e}_L Q^* E_L \equiv \underline{\underline{a}}' : \hat{e}_L\hat{e}_s Q^* E_L$.

The Stokes wave is governed by

$$\left(\frac{\partial \mathcal{E}_s}{\partial z} + \frac{1}{\bar{V}_s}\frac{\partial \mathcal{E}_s}{\partial t}\right)\cos\gamma\cos\alpha_S e^{i\bar{k}_s\cdot\bar{r}} = \frac{4\pi\omega_s^2\,\underline{\underline{a}}'\cdot\hat{e}_L\hat{e}_s\,q^*\mathcal{E}_L e^{i(\bar{k}_L-\bar{k}_s)\cdot\bar{r}}}{2k_s ic^2} \qquad \text{(v)}$$

Using the change of variable given by Eq. (57), the Stokes equation (v) becomes

$$\frac{\partial \mathcal{E}_s}{\partial z'} = -\frac{4\pi\omega_s^2\,\underline{\underline{a}}'\cdot\hat{e}_L\hat{e}_s\,q^*\mathcal{E}_L e^{i\Delta\bar{k}\cdot\bar{r}}}{2k_s ic^2\quad\cos\gamma\cos\alpha_S} \qquad \text{(vi)}$$

where $\Delta\bar{k} = \bar{k}_L - \bar{k}_p - \bar{k}_s$.

The energy propagates along $\hat{S}$ and $\hat{S}\cdot\hat{z} = \cos\gamma$. Therefore $\frac{\partial \mathcal{E}_s}{\partial z'}\cos\gamma = \frac{\partial \mathcal{E}_s}{\partial s}$. Equation (vi) becomes

$$\frac{\partial \mathcal{E}_s}{\partial s} = \frac{i\,2\pi\omega^2\,\underline{\underline{a}}'\cdot\hat{e}_L\hat{e}_s}{k_s c^2\cos\alpha_S}\,q^*\mathcal{E}_L e^{i\Delta k_s}\,. \qquad \text{(vii)}$$

The magnitude of Poynting vector for Stokes wave is given by

$$|S_s| = \frac{cn_s}{4\pi}|\mathcal{E}_s|^2\cos\alpha_S. \qquad \text{(viii)}$$

Therefore, the probe Stokes energy scattered is given by

$$I_{2s} = \frac{cn_{2s}}{4\pi} \int |\mathcal{E}_{2s}|^2 \, dt \qquad \text{(ix)}$$

$$= B\eta^2 \left(\frac{\sin \frac{\Delta k \ell}{2}}{\frac{\Delta k}{2} \ell} \right)^2 \ell^2 \int | q(t') |^2 \, | \mathcal{E}_{2L}(t' + \tau_D) |^2 \, dt'$$

where

$$B = \frac{c^2 k_{2s} \cos \alpha_S}{4\pi \omega_{2s}} \text{ and } \eta = \frac{2\pi \omega_{2s}^2 \, \underline{a}' \cdot \hat{e}_{2L} \hat{e}_{2s}}{k_{2s} c^2 \cos \alpha_S} .$$

45. W. R. Clements and B. P. Stoicheff, Appl Phys. Letters 12, 246 (1968).